Multivariable Control of the Space Shuttle Remote Manipulator System Using Linearization by State Feedback

by

Chang-Ching Lo Gettman

B.S., Engineering Mechanics
Johns Hopkins University, Baltimore, Maryland
(1990)

SUBMITTED TO THE DEPARTMENT OF AERONAUTICS AND ASTRONAUTICS IN PARTIAL FULFILLMENT OF THE REQUIREMENTS FOR THE DEGREE OF

MASTER OF SCIENCE

at the

MASSACHUSETTS INSTITUTE OF TECHNOLOGY

May, 1993

Signature of Author _____
Department of Aeronautics & Astronautics
May, 1993

Approved by _____
Neil J. Adams
Technical Staff, Charles Stark Draper Laboratory
Technical Supervisor

Certified by _____
Professor Lena Valavani
Thesis Supervisor, Associate Professor of Aeronautics and Astronautics

Accepted by _____
Professor Harold Y. Wachman
Chairman, Departmental Graduate Committee

Multivariable Control of the Space Shuttle Remote Manipulator System Using Linearization by State Feedback

by

Chang-Ching Lo Gettman

Submitted to the Department of Aeronautics and Astronautics on May 7, 1993 in partial fulfillment of the requirements for the degree of Master of Science

Abstract

This thesis demonstrates an approach to nonlinear control system design that uses linearization by state feedback to allow faster maneuvering of payloads by the Shuttle Remote Manipulator System (SRMS). A nonlinear feedback law is defined to cancel the nonlinear plant dynamics so that a linear controller can be designed for the SRMS. Model reduction techniques were employed to reduce computation time so that an implementable controller can be delivered.

First a nonlinear design model was generated via *SIMULINK*. This design model included nonlinear arm dynamics derived from the Lagrangian approach, linearized servo model, and linearized gearbox model. The current SRMS position hold controller was implemented with and without feedback linearization on this system. The contribution of the joint accelerations from the nonlinear feedback was compared with that of the control for different joint rates, mass, and dimensions.

Next, a trajectory was defined using a rigid body kinematics SRMS tool, KRMS. The maneuver was simulated with and without feedback linearization. Then, a nonlinear model of the gearbox was included in the *SIMULINK* design model. Finally, higher bandwidth controllers were developed. Results of the new controllers were compared with the existing SRMS automatic control modes for the Space Station Freedom Mission Build 4 Payload extended on the SRMS.

Technical Supervisor: Neil J. Adams
Technical Staff, Manned Space Systems Division
The Charles Stark Draper Laboratory, Inc.

Thesis Supervisor: Dr. Lena Valavani
Associate Professor of Aeronautics and Astronautics

Acknowledgments

I would like to thank the Charles Stark Draper Laboratory for giving me the opportunity to pursue my Masters Degree at MIT, and John Sweeney and Joan Chiffer for making the Draper Fellow program possible.

I thank my thesis supervisors Neil Adams and Lena Valavani for their time, guidance and support during my studies at MIT and during this research endeavor. Neil and Lena always found time in their busy schedules for my questions. They have made my experience at MIT truly rewarding. I thank Neil for spending countless hours to help me solve problems that we encountered. I want to thank Lena for being the most personable and approachable professor that I have met at MIT and for always being there for pep talks and moral support. I would also like to thank Draper Staff: Brent Appleby, Naz Bedrossian, Paul DeBitetto, Kevin Gift and Joe Turnbull for all the technical support they gave me.

I would like to thank my officemate, Roger "Knapperama" for putting up with me. I would like to thank all the other students: Eugene-the money-man, Dr. Ruth, Dr. Dean-who sold his body to science, the three Steves, the two Toms, Craig-who needs some non-Duke clothes, Bill-the former student, Alex, Bryan-the math GOD, Torsten, Keith, Mark, and all the other Draper Fellows for such a memorable experience at Draper. I also thank all the Draper hockey players and spectators for all the fun games we had. Go get'um next year DRAPER!!! Many thanks, to Carol, Deb, Susan, and Eva at Draper and Liz and Jennie at MIT for all their help.

Most of all, I thank my family: husband Matt, my parents, sisters, in-laws, and Pug & Gypsy for their love, support, and patience!!!

This report was prepared at The Charles Stark Draper Laboratory, Inc., under contract NAS9-18147.

Chang-Ching Lo Gettman

Table of Contents

List of Figures

List of Tables

Chapter 1

Introduction

The Space Shuttle Remote Manipulator System (SRMS) will be a key component in the assembly process of the Space Station Freedom (SSF). The process on the early flights will require capturing an orbiting intermediate SSF build via the SRMS and then retracting the arm to berth the SSF in the payload bay. Berthing is accomplished by latching the Unpressurised Berthing Adaptor (UBA) to the trunnions and keel via payload retention latches. After latching, the SRMS is used to attach cargo bay SSF truss segment and component elements to the UBA attached SSF build. Each Shuttle flight carries approximately 35,000 lb. of SSF payload to be assembled on-orbit via the SRMS. SRMS operations, particularly the time required to complete specific SRMS maneuvers, has a significant impact on operational mission timelines.

Experience with SRMS operations [1] indicates several areas where improvements can be made including: speed of manipulation, positioning accuracy, and vibration control. The speed of manipulation depends both on the system bandwidths and the maneuver velocities. A significant amount of time is spent damping vibrations caused by a SRMS maneuver, while maneuver velocities are kept small to achieve stopping distance criteria

and limit vibration. Several active or passive vibration damping systems have been recently developed. For example, Prakash et al. [2] discuss the application of multivariable linear optimal control to the problem of position hold and active vibration damping. Scott and Demeo [3] developed an active damping augmentation system using an identified system model from simulation. Sasiadek [1] discusses passive damping by manipulator redesign and the application of new materials. He also discusses active vibration control via input pre-shaping and the application of force feedback. The current SRMS [4] automatic mode commands the end effector to move along a linear trajectory at a constant velocity using bandwidth limitations and adjustments to the coast velocity to provide reasonable transient responses at either end of a maneuver.

This thesis develops and demonstrates an approach to nonlinear control system design using linearization by state feedback. The design provides improved transient response behavior allowing faster maneuvering of payloads by the SRMS. Modeling uncertainty is accounted for using a second feedback loop designed around the feedback linearized dynamics. A classical feedback loop is developed to provide the easy implementation required for the relatively small onboard computers. Feedback linearization also allows the use of higher bandwidth model based compensation in the outer loop since it helps maintain stability in the presence of the nonlinearities typically neglected in model based designs.

This thesis is organized as follows. Chapter 2 provides a brief description of the Shuttle SRMS. Chapter 3 develops the approach taken and the theory applied. Chapter 4 discusses the nonlinear manipulator dynamics, the nonlinear servo and gearbox models used for simulation, and the reduced models used for design of the compensation. Chapter 5 develops the control laws to be used for maneuvering the SRMS with a deployed payload. Chapter 6 demonstrates performance of the system with and without

feedback linearization during a maneuver. The implementation of the steering algorithm is also discussed in Chapter 6. Finally, Chapter 7 presents the conclusions and discusses topics for future work.

Chapter 2

Remote Manipulator System

A team of Canadian companies led by SPAR Aerospace Limited of Toronto designed, developed, tested and manufactured the anthropomorphic Space Shuttle Remote Manipulator System (SRMS). The SRMS was first tested on-orbit in November 1981 on the Space Shuttle Columbia. This development of the SRMS was performed under a contract from the National Research Council of Canada (NRCC) under the guidance of NASA.

This chapter presents background information about the SRMS. Section 2.1 gives physical descriptions of SRMS components, while section 2.2 discusses SRMS software. The coordinate systems for the SRMS are defined in section 2.3. Finally, Payload Deployment and Retrieval System (PDRS) operating modes are discussed in section 2.4

2.1 Physical Description

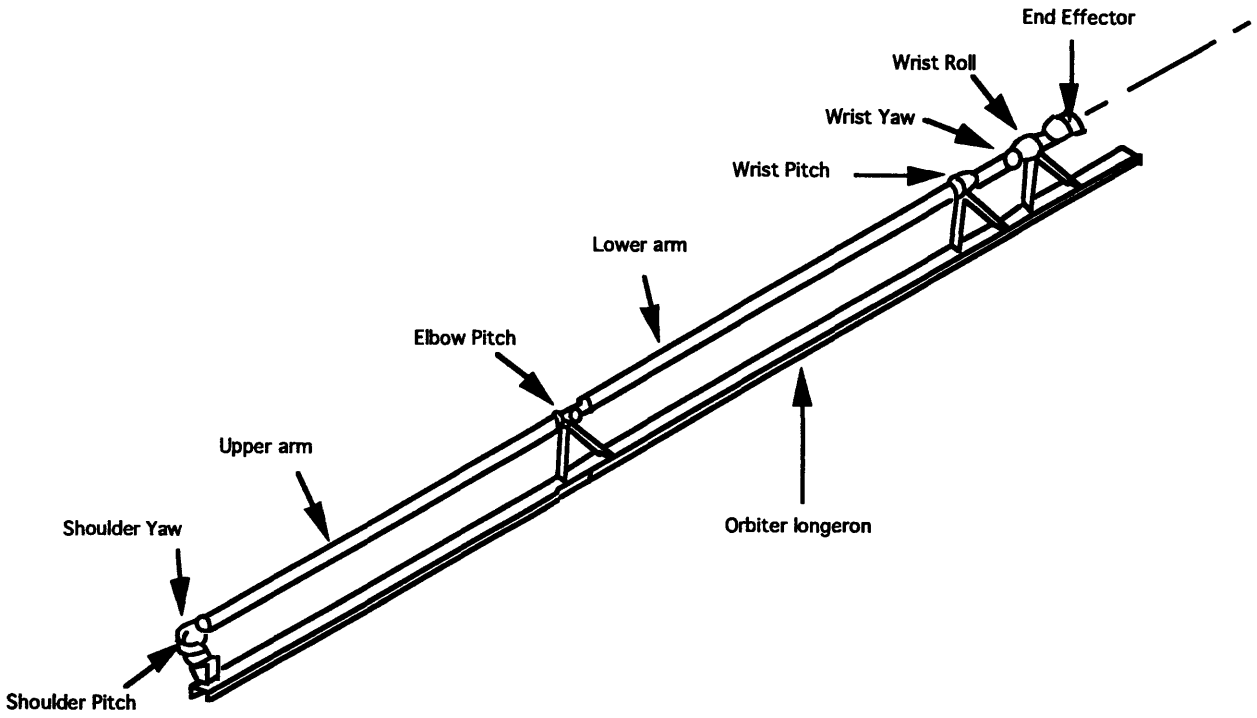

Figure 2.1. SRMS Physical Description

The Space Shuttle Remote Manipulator System is illustrated in Figure 2.1. It is a crucial part of the Space Shuttle Payload Deployment and Retrieval System (PDRS) and is the Orbiter baseline on-orbit cargo handling system. The SRMS is used to maneuver payloads to the cargo bay for berthing and from the cargo bay for deployment. The SRMS can handle payloads of up to 65,000 lb. mass with dimensions of up to 60 feet in length and 14 feet in diameter from up to a 49 feet distance in space. Other SRMS applications include: inspection, servicing and repair of spacecraft; transfer of men, work stations and equipment; crew extravehicular activities (EVA) as well as the on-orbit assembly of the Space Station Freedom (SSF).

2.1.1 Mechanical Arm Assembly

The mechanical arm assembly is 50 feet 3 inches in length, 15 inches in diameter, and has a mass of 905 pounds. It is located on the port side of the vehicle and stowed outside the payload dynamic envelope. It consists of six individual joints: shoulder yaw, shoulder pitch, elbow pitch, wrist pitch, wrist yaw, and wrist roll, as shown in Figure 2.2. These joints provide six degrees-of-freedom at the end effector. The shoulder yaw, shoulder pitch, and elbow pitch joints provide the translational capability, while the wrist joints provide the attitude pointing. The motion is coordinated by an onboard computer from operator inputs or automatic trajectory points.

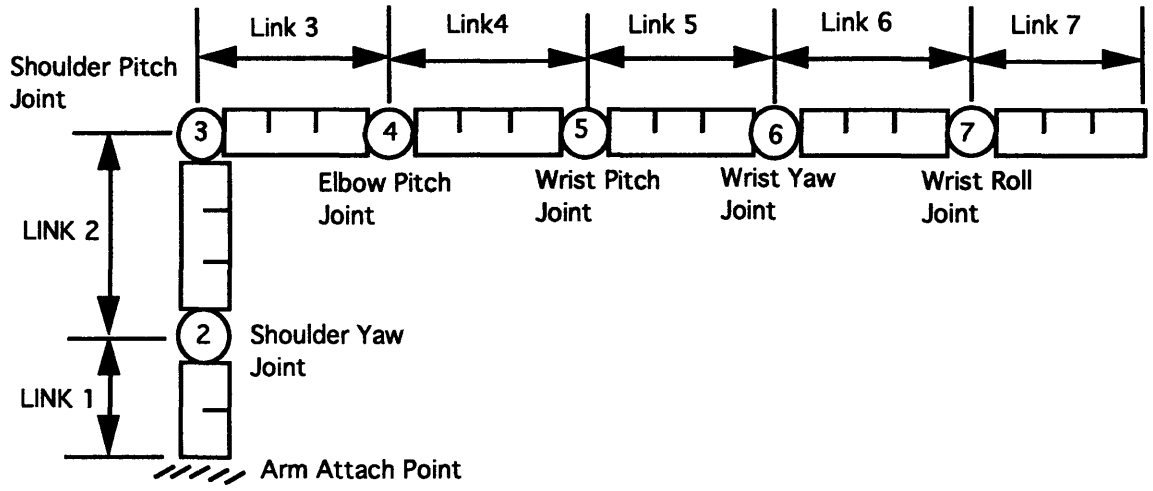

Figure 2.2. Model of SRMS

The SRMS hardware is comprised of a mechanical arm assembly, manipulator controller interface unit (MCIU), end effector, thermal protection system, and shoulder brace. The following sections will describe each of these elements.

2.1.2 MCIU

The MCIU contains the circuitry for interfacing with the general purpose computer (GPC), display and control subsystem (D&C), arm based electronics, brace control functions, end effector automatic functions, and the built-in test equipment (BITE). The hand controllers and D&C panel send signals through the MCIU to the Orbiter GPC where the commands are converted into joint motor rate commands. The MCIU then passes these joint rate commands and current limits to the corresponding joints.

2.1.3 End Effector

The end effector is a hollow cylinder 13.6 inches in diameter and 21.5 inches long. It connects the arm to the payload. The purpose of the end effector is twofold: to grapple a payload and keep it rigidly attached as long as required or to release a grappled payload. The end effector is attached to the wrist roll motor and physically interfaces with the payload grappling fixture.

2.1.4 Thermal Protection System

The on-orbit thermal environment requires that the manipulator have thermal protection. Thermal protection is achieved through both passive and active control. The passive thermal control system consists of insulation blankets and coatings, while the active thermal control system uses heaters.

2.1.5 Shoulder Brace

The shoulder brace is used to carry loads during launch. It is installed between the upper arm boom and the shoulder pedestal and must be released to allow arm uncradling during flight. The shoulder brace cannot be relatched during orbit and is not required for landing.

2.2 SRMS Software

The SRMS software is organized into 15 principal functions to perform mathematical and logical operations to monitor and control the active mechanical arm motion. It first selects and initiates the control modes. It then computes the command inputs and the operational status. SRMS caution and warning signals are generated and fault detection is performed.

2.3 Coordinate Systems

RMS and payload POR positions (X,Y,Z) are always defined in the orbiter body axis system (OBAS). The origin of the OBAS is 236 inches in front and 400 inches below the nose of the orbiter. The +X axis points away from the Orbiter nose, while the +Y axis points towards the starboard wing, and the +Z axis points "downward." A positive roll rotates the port wing "up", while a positive pitch rotates the nose "up", and a positive yaw rotates the nose starboard.

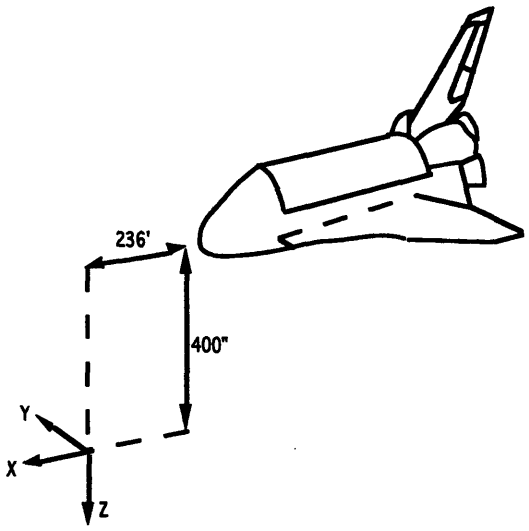

Figure 2.3. Orbiter Body Axis System (OBAS) for POR Translations

RMS and payload Point of Resolution (POR) attitudes (pitch, yaw, roll Euler sequence) are defined in the orbiter rotation axis system (ORAS). The origin of the ORAS coincides with the origin of the OBAS. However, the +X axis points towards the tail of

the Orbiter, while the **+Y** points towards the port wing, and the **+Z** axis points "downward." In ORAS, a positive roll rotates the port wing "down", a positive pitch rotates the tail "up", and a positive yaw rotates the nose starboard.

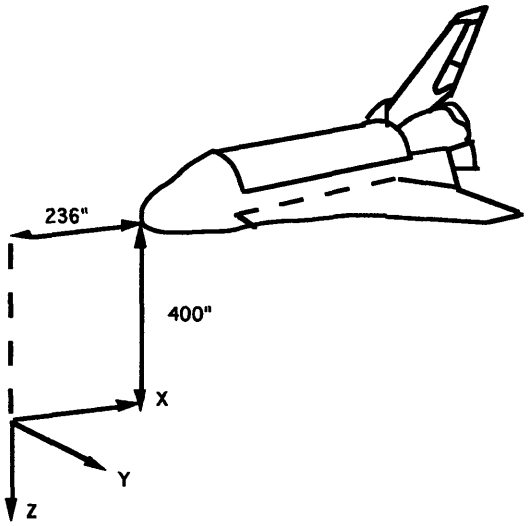

Figure 2.4. Orbiter Rotation Axis System (ORAS) for POR Rotations

The end effector operating system (EEOS) is fixed with respect to the end effector. The EEOS defines the axis along which the end effector will move. The payload operating system (PLOP) is a right-handed orthogonal coordinate system that defines the axes along which the payload translates and rotates when the SRMS is in the manual mode. The origin of the PLOP is chosen to be some fixed point on the payload. It is commonly given as a transpose of the payload axis system (PAS) with its axes parallel to those of the ORAS when the payload is berthed. The PAS is defined by the payload designer and must also be a right-handed, orthogonal coordinate system.

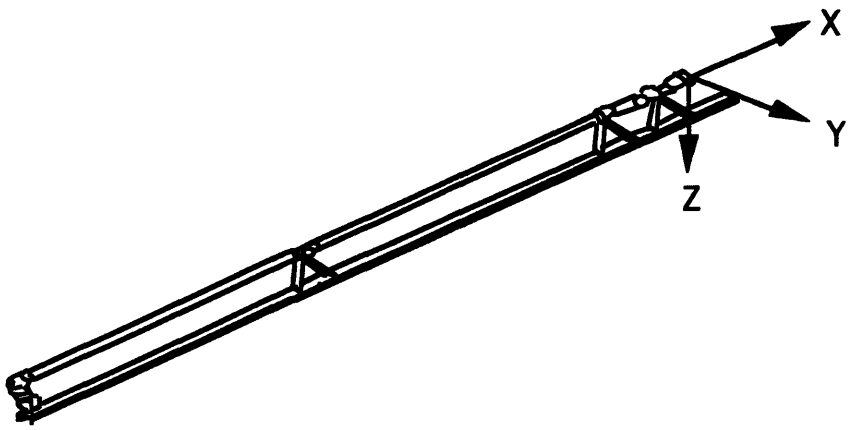

Figure 2.5. End Effector Operating System (EEOS)

2.4 PDRS Operating Modes

Operation of the SRMS is based on the "man-in-the-loop" concept, when the operator is an integral part of the control and monitoring system [4]. An operator controls the SRMS from the Display and Control (D&C) panel in the aft flight deck. Command inputs are based on visual, closed circuit television feedback, and information available on the D&C panel as shown in Figure 2.6. Visual contact is imperative to avoid collisions between the SRMS, orbiter and payload.

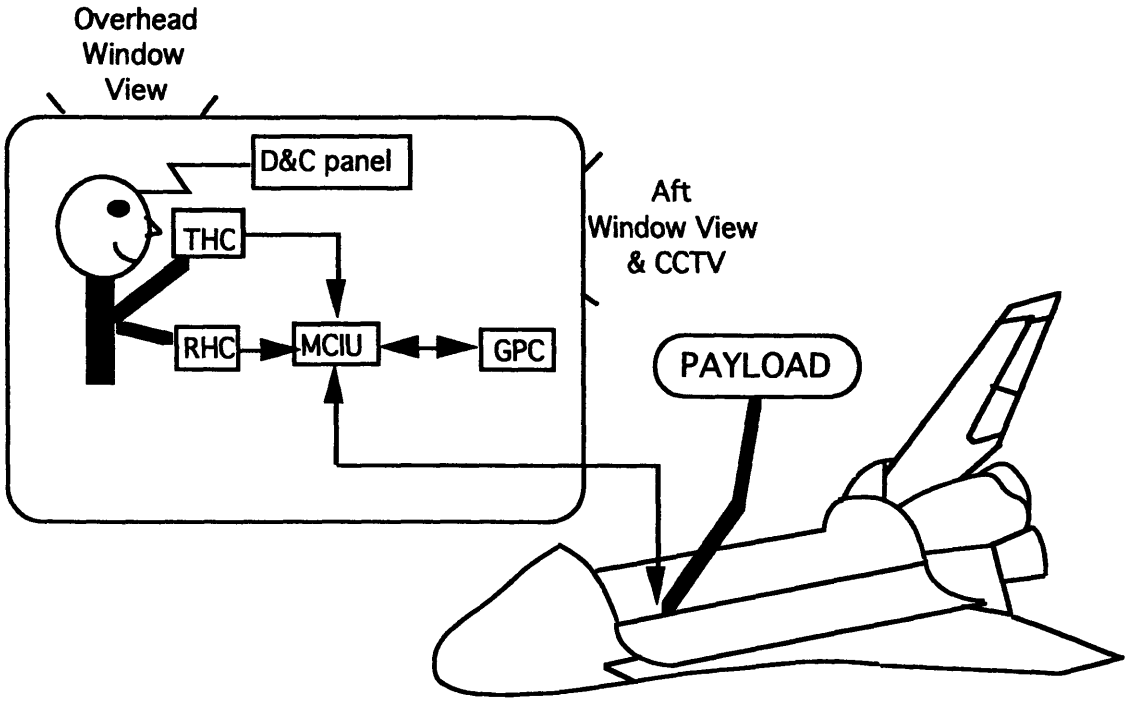

Figure 2.6. "Man-in-the-loop" Concept

There are four primary control modes: manual augmented, automatic, manual single joint, and direct drive, as well as one back-up mode. The operator can move the SRMS end effector in six degrees-of-freedom, three rotation and three translation, using either the manual or automatic control modes. These control modes will be described in more detail.

2.4.1 Manual Augmented Modes

The Manual Augmented Mode is the normal mode of operation of the SRMS. One or more joints are driven simultaneously to translate and rotate the end effector in the Manual Augmented Mode. The operator uses two three degree-of-freedom hand controllers to issue commands. One of the hand controllers is for rotation in pitch, yaw and roll about the point of resolution (POR), a convenient and easily visible component on the manipulated payload. The other is for translation, resolved for up/down, left/right, and fore/aft. During this mode of operation, cross-coupling (which varies with payload

mass and POR velocity) and drifting in uncommanded directions can be expected. However, once the arm is stationary, its position can be maintained to within +/-2 inches and +/- 1 degrees. The control algorithms for manual augmented modes process the astronaut's input commands into rate demands for each of the six joints.

All together, there are four types of manual augmented modes: orbiter unloaded mode, orbiter loaded mode, end effector mode, and payload mode. Each of these modes provides control for a different combination of POR, payload and command coordinate system, as shown in Table 2.1. The coordinate systems described in Table 2.1 are defined in Figures 2.3, 2.4, and 2.5.

Table 2.1. SRMS Operating Modes

Operating Mode	Point of Resolution (POR)	Coordinate System
Orbiter Unloaded	Tip of End Effector	Orbiter Body Axis System (OBAS) for POR translations Orbiter Rotation Axis System (ORAS) for POR Rotations
Orbiter Loaded	Pre-determined point within payload	Same as above
End Effector	Tip of End Effector	End Effector Operating System (EEOS)
Payload	Pre-determined point within payload	Payload Operating System (PLOS)

2.4.2 Automatic Modes

There are two types of automatic modes: pre-planned automatic sequence and operator commanded automatic sequence. These modes consist of arm trajectories defined by a series of end effector positions and attitudes. These trajectories are designed to keep the arm boom and payload at least five feet from any orbiter or payload structure.

The operator can also control the individual joints via the computer system or via one of the two hardwired systems. Servo motor modules drive the joints through high reduction epicyclical gear trains which produce the desired torque and speed characteristics. Measurements available to the control system include motor rate produced by analog tachometers and joint angles provided by joint encoders. No joint angle rate measurements are available and boom flexibility is not observable in the joint angle measurements. For an unloaded arm, the maximum translational and rotational rates of the end effector are 2.0 ft/sec and 4.76 deg/sec, respectively. The rate limits for a loaded arm varies with payload mass. For a 32,000 lb. payload, the maximum allowable tip velocity of the SRMS is 0.2 ft/sec [5].

2.4.3 Pre-planned Automatic Sequence

On orbit, the GPC will maneuver the arm through the preprogrammed auto sequence selected by the operator. In the pre-planned automatic sequence mode, software compiled prior to launch is used to control automatically the six-jointed arm along a prespecified flight trajectory. This "auto sequence" consists of a series of points. Each sequence is designed for a specific flight, arm, end effector, and payload. The maximum of 20 sequences can be constructed for each flight. There is no limit set for the number of points per sequence. However, the total number of points per flight cannot exceed 200.

Prior to starting the auto sequence, the payload POR must be within a specified distance of the first point, usually two inches and one degree. The SRMS software then calculates a straight line from the current POR for translational motion and an eigenaxis for rotational motion to the next point. Arm dynamics, however, prevents exact straight line motion or precise rotation about the prescribed eigenaxis. The preprogrammed points may be either fly-by or pause points. For fly-by points, the arm will drive toward the point until the POR is within 12 inches and 3 degrees of the point ("fly-by sphere"); then the arm will progress towards the next point. Hence, the position and attitude of the fly-by points may not be achieved. For pause points, the arm will decelerate when the POR reaches the "washout sphere", which is 24 inches and 5.5 degrees around the point. Once the point is reached, the arm stops and the POR remains within two inches and one degree of the pause point until the operator commands the arm to move to the next point. For every sequence, both the initial and the final points are pause points.

2.4.4 Operator Commanded Mode

The operator has direct control of the second type of automatic trajectory. The operator commanded automatic sequence (OCAS) is initiated on orbit. The operator can enter the desired position and attitude of the POR into the GPC via the computer keyboard to maneuver the SRMS. The computer calculates a straight line (both linear and rotational) from the current POR position to the specified point. The GPC will then maneuver the arm to the desired position and attitude. Again, because of arm dynamics, exact straight line motion cannot be achieved. In this mode, there is no collision detection or avoidance system to prevent an incorrect command from causing the arm/payload to contact the orbiter. Hence, each OCAS command must be verified through pre-flight procedure testing, or in-flight through visual inspection by the crew or flight controllers in mission control.

2.4.5 Single Joint, Direct Drive and Backup

The remaining three control modes permit the astronaut to manipulate the arm on a joint-by-joint basis. The single joint mode control algorithms provide joint rate commands to the selected joints, simultaneously requiring the other joints maintain their positions. The commands are given through the D&C panel and routed through the SRMS software. The SRMS software controls the position of all the joints, limits drive speeds, provides joint position displays, and indicates when the joint angles reach their limits. Uncommanded joints maintain their current positions.

The direct drive mode is a contingency mode which supplies rate commands to the selected joint via hardwires, bypassing the SRMS general purpose computer software. To enter the direct drive, the brakes must be engaged. When a joint is selected to drive, that joint's brake is released, while the other brakes remain engaged. After the joint command is taken off, the brake is reapplied and "higher-than-normal" joint rate oscillations occur. System display data may not be available in this contingency mode.

The back-up mode is a contingency mode that is utilized in the event that no primary control mode is operable. This is similar to the direct drive mode; however, the display data and ground downlist is never available.

Chapter 3.

Approach & Theory

Several control methods are possible for maneuvering the SRMS and attached payload. The current system consists of six lead-lag compensators in parallel, which act on the system error dynamics with a low bandwidth design to force the SRMS to follow a prescribed linear trajectory. The approach is simple, but may not provide good transient performance when maneuvering the SRMS and does not provide good vibration damping when precise end effector control is desired. Hence, the speed of manipulations of the SRMS is hindered.

A second approach, suggested in [2], is the design of a linear optimal controller via μ-synthesis [6] for a nominal joint angle configuration while treating all other configurations as structured uncertainty. However, the error in the model due to joint angle variations is real parameter error in the state space coefficient matrices. This, in turn, leads to overly-conservative designs which necessarily have low bandwidth to avoid instability for off-nominal joint configurations. Alternatively, model based compensators such as those investigated by Prakash [2] could be developed for several arm

configurations and gain scheduled. However, this would be extremely cumbersome to implement in the relatively small shuttle computers.

Since the actual dynamics of the SRMS are nonlinear, any linear compensator will exhibit poor transient response and will need to be overly conservative to account for uncertainties due to the important nonlinear dynamics in the controller design.

This chapter describes an approach to controlling the SRMS during trajectory following using the nonlinear dynamics of the plant. The approach, termed "feedback linearization," applies a nonlinear feedback control law in a "inner" feedback loop to cancel plant nonlinear dynamics. The transformed system (the Nonlinear SRMS Plant Dynamics with the Nonlinear Feedback Law) is now linear and a corresponding conventional feedback control law can be designed in an "outer" feedback loop to reject disturbances and provide robustness to unmodeled dynamics, Figure 3.1.

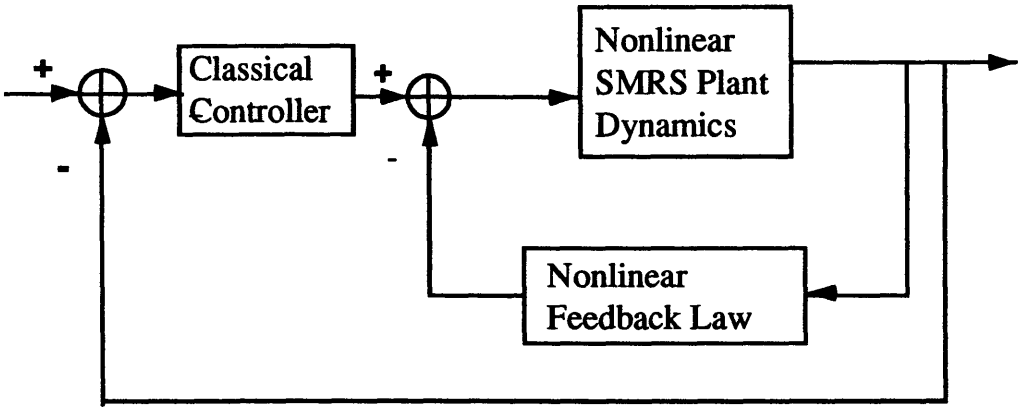

Figure 3.1. Classical controller designed for linearized system

Section 3.1 defines a general nonlinear system, while, section 3.2 discusses nonlinear control issues. Section 3.3 discusses the Taylor series method of linearization. Finally, section 3.4 presents the mathematical notation and definitions that are used in 3.5 and 3.6 for the discussion of feedback linearization concepts.

3.1 Nonlinear Description

The general form of a system of first-order nonlinear ordinary differential equations in state space representation is,

$$\dot{\mathbf{x}}(t) = \mathbf{f}[t, \mathbf{x}(t)] \tag{3.1}$$

where **t** denotes the time; **x(t)** denotes the value of the function **x()** at time **t** and is a *n*-dimensional vector. The vector quantity **x(t)** is referred to as the **state** of the system at time **t**, $\dot{\mathbf{x}}$ is the rate of change of **x** with respect to time ($\frac{\mathbf{dx}}{\mathbf{dt}}$), and **f[t,x(t)]** is a vector-valued nonlinear function of the states and time. Therefore, a typical open loop description of a system with an input function (forcing function) for a nonlinear system is

$$\dot{\mathbf{x}}(t) = \mathbf{f}[t, \mathbf{x}(t)] + \mathbf{g}[t, \mathbf{x}(t)]\mathbf{u}(t), \ \forall t \geq 0 \tag{3.2}$$

where **u(t)** enters linearly and is an *m*-dimensional vector; and the functions **f** and **g** associate, with each value of **t** and **x(t)**, a corresponding *n*-dimensional vector. **u(t)** is called the **input** or the **control** function [7]. Eq. 3.2 is defined as the nonlinear open loop system dynamics. Note that **u**, determined from the control law, is separate from the plant dynamics. **g[t,x(t)]** is a nonlinear function that describes how the controls enter the plant dynamics.

In control system design, the control law, **u**, is chosen so that the states, **x**, can be brought from an arbitrary initial condition to an arbitrary end point, within the workspace of the system dynamics, in a finite amount of time [8]. When applying the control law, the system must also exhibit global asymptotic stability. Stability issues will be discussed in the following section.

3.2 Nonlinear Control Issues

Stabilization and tracking are the two design issues encountered in most (nonlinear) control problems. The stabilization problem involves designing a control system that drives the states of the closed-loop system to a particular equilibrium point. Slotine [9] defines this stabilization/ regulation problem as *finding a control law* $\mathbf{u}$, *for a given nonlinear dynamic system* $\dot{\mathbf{x}} = \mathbf{f}(\mathbf{x},\mathbf{u},\mathbf{t})$, *that sends the state* $\mathbf{x}$, *from any point in a region* Ω *towards* $\mathbf{0}$ *as* $\mathbf{t} \rightarrow \infty$. Position or joint control of the SRMS is an example of a stabilization task.

On the other hand, in the tracking problem, the aim is to develop a control system that forces the closed-loop system to follow a given time-varying trajectory. In [9], the tracking problem is defined as: *for a given nonlinear dynamic system* $\dot{\mathbf{x}} = \mathbf{f}(\mathbf{x},\mathbf{u},\mathbf{t})$, $\mathbf{y} = \mathbf{h}(\mathbf{x})$ *and a desired output trajectory* $,\mathbf{y}_d$ *find a control law for the input* $\mathbf{u}$ *such that, starting from any initial state in a region* Ω, *the tracking error* $\mathbf{y}(\mathbf{t}) - \mathbf{y}_d(\mathbf{t})$ *vanishes while the state* $\mathbf{x}$ *remains bounded.* Manipulating the SRMS to follow a trajectory is a typical tracking problem. The stabilization and tracking problems are often related.

The typical procedure for designing a controller for a nonlinear system is illustrated below in Figure 3.2

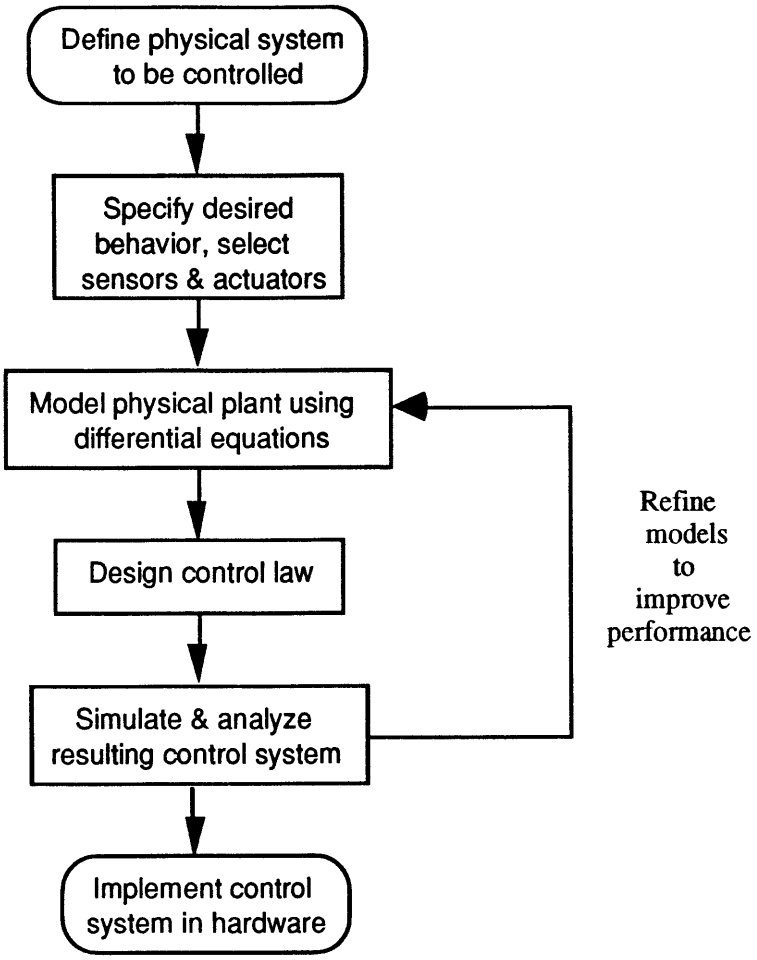

Figure 3.2. Nonlinear Controller Design

Before designing a nonlinear controller, the physical system to be controlled must be defined. Next, performance objectives must be specified. The physical plant is described via differential equations. A nonlinear feedback control law is then derived based on these equations. This is followed by simulation and analysis of the resulting control system. The results may suggest modifying the physical plant model to improve performance. Finally, the control system is implemented.

3.3 Taylor Series Method of Linearization

Linear control systems are "easy" to work with because there are well known methods available to stabilize them. The usual approach, Taylor series linearization method, for dealing with a nonlinear control system is to linearize the system about a particular operating point. If this yields a controllable linear system, then it is possible to stabilize the linear system.

Taylor series linearization, also called Jacobian linearization, deals with the local stability of a nonlinear system. This method provided the justification for using linear control techniques on physical systems by showing that stable control design using the linearized system guarantees the stability of the original nonlinear system[9]. A nonlinear autonomous system defined as $\dot{\mathbf{x}}(t) = \mathbf{f}[\mathbf{x}(t)]$ can be transformed into a locally linear system using the Jacobian.

If $\mathbf{f}$ is continuously differentiable and $\mathbf{f(0)=0}$, where $\mathbf{0}$ is an equilibrium point of the system, then the Jacobian matrix, $\mathbf{J}$, of $\mathbf{f}$ can be evaluated at $\mathbf{x=0}$.

$$\mathbf{J} = \left[\frac{\partial \mathbf{f}}{\partial \mathbf{x}}\right]_{\mathbf{x}=\mathbf{0}} = \begin{bmatrix} \frac{\partial \mathbf{f}_1}{\partial \mathbf{x}_1} & \cdots & \frac{\partial \mathbf{f}_1}{\partial \mathbf{x}_n} \\ \vdots & \ddots & \vdots \\ \frac{\partial \mathbf{f}_n}{\partial \mathbf{x}_1} & \cdots & \frac{\partial \mathbf{f}_n}{\partial \mathbf{x}_n} \end{bmatrix}_{\mathbf{x}=\mathbf{0}} \tag{3.3}$$

The system $\dot{\mathbf{x}} = \mathbf{Jx}$ is the *linearization (linear approximation)* of the original nonlinear system at the equilibrium point x=0. The stability of the linearized system , Table 3.2, is characterized by the eigenvalues of the Jacobian matrix, $\mathbf{J}$.

Table 3.2.

Taylor Series Linearization

Stability of Linearized System	Eigenvalues of J	Equilibrium Point (for nonlinear system)
Strictly Stable	all are strictly in the left-half complex plane	asymptotically stable
Unstable	at least one is strictly in the right-half complex plane	unstable
Marginally Stable	left-half complex plane, at least one is on the jω axis	may be stable, asymptotically stable, or unstable

Taylor series linearization [7,9] implies that, as long as the system is kept "close" to the operating point, the nonlinear system will be stable. Hence, there are limitations such as when the system is not "close" to the operating point with Taylor series linearization method. SRMS maneuvers would require many set points with the associated compensators at each point, thus resulting in a numerically intensive and impractical approach. Also, it is undesirable to use gain scheduling or to have a low bandwidth design for the SRMS controller because these would yield poor transient responses. Therefore, feedback linearization was implemented in the controller design for the SRMS.

3.4 Mathematical Background for Feedback Linearization

Preliminary mathematical tools associated with the development of the feedback linearization control law will be introduced in this section. In the following discussion,

operations will involve scalar functions, $\mathbf{h(x)}:\mathbf{R^n} \rightarrow \mathbf{R}$, and vector functions, $\mathbf{f(x)}:\mathbf{R^n} \rightarrow \mathbf{R^n}$. These functions are called *vector fields*. In the following discussion, only smooth vector fields will be considered, that is, the functions have continuous partial derivatives of arbitrary higher order.

The gradient of the scalar field, $\mathbf{h(x)}$, is denoted by $\nabla \mathbf{h} = \frac{\partial \mathbf{h}}{\partial \mathbf{x}}$; it is represented by a *row-vector* of elements. Similarly, the Jacobian of the vector field, $\mathbf{f(x)}$, is denoted by $\nabla \mathbf{f} = \frac{\partial \mathbf{f}}{\partial \mathbf{x}}$; this is represented by an *(nxn)* matrix of elements. These concepts are used in defining the Lie derivative or directional derivative.

Definition 3.1 *For a smooth scalar field* $\mathbf{h(x)}:\mathbf{R^n} \rightarrow \mathbf{R}$ *and a smooth vector field* $\mathbf{f(x)}:\mathbf{R^n} \rightarrow \mathbf{R^n}$, *the Lie derivative of h with respect to f, denoted by* $\mathbf{L_f h}$, *is a new scalar field defined by:*

$$\begin{aligned} \mathbf{L_f h} &= \nabla \mathbf{h(x) f(x)} \\ &= \sum_{i=1}^{n} \frac{\partial \mathbf{h(x)}}{\partial \mathbf{x_i}} \mathbf{f_i(x)} \end{aligned} \tag{3.4}$$

Repeated Lie derivatives are defined recursively by:

$$\begin{aligned} \mathbf{L_f^0 h} &= \mathbf{h} \\ \mathbf{L_f^i h} &= \mathbf{L_f(L_f^{i-1} h)} = \nabla \mathbf{(L_f^{i-1} h) f} \end{aligned} \tag{3.5}$$

Similarly, if $\mathbf{g}$ is another vector field, then the scalar function $\mathbf{L_g L_f h(x)}$ is

$$\mathbf{L_g L_f h} = \nabla \mathbf{(L_f h) g} \tag{3.6}$$

The concept of Lie derivatives will be used in the derivation of the control law for the feedback linearization.

3.5 Feedback Linearization

With the development of feedback linearization, it is possible to stabilize nonlinear control systems without any linearization about an operating point. It is not like Taylor series linearization, *the nonlinear system is not approximated by a linear system.* The fundamental concept of feedback linearization is to cancel the nonlinearities in a "inner loop" of the nonlinear system so that the closed loop dynamics becomes linear in form. A (classical) linear controller can then be designed in the "outer" loop.

Feedback linearization transforms the nonlinear system into an equivalent controllable linear system. In feedback linearization, a nonlinear system now behaves like a linear system, via feedback control and a transformation of the state vector. Hence, linear control theory can be used to design the appropriate compensation. The resulting linear system, usually a bank of integrators, is invariant over the entire operating envelope, under exact modeling conditions.

In sections 3.5.1 and 3.5.2, two types of feedback linearization will be discussed. The first is Input-State Linearization and the second is Input-Output linearization. Both are fundamentally different from the Taylor series linearization method.

3.5.1 Input-State Linearization

Input-state linearization is a form of feedback linearization. Input state linearization involves solving the feedback linearization problem by finding a state transformation and an input transformation so as to transform the nonlinear system dynamics into an equivalent dynamic system, which can be controller, via nonlinear feedback, into a linear time-invariant system. Then, linear design techniques such as pole placement can be employed to determine the reference input $\mathbf{v}$, which would define the desired trajectory [9]. For a single-input nonlinear system, $\dot{\mathbf{x}} = \mathbf{f}(\mathbf{x},\mathbf{u})$, a state transformation $\mathbf{z}=\mathbf{z}(\mathbf{x})$ and an

input transformation $\mathbf{u}=\mathbf{u}(\mathbf{x},\mathbf{v})$, are found. The equivalent linear time-invariant dynamics have the form $\dot{\mathbf{z}} = \mathbf{A}\mathbf{z} + \mathbf{b}\mathbf{v}$. Slotine [9] defines the criteria for input-state linearization as

Definition 3.2 *A single-input nonlinear system of the form* $\dot{\mathbf{x}} = \mathbf{f}(\mathbf{x}) + \mathbf{g}(\mathbf{x})\mathbf{u}$ *with* $\mathbf{f}(\mathbf{x})$ *and* $\mathbf{g}(\mathbf{x})$ *being smooth vector fields on* $\mathbf{R}^n$, *is input-state linearizable if there exists a region* Ω *in* $\mathbf{R}^n$, *a diffeomorphism* $\phi:\Omega \rightarrow \mathbf{R}^n$, *and a nonlinear feedback control law* $\mathbf{u} = \alpha(\mathbf{x}) + \beta(\mathbf{x})\mathbf{v}$ *such that the new state variables* $\mathbf{z}=\phi(\mathbf{x})$ *and the new input* $\mathbf{v}$ *satisfy a linear time invariant relation* $\dot{\mathbf{z}} = \mathbf{A}\mathbf{z} + \mathbf{b}\mathbf{v}$. $\mathbf{A}$ *and* $\mathbf{b}$ *are of the form*

$$\mathbf{A} = \begin{bmatrix} 0 & 1 & 0 & 0 & \cdots & 0 \\ 0 & 0 & 1 & 0 & \cdots & 0 \\ 0 & 0 & 0 & 1 & \cdots & 0 \\ \cdots & \cdots & \cdots & \cdots & \cdots & \cdots \\ 0 & 0 & 0 & 0 & \cdots & 1 \\ 0 & 0 & 0 & 0 & \cdots & 0 \end{bmatrix}, \mathbf{b} = \begin{bmatrix} 0 \\ 0 \\ 0 \\ \vdots \\ 0 \\ 1 \end{bmatrix}$$

All the poles of the transformed system (determined from the characteristic polynomial, $\det[sI-A]=s^{(n)}$ are at the origin and there are no system zeros. This yields a decoupled set of integrators and the concept can be extended beyond SISO systems [10].

It can be shown [9] that the control law for an input-state linearization problem is of the form

$$\mathbf{u} = \frac{(-\mathbf{L}_f^n \mathbf{z}_1 + \mathbf{v})}{(\mathbf{L}_g \mathbf{L}_f^{n-1} \mathbf{z}_1)} \tag{3.7}$$

which yields

$$\dot{\mathbf{z}}_n = \mathbf{v} \tag{3.8}$$

The closed-loop system using input-state linearization is presented in Figure 3.3. There are two feedback loops in this system, an inner loop to linearize the input-state relation, and an outer loop to control to specifications the overall closed-loop dynamics.

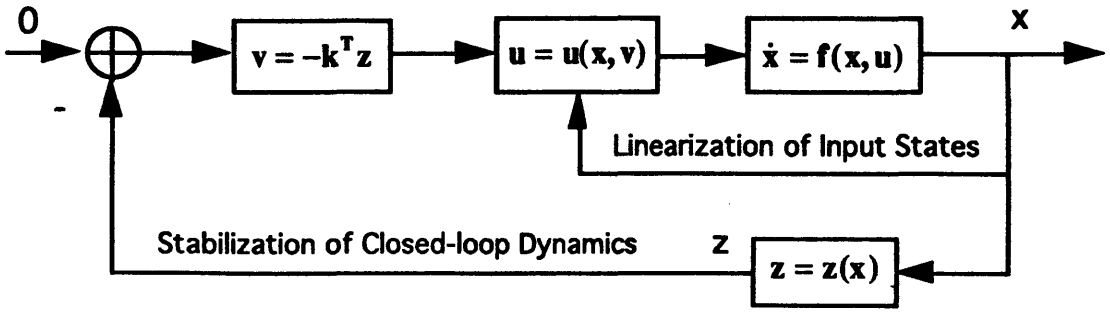

Figure 3.3 Input-State Linearization

Slotine [9] remarks that, in using input-state linearization, if the initial state is at a singularity point, the controller cannot bring the state to the equilibrium point. Hence, although the result is valid over a large region in the state space, it may not always be global. Thus, we have the discussion between a global diffeomorphism (transformation) and a local one, which in turn influence the region of validity of such a total linearization procedure.

3.5.2 Input-Output Linearization

The second type of feedback linearization is often considered when dealing with the tracking problem, for a nonlinear system of the form

$$\dot{\mathbf{x}} = \mathbf{f}(\mathbf{x},\mathbf{u})$$
$$\mathbf{y} = \mathbf{h}(\mathbf{x}) \qquad (3.9)$$

For the tracking problem, it is desired to make the output, $\mathbf{y(t)}$, track a given trajectory, $\mathbf{y_d(t)}$. From Eq. 3.9 , it is obvious that the output $\mathbf{y(t)}$ is only indirectly related to the input $\mathbf{u}$, through the state variables. If it is possible to identify a direct and simple

relation between the system input and output, the tracking problem would be easier to solve. This issue motivates the input-output linearization approach, which does not require a full state transformation and it does not, therefore, yield total system linearization.

In order to generate a direct relation between the output **y** and the input **u**, the output function **y** is differentiated repeatedly until the input appears. Then, **u** is designed to cancel the nonlinearities.

Definition 3.3 *The number* **r** *of differentiations required for the input* **u** *to appear is called the relative degree of the system.*

When the input appears in a number **r** of differentiations of the output, up to the system order **n** (i.e. $r \leq n$), then we say the system is of relative degree **r** and the input/output linear system is a well posed problem. The process of repeated differentiations means that we start with $y=h(x)$, differentiate and proceed up until $y^{(r)}$, i.e. until the control input **u** appears on the right-hand side. For $r=1$, we have

$$\dot{y} = \nabla h(f + gu) = L_f h(x) + L_g h(x) u \tag{3.10}$$

If $L_g h(x) \neq 0$ for some $x=x_0$ in a region Ω_x, then, because of continuity, that relation is verified in a finite neighborhood Ω of x_0. The input transformation in Ω becomes

$$u = \frac{1}{L_g h}(-L_f h + v) \tag{3.11}$$

This yields a linear relation between the input and the output, specifically, $\dot{y} = v$. If $L_g h(x) = 0$ for all **x** in Ω_x, it is necessary to differentiate $\dot{y}$ to obtain

$$\ddot{y} = L_f^2 h(x) + L_g L_f h(x) u$$

(3.12)

If $L_g L_f h(x) = 0$ x in Ω_x, differentiation must be performed again and again until for some integer r, $L_g L_f^{r-1} h(x) \neq 0$. The control law becomes

$$u = \frac{1}{L_g L_f^{r-1} h}(-L_f^r h + v)$$

(3.13)

This is applied to

$$y^{(r)} = L_f^r h(x) + L_g L_f^{r-1} h(x) u$$

(3.14)

to yield

$$y^{(r)} = v$$

(3.15)

When the system has relative degree $r < n$, the nonlinear system can be transformed using $y, \dot{y}, \ldots, y^{(r-1)}$, into the "normal form", which will allows the internal dynamics and the zero dynamics to be studied [9]. Setting

$$\mu = [\mu_1 \quad \mu_2 \quad \cdots \quad \mu_r]^T = \left[y \quad \dot{y} \quad \cdots \quad y^{(r-1)}\right]^T$$

(3.16)

With the output defined as $y = \mu_1$, the "normal form" of the system becomes

$$\dot{\mu} = \begin{bmatrix} \mu_2 \\ \vdots \\ \mu_r \\ a(\mu, \psi) + b(\mu, \psi) u \end{bmatrix}$$

(3.17)

$$\dot{\psi} = w(\mu, \psi)$$

(3.18)

μ_i and ψ_i are called the *normal coordinates* or *normal states*. The internal dynamics associated with the input-output linearization correspond to the last (**n-r**) equations $\dot{\psi} = \mathbf{w}(\mu, \psi)$ of the normal form. These dynamics generally depend on the output states μ, and are the unobservable dynamics after feedback linearization. By setting the output to zero, in the internal dynamics equation, the zero dynamics are determined. The zero dynamics are defined as $\dot{\psi} = \mathbf{w}(\mathbf{0}, \psi)$.

There are two approaches that can be taken for the SRMS tracking problem. The SRMS plant is comprised of three parts, servo, gearbox, and nonlinear arm dynamics. Chapter 4 provides the details concerning the significant nonlinearities that are found in the nonlinear arm dynamics. Chapter 4 also discusses the linearization of the servo and gearbox models.

The first approach is to use input state linearization around the nonlinear arm dynamics to derive a control law for the "inner" loop. This would allow for the design of a linear controller in the "outer" loop of the SRMS system to compensate for the error in the feedback control law caused by not including the nonlinearities of the servo and gearbox. In this case, all the states are observable and there are no internal dynamics. A pole placement controller can then be designed in the "outer" loop.

This approach is investigated in this thesis; the significant nonlinearities are assumed to be in the nonlinear arm dynamics portion of the SRMS system. The servo and gearbox components are not included in the design of the feedback linearization control law because of the dimension and modeling uncertainty associated with these models.

The alternative approach is to include the nonlinearities of the servo and gearbox in deriving the feedback linearization control law. A control law based on input-output linearization methods could be derived to cancel the plant nonlinearities. The internal dynamics of the system could be found by defining the system in the "normal form" as defined in Eq. 3.17. The stability of these internal dynamics would dictate whether it is possible to designing a compensator for the system. Slotine [9] provides a detailed discussion on how a simple linear pole-placement controller in the outer loop provides local asymptotic stability of the overall system so long as the zero dynamics are locally asymptotically stable.

Chapter 4

SRMS Modeling

A simulation model of the nonlinear SRMS dynamics has been developed in *SIMULINK*. The actual dynamics will replace sensor dynamics during implementation. This simulation model, illustrated in Figure 4.1, contains a representation of the gearboxes, nonlinear arm dynamics, and servos. This simulation model is used in the "outer loop" linear controller design.

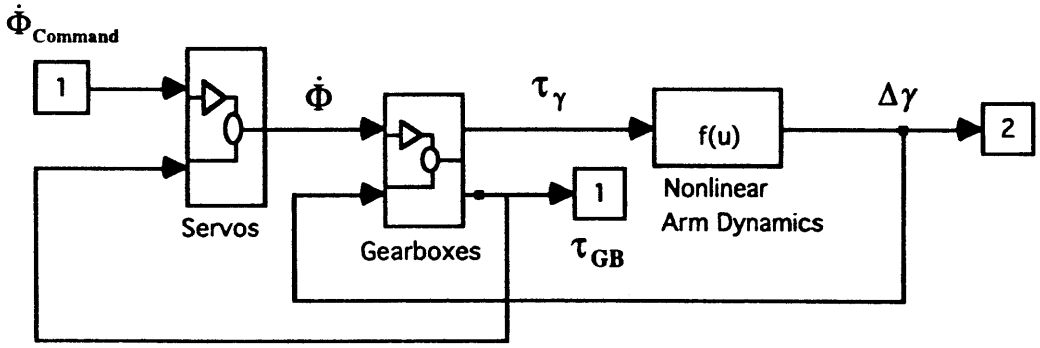

Figure 4.1. Simulation Model - Nonlinear Plant

The gearbox model, described in section 4.1, has a nonlinear stiffness that is linearized in the design model. The gearbox dynamics model the conversion of motor rate into applied joint torque and include a nonlinear stiffness, which represents the flexibility of the gearbox. The nonlinear arm dynamics, outlined in section 4.2, contain the significant nonlinearities. This nonlinear arm dynamics module outputs a joint angle perturbation to a corresponding joint torque.

The servos, described in section 4.3, contain delays and limiters which are ignored in this implementation of the model. The individual joint servos provide a motor rate consistent with the controller generated motor rate command. All of the six joint servos and gearboxes are independent of each other (i.e. single input, single output). Boom flexibility has not been included in the models and will be treated as uncertainty when the feedback compensation is designed.

Each servo is a seventh order system that contains several high frequency poles. These poles do not affect the controller design; however, they do require smaller integration steps of 0.001 sec which increases the computation time. Therefore, the frequency weighted Balance and Truncate model reduction technique was implemented to eliminate the high frequency poles and reduce each servo model to second order. This second order servo model reduces the computation time because it requires an integration step size of 0.1 sec. Section 4.4 discusses the procedure used to reduce the servo models, while section 4.5 illustrates the results from this procedure.

In order to develop a simulation model that is implementable in the relatively small flight computers of the shuttle, the servo and gearbox models were linearized. The nonlinear dynamics are also reduced to allow development of a simplified feedforward control. This procedure is described in section 4.6. The nonlinearities of the servos and gearboxes

are not included in the feedforward terms, but are accounted for by the "outer loop" feedback compensator design.

Table 4.1. Variable Notation for Simulation Model - Nonlinear Plant

Variable	Description
$\dot{\Phi}$	Input : Commanded Motor Rate
τ_γ	Output: Joint Torque
τ_{GB}	Output: Gearbox Torque
$\Delta\gamma$	Output: Change in Joint Angle

4.1 Gearbox Model

The block diagram for the gearbox model of each joint [11] is presented in Figure 4.3. A state space description of this system is generated via *SIMULINK*. The input to each gearbox is motor rate from the servos, and the change in joint angle, $\Delta\gamma$, which is fed back from the arm dynamics module. This is done to model the "twist" angle or the shaft deflection between the motor side and the joint side.

The actual gearbox stiffness gain, **KG**, is the slope of the curve at a particular gearbox torque, τ_γ, and deflection angle vector, $\phi - \gamma$ (motor shaft angle - joint angle). The relation between the gearbox torque and the deflection angle is described in Eq.4.1.

$$\left.\begin{aligned} \tau_\gamma &= \frac{(\phi-\gamma)^2}{4c} \\ c &= \frac{B_L^2}{4T_\Delta^2} \end{aligned}\right\} \tag{4.1}$$

where B_L is the gearbox backlash half angle as seen on the joint side of the gearbox and T_Δ is the gearbox torque at the backlash half angle as seen on the joint side. The values

of B_L and T_Δ for the different joints are presented in Table 4.3. The actual nonlinear stiffness curve for the gearbox is presented in Figure 4.3.

Table 4.3. Variables for Calculation of Actual Gearbox Gain

			JOINTS				
Gains	**Units**	**Shoulder Yaw**	**Shoulder Pitch**	**Elbow Pitch**	**Wrist Pitch**	**Wrist Yaw**	**Wrist Roll**
B_L	radians	1.6872	1.4983	0.8998	0.9222	0.9234	0.9222
T_Δ	ft-lb.	0.1697	0.2035	0.2008	0.3201	0.3206	0.3210

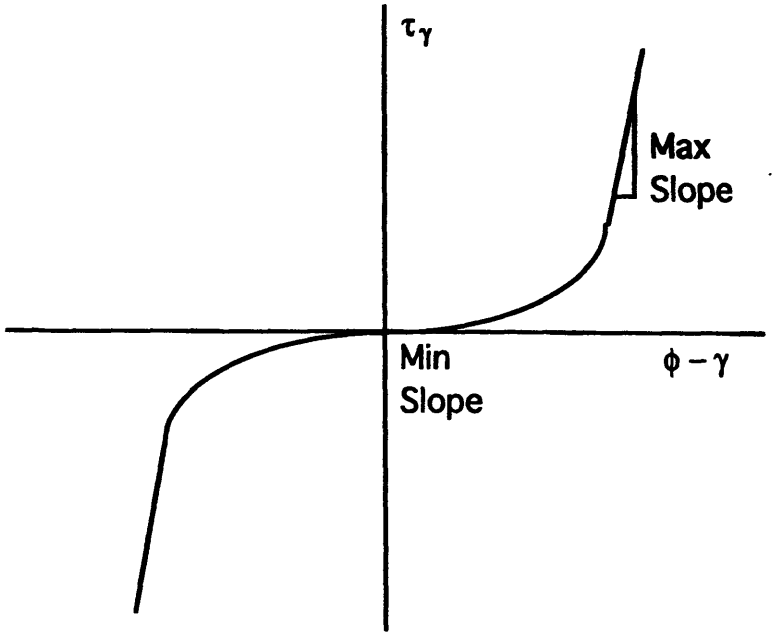

Figure 4.2. Gearbox Nonlinear Stiffness Curve

The nonlinear gearbox can be linearized by substituting the gains for **KG** in Table 4.2[11]. **KG** transforms the deflection angle, denoted by $\phi-\gamma$ in Figure 4.2, into a torque, τ_γ. The gearbox model yields joint torque and gearbox torque; these are obtained from multiplying τ_γ by the gear ratio and gearbox efficiency gains, respectively. **KG** can

range in value between zero and a maximum slope determined by the servos under consideration. The linear values from Table 4.2 that were used for **KG** in the design model fall between the maximum and minimum values of the actual gearbox stiffness gain.

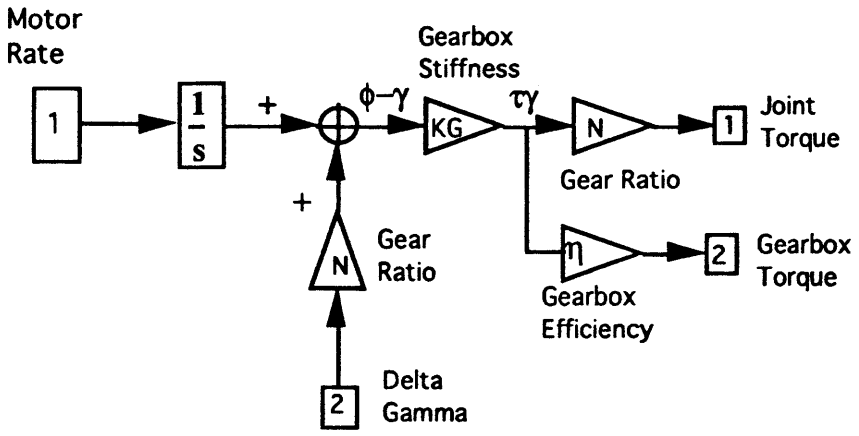

Figure 4.3. Gearbox Model for Nonlinear Plant

Table 4.2. Linear Gains for Gearbox Model

			JOINTS				
Gains	**Units**	**Shoulder Yaw**	**Shoulder Pitch**	**Elbow Pitch**	**Wrist Pitch**	**Wrist Yaw**	**Wrist Roll**
KG	ft-lb./rad	0.3478	0.6212	1.1962	1.9292	1.924	1.9292
N	no dim.	1841.95	1842.95	1260.28	737.74	738.74	737.74
η	no dim.	1.17	1.27	1.20	1.21	1.21	1.21

The controller design model was developed by using the linearized gearbox model. The nonlinear gearbox model was implemented later.

4.2 Nonlinear Arm Dynamics

The equations of motion for the nonlinear model of the SRMS were developed using the Lagrangian approach. The Lagrangian function, **L=T-V**, is first formed, where **T** is the kinetic energy and **V** is the potential energy. Since it is assumed that there are no gravity terms and no rigid body dynamics, **V = 0**. The equations of motion are

$$\mathbf{H(q)\ddot{q} + \dot{H}(q)\dot{q} - \left[\frac{\delta}{\delta q}[T]\right]^T = u} \tag{4.2}$$

Rearranging yields

$$\ddot{\mathbf{q}} = \mathbf{H(q)}^{-1}[-\dot{\mathbf{H}}(\mathbf{q})\dot{\mathbf{q}} + (\frac{\delta}{\delta \mathbf{q}}(\mathbf{T}))^{\mathbf{T}} + \mathbf{u}] \tag{4.3}$$

where $\mathbf{u}_i$ is the vector of joint torques, **H(q)** is the 6X6 composite inertia or mass matrix, while $\dot{\mathbf{q}}$ is the vector of joint rates, $\mathbf{T = 0.5[\dot{q}]^T H(q)\dot{q}}$, and $\dot{\mathbf{H}}(\mathbf{q}) = \sum_{k=1}^{6} \frac{\delta}{\delta \mathbf{q}_k}[\mathbf{H(q)}]\dot{\mathbf{q}}_k$. From these equations, it is possible to generate a state space description of the system, arm dynamics.

4.3 Servo Model

The model for an individual joint servo [12] is presented in Figure 4.4. The servos take as input a motor rate command generated by the controller for each point. The gearbox reaction torque is also modeled as a servo input. The output is motor rate including the appropriate servo dynamic lags. The delays and limiters are ignored in the development of the feed-forward control law. The appropriate servo gains [11] are defined in Table 4.4. Notice that the motor dynamics and tachometer feedback loop contain high frequency dynamics, which can be ignored in the basic design model.

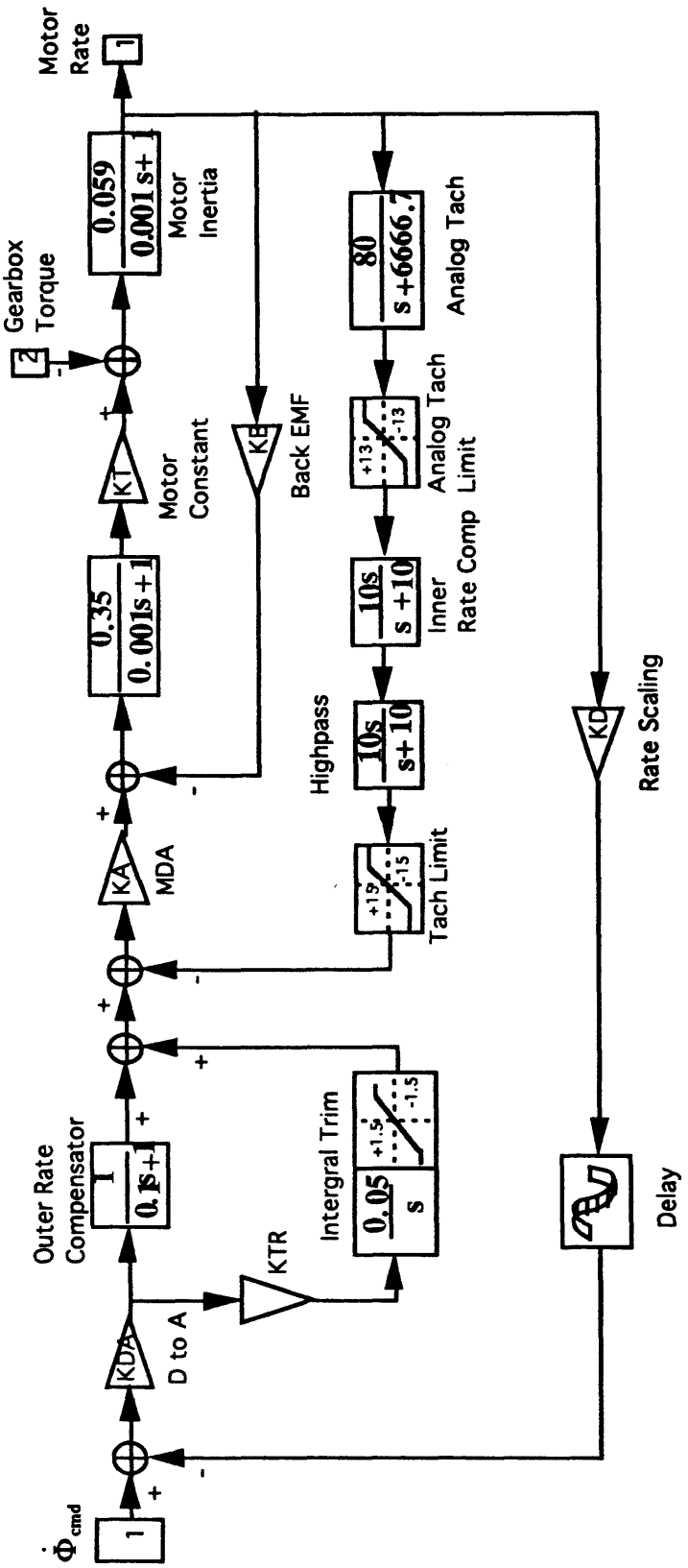

Figure 4.4. Servo Model for Nonlinear Plant

Table 4.4. Gains for Servo

Gains	Units	All Six Joints
KA	Volts/Volt	1.92
KB	Volts/ Radian/Second	0.235
KD	Counts/ Radian/Second	11.378
KDA	Volts/Count	0.1615*
KT	Foot-Pound/Amp	0.17
KTR	$Seconds^{-1}$	0.05*

* for space station sized payloads, KDA for wrist joints is 1.0 and KTR for wrist joints is 0.01 to reflect the upgraded servo power amplifiers.

4.4 Model Reduction for Servos

Each of the six SRMS joints, as shown in Figure 4.4 represents a 7th order system. However, many high frequency modes can be truncated. Model reduction techniques were used to reduce the model for each joint from 7th order to 2nd order.

Moore, [13] describes a model reduction technique which is referred to as "Balance and Truncate." This technique was modified to allow frequency weighting by the method of [14] and then was applied to the servo models described previously. The frequency weighting enables the technique to concentrate on providing good models in a particular frequency range.

4.4.1 Balance and Truncate Model Reduction Technique

The Balance and Truncate technique requires an open-loop stable plant. It uses a state-space representation of the plant in which the controllability and observability grammians are diagonal and equal [13]. The diagonal elements of theses grammians, called Hankel singular values (HSVs), provide the basis for model reduction. Modes that are easily controlled and observed are represented by large Hankel singular values, while modes that are difficult to control and observe are represented by small Hankel singular values. Thus, the state space can be partitioned into strongly and weakly controllable/ observable modes, and the subspace of weakly controllable/ observable modes may be deleted [13].

The Balance and Truncate method uses a state space model of the form

$$\begin{aligned} \dot{\mathbf{x}}(t) &= \mathbf{A}\mathbf{x}(t) + \mathbf{B}\mathbf{u}(t) \\ \mathbf{y}(t) &= \mathbf{C}\mathbf{x}(t) + \mathbf{D}\mathbf{u}(t) \end{aligned} \tag{4.4}$$

where G(s) is

$$\mathbf{G}(s) = \mathbf{D} + \mathbf{C}(s\mathbf{I} - \mathbf{A})^{-1}\mathbf{B} \triangleq \left[\begin{array}{cc} \mathbf{A} & \mathbf{B} \\ \mathbf{C} & \mathbf{D} \end{array}\right] \tag{4.5}$$

A nonsingular state transformation T can be found such that

$$\mathbf{z}(s) = \mathbf{T}\,\mathbf{x}(s) \tag{4.6}$$

which yields another representation of the system G(s)

$$\mathbf{G}(s) = \left[\begin{array}{cc} \mathbf{A} & \mathbf{B} \\ \mathbf{C} & \mathbf{D} \end{array}\right] = \left[\begin{array}{cc} \mathbf{T}^{-1}\mathbf{A}\mathbf{T} & \mathbf{T}^{-1}\mathbf{B} \\ \mathbf{C}\mathbf{T} & \mathbf{D} \end{array}\right] \tag{4.7}$$

By properly selecting T, Moore's balancing techniques can improve the numerical properties of $(\mathbf{TAT}^{-1}, \mathbf{TB}, \mathbf{CT}^{-1})$. The procedure for "properly selecting" T involves using

the controllability grammian, $\mathbf{L_C}$, and observability grammian, $\mathbf{L_O}$. The controllability grammian , $\mathbf{L_C}$, shows the influence of the input on the states, and is given by

$$\mathbf{L_c} = \int_0^\infty \mathbf{exp(At)BB^T exp(A^T t)dt} \tag{4.8}$$

The observability grammian indicates the observability of the states in the output, and is given by

$$\mathbf{L_o} = \int_0^\infty \mathbf{exp(A^T t)C^T C exp(At)dt} \tag{4.9}$$

Solving the matrix Lyapunov equations yields $\mathbf{L_C}$ and $\mathbf{L_O}$

$$\left.\begin{aligned} \mathbf{AL_c + L_c A^T + BB^T = 0} \\ \mathbf{A^T L_o + QL_o + C^T C = 0} \end{aligned}\right\} \tag{4.10}$$

The controllability and observability grammians of $\left(\mathbf{TAT^{-1}, TB, CT^{-1}}\right)$ are related to the grammians of (A,B,C), designated as $\mathbf{L_C}$ and $\mathbf{L_O}$ by

$$\left.\begin{aligned} \overline{\mathbf{L_c}} &= \mathbf{T^{-1} L_c (T^{-1})^T} \\ \overline{\mathbf{L_o}} &= \mathbf{T^T L_o T} \end{aligned}\right\} \tag{4.11}$$

Moore's balancing transformation T is selected such that

$$\overline{\mathbf{L_c}} = \overline{\mathbf{L_o}} \tag{4.12}$$

In order to calculate T, the positive definite $\mathbf{L_C}$ and $\mathbf{L_O}$ can be factored such that

$$\left.\begin{aligned} \mathbf{L_c} &= \mathbf{RR^T} \\ \mathbf{L_o} &= \mathbf{SS^T} \end{aligned}\right\} \tag{4.13}$$

Considering the positive definite matrix

$$\mathbf{H = R^T L_o R} \tag{4.14}$$

Let the singular value decomposition of $\mathbf{S^TR}$ be

$$\mathbf{U_H \Sigma_H V_H = S^T R} \tag{4.15}$$

$$\mathbf{H = V_H \Sigma_H^2 V_H^T} \tag{4.16}$$

where Σ_H is the matrix of Hankel singular values, which provide the basis for model reduction. $\mathbf{U_H}$ is a unitary matrix containing the left singular vectors of $\mathbf{S^TR}$, and $\mathbf{V_H}$ is the corresponding unitary matrix that contains the right singular vectors of $\mathbf{S^TR}$. Since $\mathbf{U_H^T U_H = I}$ and $\mathbf{V_H^T V_H = I}$, selecting

$$\mathbf{T = \dot{R} V_H \Sigma_H^{1/2}} \tag{4.17}$$

yields the desired

$$\overline{\mathbf{L_c}} = \overline{\mathbf{L_o}} = \Sigma_H \tag{4.18}$$

Now it is appropriate to truncate states having small Hankel singular values, which are diagonal elements of Σ_H. The transformed system becomes

$$\mathbf{G(s)_{Full}} = \begin{bmatrix} \mathbf{T^{-1}AT} & \mathbf{T^{-1}B} \\ \mathbf{CT} & \mathbf{0} \end{bmatrix} = \begin{bmatrix} \hat{\mathbf{A}}_{11} & \hat{\mathbf{A}}_{12} & \hat{\mathbf{B}}_1 \\ \hat{\mathbf{A}}_{21} & \hat{\mathbf{A}}_{22} & \hat{\mathbf{B}}_2 \\ \hat{\mathbf{C}}_1 & \hat{\mathbf{C}}_2 & \hat{\mathbf{D}} \end{bmatrix} \tag{4.19}$$

Model reduction can be performed on this balanced realization. The first m states, located in the top left corner of the $\hat{\mathbf{A}}$ matrix, are kept; all others are truncated depending on Σ_H. The reduced system, given in Eq. 4.20, has truncated modes and relatively small approximation errors, σ_H

$$\mathbf{G(s)_{Reduced}} = \begin{bmatrix} \hat{\mathbf{A}}_{11} & \hat{\mathbf{B}}_1 \\ \hat{\mathbf{C}}_1 & \hat{\mathbf{D}} \end{bmatrix} \tag{4.20}$$

The upper bound on the approximation error [13] is

$$\sigma_H = \left\| G_{Full}(s) - G_{Reduced}(s) \right\|_\infty \le 2 \sum_{i=m+1}^{n} \lambda_i, \forall \omega \tag{4.21}$$

where λ_i are the Hankel singular values of the modes that are truncated

4.4.2 Frequency Weighted Balancing Technique

Using model reduction techniques such as Balance and Truncation with unweighted balancing " spreads out" the approximation errors evenly over all frequencies. In some cases, it is desirable to emphasize certain frequency bands at the expense of others. Enns[14] developed a frequency weighted balancing technique. Input, $W_i(s)$, and output, $W_o(s)$, weighting functions are incorporated into the model according to the method described in [14], see Figure 4.5.

$$W_i(s) = \begin{bmatrix} A_i & B_i \\ C_i & D_i \end{bmatrix} \tag{4.22}$$

$$W_o(s) = \begin{bmatrix} A_o & B_o \\ C_o & D_o \end{bmatrix} \tag{4.23}$$

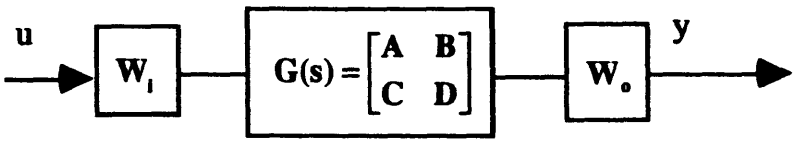

Figure 4.5 Frequency Weighted Balancing at Input and Output

Considering the controllability grammian for the frequency weighted balancing, the augmented system Lyapunov equation becomes.

$$\hat{A}_c \hat{L}_c + \hat{L}_c \hat{A}_c^T + \hat{B}_c \hat{B}_c^T = 0 \tag{4.24}$$

where

$$\hat{A}_c = \begin{bmatrix} A & BC_i \\ 0 & A_i \end{bmatrix} \tag{4.25}$$

$$\hat{B}_c = \begin{bmatrix} BD_l \\ B_l \end{bmatrix} \tag{4.26}$$

The controllability grammian is extracted from the top left corner of the augmented controllability grammian, after solving Eq. 4.24.

$$\hat{L}_c = \begin{bmatrix} L_c & * \\ * & * \end{bmatrix} \tag{4.27}$$

Similarly, considering the observability grammian for the frequency weighted balancing, the augmented system Lyapunov equation becomes.

$$\hat{A}_o^T \hat{L}_o + \hat{L}_o \hat{A}_o + \hat{C}_o^T \hat{C}_o = 0 \tag{4.28}$$

where

$$\hat{A}_o = \begin{bmatrix} A & 0 \\ B_o C & A_o \end{bmatrix} \tag{4.29}$$

$$\hat{C}_o = [D_o C \quad C_o] \tag{4.30}$$

and the observability grammian is extracted from the top left corner of the augmented observability grammian, after solving Eq. 4.28.

$$\hat{L}_O = \begin{bmatrix} L_O & * \\ * & * \end{bmatrix} \tag{4.31}$$

Using $\hat{L}_C$ and $\hat{L}_O$,the same method described for the unweighted case, can be used to solve for **T** in the frequency weighted balancing case.

4.5 Reduced Order Servos

A recent upgrade to the shuttle RMS servo power amplifiers (SPA) has increased the gain values for the digital to analog (KDA) blocks, shown in Figure 4.4, in the three wrist joint servos, by a factor of six. Also, the gain values for the integral trim block (KTR) are five times lower in the three wrist joints due to the same SPA upgrade. Model reduction results both for the shoulder yaw and the wrist pitch joints will be discussed. Other joint reduced order models are obtained in a similar fashion. State space representations for the shoulder yaw servo and wrist pitch servo, shown in Figure 4.4, were generated via *SIMULINK*.

First, a balanced realization without frequency weighting was created for the shoulder yaw servo. Figure 4.6 presents the singular value response of second order reduced model without frequency weighting. The full seventh order model is shown as the solid line, while the reduced second order model is represented as the dashed line. At low frequency, the reduced order model proved to be an inaccurate representation of the full order model because, without frequency weighting, the algorithm spreads the error over all frequencies.

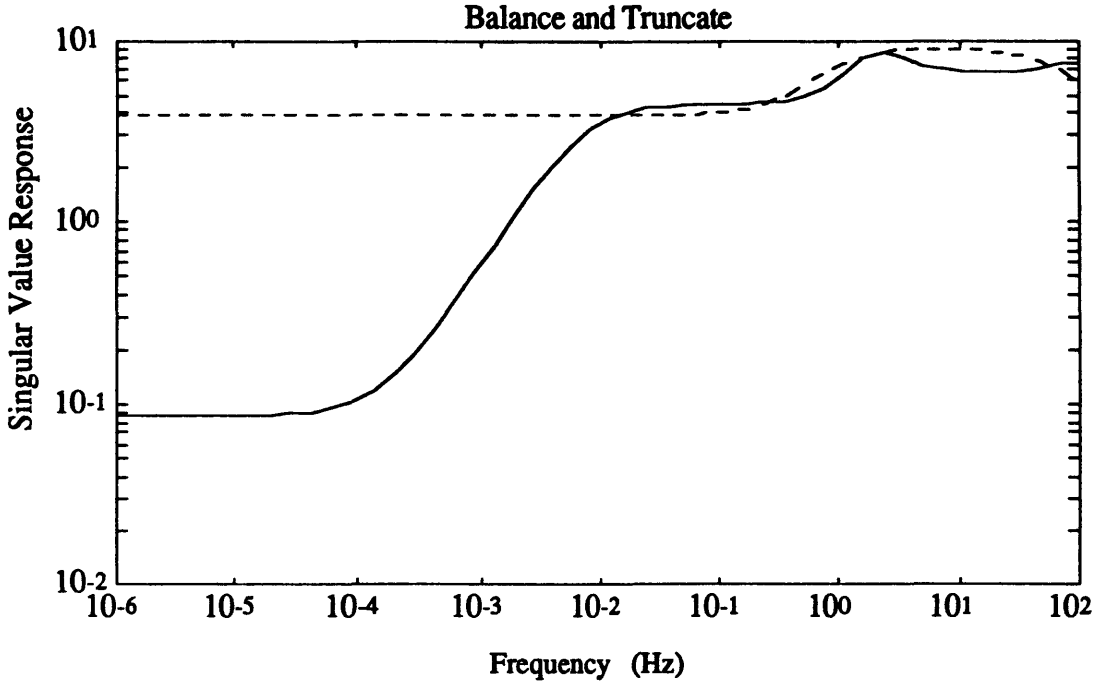

Figure 4.6. Singular Value Response, Model Without Frequency Weighting

A more accurate representation of the full order model was obtained by adding frequency weighting at the output. Table 4. 5 defines the variables used in the frequency weighting procedure.

Table 4.5. Frequency Weighting Filter Description

Type of filter	lowpass
Break frequency	10^{-5} Hz
Order of weight	second
Location of filter	output

Figure 4.7 and Figure 4.8 present the reduced order models with frequency weighting at the output for the shoulder yaw and wrist pitch joints, respectively. Again, the full seventh order model is shown as the solid line, while the reduced second order model is

represented as the dashed line. Now, at low frequency, the reduced order model for both the shoulder yaw and the wrist pitch joints proved to be a nearly perfect match of the full order model.

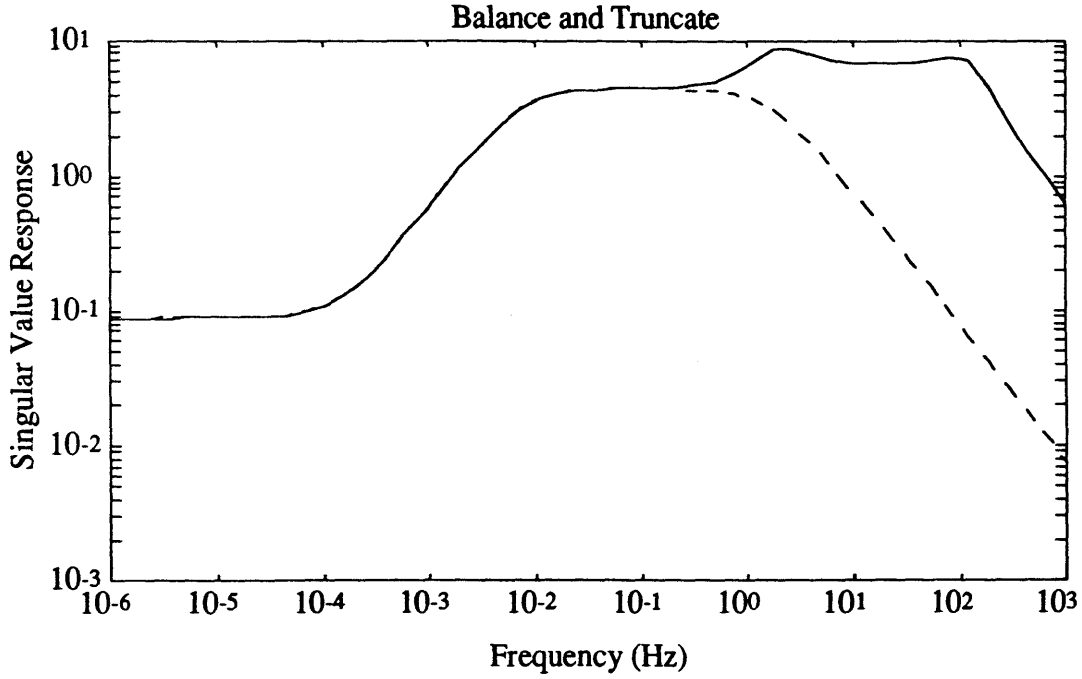

Figure 4.7. Second Order Model of Shoulder Yaw Servo, With Frequency Weighting

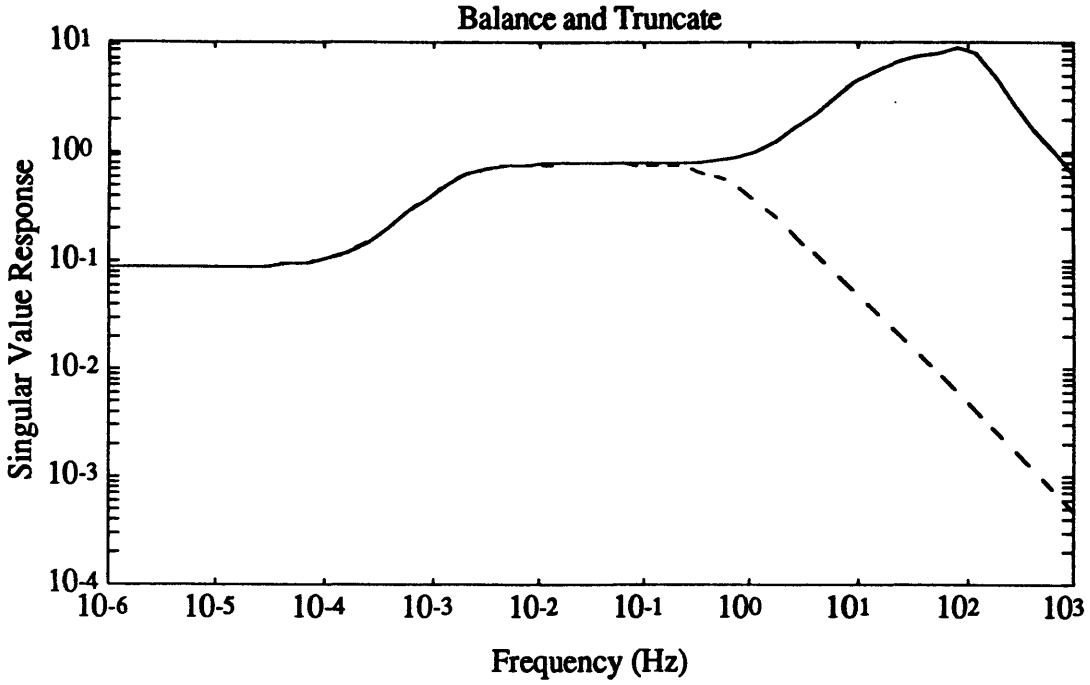

Figure 4.8. Second Order Model of Wrist Pitch Servo, With Frequency Weighting

Poles and zeros of the reduced order model were verified to be stable and minimum phase, respectively. Bode plots , Figure 4.9 and Figure 4.10, individually from the two input channels to the one output were generated for both the shoulder yaw and wrist pitch servos. The solid lines represent the seventh order models, while the dashed lines represent the reduced, second order models. In both channels, the magnitude and phase matched well up to about 0.2 Hz, which is well below the current SRMS controller bandwidth.

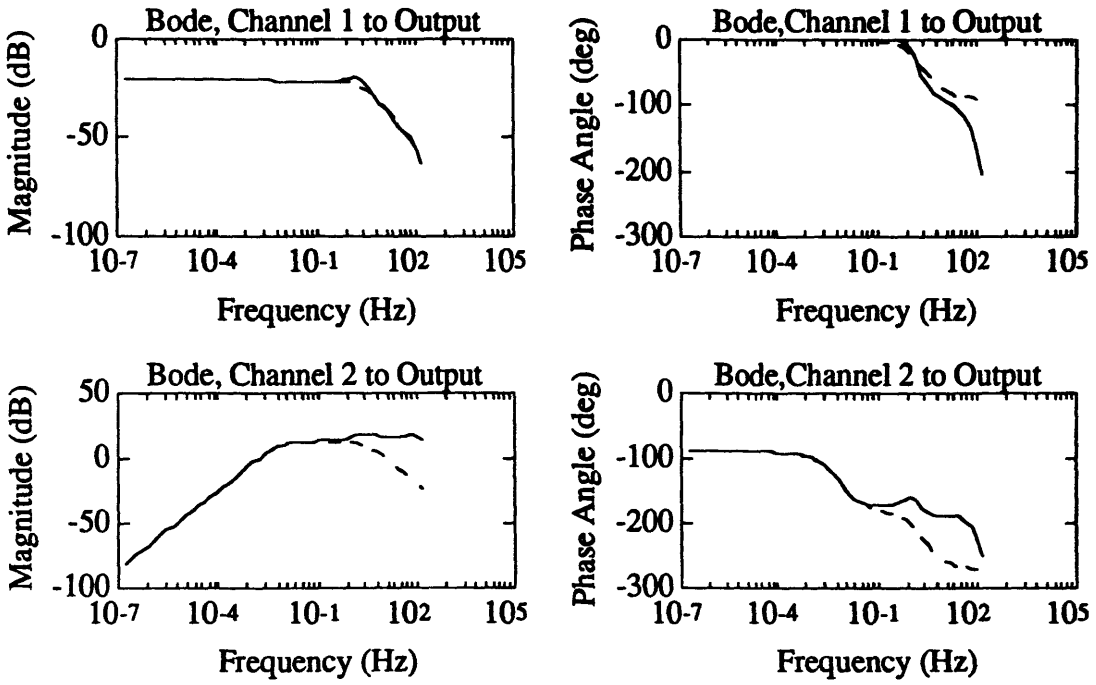

Figure 4.9. Bode Plots for Shoulder Yaw Servo Model with Frequency Weighting

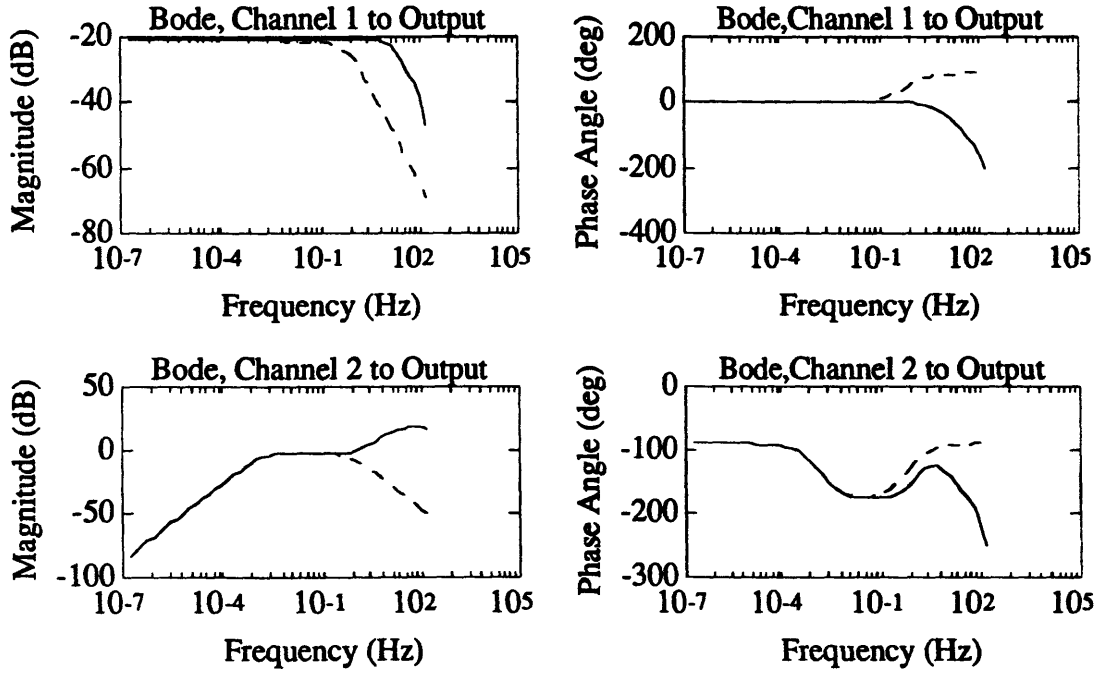

Figure 4.10. Bode Plots for Wrist Pitch Servo Model with Frequency Weighting

Figure 4.11 illustrate the singular value response for all six joints. The solid curves represent the full 42nd order model, while the dashed curves represent the reduced 12th order model.

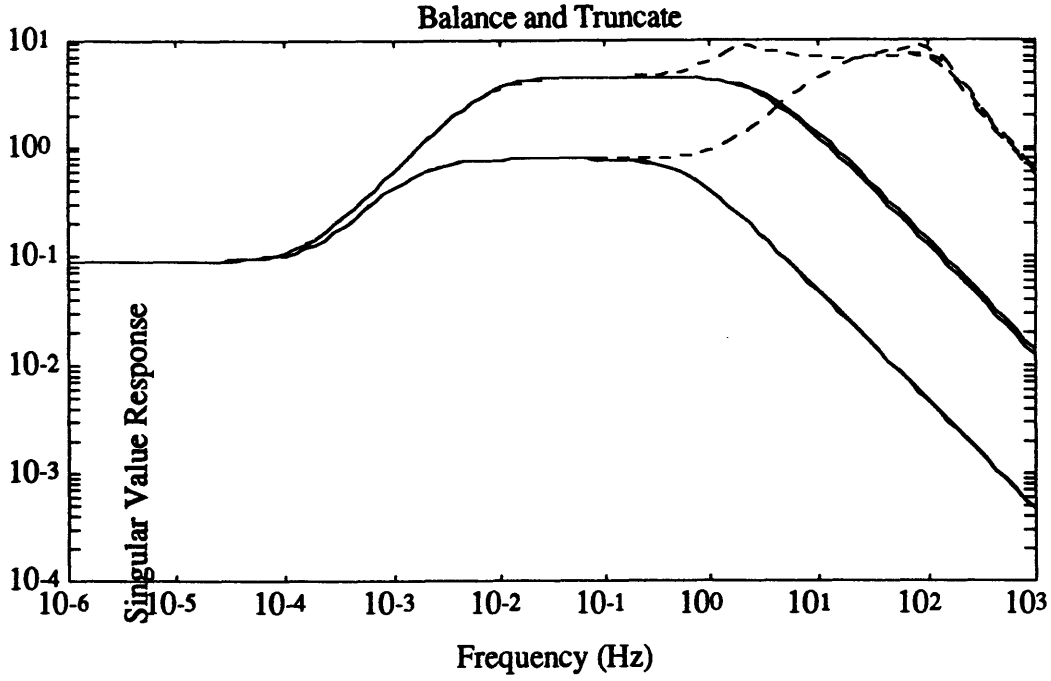

Figure 4.11. 12th Order Reduced Model of Servos

The Balance and Truncate model reduction technique that was used eliminated high frequency modes of the system. The second order reduced model had modes below 20 Hz, whereas in the full system model there was a mode at 6760 Hz. Eliminating high frequency modes results in being able to integrate with larger step sizes. Because the plant dynamics are nonlinear, it is necessary to use the computationally intensive fourth order Runge-Kutta integration method. By using larger step sizes for the integration (of 0.1 sec), the computation time is drastically reduced.

4.6 Model Reduction for Nonlinear Plant

The equations of motion for the SRMS described in section 4.2 also result in computationally intensive calculations of the link composite inertia matrices. A technique for reducing the model of the nonlinear plant which involved considering the predominant composite inertia matrix over the reach space of the SRMS was used. Figure 4.12, Table 4.6 and 4.7 present the reach limits and joint rate limits, for each joint of the SRMS, that were used to search for the dominant composite inertia matrices.

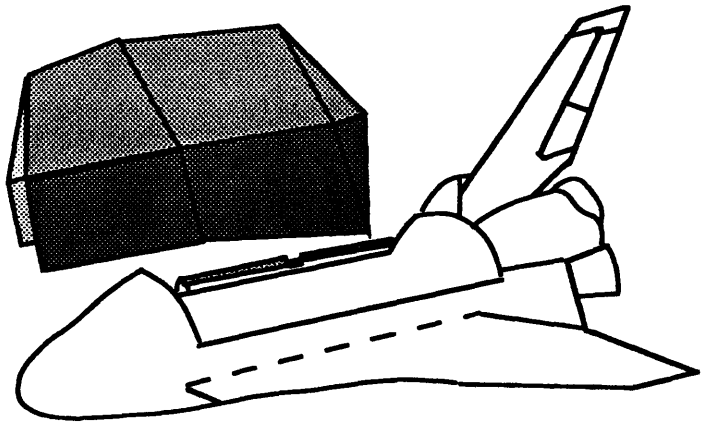

Figure 4.12. Reach Space of SRMS

Table 4.6. Reach Limits of the SRMS

Joint	Reach Limit	
Shoulder Yaw	+175.4°	-175.4°
Shoulder Pitch	+2.6°	+140.4°
Elbow Pitch	-2.4°	-155.6°
Wrist Pitch	-114.4°	+114.4°
Wrist Roll	-114.6°	+114.6°
Wrist Yaw	-440.0°	+440.0°

Table 4.7. Rate Limits for SRMS

Unloaded I-load	Units	Shoulder Yaw	Shoulder Pitch	Elbow Pitch	Wrist Pitch	Wrist Yaw	Wrist Roll
JRL_PL Coarse	Degrees/ second	2.29	2.29	3.21	4.76	4.76	4.76
JRL_PL Vernier	Degrees/ second	0.229	0.229	0.321	0.476	0.476	0.476

Composite inertia matrices were computed over the state space of joint angles and joint rates. The norms of these matrices were compared over the different joint configurations and joint rates. Typical values of the norms for the different configurations are presented in Table 4.8. These values are normalized over the six joint inertia and payload inertia.

Table 4.8. Norms of Composite Inertia Matrices in SRMS Reach Space

Joints	Configuration A	Configuration B	Configuration C	Configuration D	Configuration E
Shoulder Yaw	1.4283e-07	9.1038e-08	1.5194e-07	2.2052e-07	3.1918e-07
Shoulder Pitch	5.7985e-04	3.6959e-04	6.1685e-04	8.9527e-04	1.2958e-03
Elbow Pitch	2.5585e-03	1.3198e-03	9.5599e-04	1.0211e-03	2.3375e-03
Wrist Pitch	4.6649e-04	2.4499e-04	1.7218e-04	2.0276e-04	3.7978e-04
Wrist Roll	2.5660e-03	1.4887e-03	1.0619e-03	1.3043e-03	1.8185e-03
Wrist Yaw	2.5871e-03	1.6673e-03	1.2228e-03	1.5591e-03	1.5690e-03
Payload	**9.9124e-01**	**9.9491e-01**	**9.9597e-01**	**9.9502e-01**	**9.9260e-01**

In all cases the composite inertia matrix for the SRMS links were insignificant compared with the composite Inertia matrix for the payload. Hence, a suitable reduced order nonlinear system only considers the composite inertia matrix for the payload represented in a shuttle fixed frame.

Chapter 5

Controller Design and Analysis

Using the approach presented in Chapter 3, the nonlinear feedback control law is derived in this chapter. Next, implementation of the feedback control law is discussed. Details about Spar Aerospace's lead-lag controller are also included in this chapter.

5.1 Derivation of the Control Law

Recall from the EQ. 4.3, the equations of motion for the nonlinear arm dynamics

$$\ddot{\mathbf{q}} = \mathbf{H}(\mathbf{q})^{-1}[-\dot{\mathbf{H}}(\mathbf{q})\dot{\mathbf{q}} + (\frac{\partial}{\partial \mathbf{q}}(\mathbf{T}))^{\mathbf{T}} + \mathbf{u}] \tag{5.1}$$

Let the state vector be defined as

$$\mathbf{x} = \begin{bmatrix} \mathbf{x}_1 \\ \mathbf{x}_2 \end{bmatrix} = \begin{bmatrix} \mathbf{q} \\ \dot{\mathbf{q}} \end{bmatrix} \tag{5.2}$$

then

$$\dot{\mathbf{x}} = \begin{bmatrix} \dot{\mathbf{q}} \\ \ddot{\mathbf{q}} \end{bmatrix} = \begin{bmatrix} \mathbf{x}_2 \\ \mathbf{H}(\mathbf{x}_1)^{-1}[-\dot{\mathbf{H}}(\mathbf{x}_1)\mathbf{x}_2 + (\frac{\mathbf{d}}{\mathbf{dq}}(\mathbf{T}))^{\mathbf{T}} + \mathbf{u}] \end{bmatrix} \tag{5.3}$$

In the feedforward control calculation we have ignored the process noise, measurement noise, and servo and gearbox nonlinearities. The system can be represented as

$$\left.\begin{aligned} \dot{\mathbf{x}} &= \mathbf{f}(\mathbf{x}) + \mathbf{g}(\mathbf{x})\mathbf{u} \,|\, \cdots + \mathbf{F}\mathbf{w} \\ \mathbf{y} &= \mathbf{h}(\mathbf{x}) \,|\, \cdots + \mathbf{v} \end{aligned}\right\} \tag{5.4}$$

Fw represents the process noise while **v** represents the measurement noise. Here, **u** represents joint torque, which is achieved by commanding the motors to produce the desired torque. The joint servos and gearboxes are a high speed inner control loop that achieves the desired motor rate commands and joint torques. Nonlinearities existing in these components are taken into consideration by an outer loop feedback controller. The feed forward terms computed from the nonlinear arm dynamics become

$$\left.\begin{aligned} \mathbf{f}(\mathbf{x}) &= \begin{bmatrix} \mathbf{x}_2 \\ \mathbf{H}(\mathbf{x}_1)^{-1}[-\dot{\mathbf{H}}(\mathbf{x}_1)\mathbf{x}_2 + (\frac{\mathbf{d}}{\mathbf{dq}}(\mathbf{T}))^{\mathbf{T}}] \end{bmatrix} = \begin{bmatrix} \mathbf{f}_1(\mathbf{x}) \\ \mathbf{f}_2(\mathbf{x}) \end{bmatrix} \\ \mathbf{g}(\mathbf{x}) &= \begin{bmatrix} \mathbf{0}_{n/2 \mathrm{X} m} \\ \mathbf{H}(\mathbf{x}_1)^{-1} \end{bmatrix} = \begin{bmatrix} \mathbf{g}_1(\mathbf{x}) \\ \mathbf{g}_2(\mathbf{x}) \end{bmatrix} \\ \mathbf{y} &= \mathbf{h}(\mathbf{x}) = \mathbf{x}_1 \end{aligned}\right\} \tag{5.5}$$

where n is the state dimension and m is the number of controls. Only the joint angles are measured. The joint rates must be estimated or the command must be fed forward. Both options will be examined. The servo lags will determine whether the feedforward command rates will allow satisfactory performance.

x, f and **g** are smooth vector fields and **h** is a smooth nonlinear function. Differentiating **y** with respect to time yields

$$\dot{\mathbf{y}} = \frac{\partial \mathbf{h}}{\partial \mathbf{x}}\mathbf{f}(\mathbf{x}) + \frac{\partial \mathbf{h}}{\partial \mathbf{x}}\mathbf{g}(\mathbf{x})\mathbf{u}$$
$$= \mathbf{L}_f\mathbf{h}(\mathbf{x}) + \mathbf{L}_g\mathbf{h}(\mathbf{x})\mathbf{u}$$

(5.6)

If $\mathbf{L}_g\mathbf{h}(\mathbf{x})$ is bounded away from zero for all $\mathbf{x}$, then the state feedback law would take the form of

$$\mathbf{u} = \frac{\mathbf{1}}{\mathbf{L}_g\mathbf{h}(\mathbf{x})}(-\mathbf{L}_f\mathbf{h}(\mathbf{x}) + \mathbf{v})$$
$$\mathbf{u} = \alpha(\mathbf{x}) + \beta(\mathbf{x})\mathbf{v}$$

(5.7)

The new linear system from the input $\mathbf{v}$ to the output $\mathbf{y}$ would be

$$\dot{\mathbf{y}} = \mathbf{v}$$

(5.8)

Thus, the feedback control law has the effect of making (n-1) of the system states unobservable.

If for all values of $\mathbf{x}$, $\mathbf{L}_g\mathbf{h}(\mathbf{x}) \equiv \mathbf{0}$, then it is necessary to differentiate the equation for $\dot{\mathbf{y}}$

$$\ddot{\mathbf{y}} = \mathbf{L}_f^2\mathbf{h}(\mathbf{x}) + \mathbf{L}_g\mathbf{L}_f\mathbf{h}(\mathbf{x})\mathbf{u}$$

(5.9)

recall that $\mathbf{L}_f^2\mathbf{h}(\mathbf{x}) \equiv \mathbf{L}_f(\mathbf{L}_f\mathbf{h})(\mathbf{x})$ and $\mathbf{L}_g\mathbf{L}_f\mathbf{h}(\mathbf{x}) \equiv \mathbf{L}_g(\mathbf{L}_f\mathbf{h}(\mathbf{x}))$. This time, if for all values of $\mathbf{x}$, $\mathbf{L}_g\mathbf{L}_f\mathbf{h}(\mathbf{x})$ is bounded away from zero, then the control law is given by

$$\mathbf{u} = \frac{\mathbf{1}}{\mathbf{L}_g\mathbf{L}_f\mathbf{h}(\mathbf{x})}(-\mathbf{L}_f^2\mathbf{h}(\mathbf{x}) + \mathbf{v})$$

(5.10)

and the linearized input-output system is

$$\ddot{\mathbf{y}} = \mathbf{v}$$

(5.11)

A general expression for the control law can be derived. If γ (order of differentiations) is the smallest integer for which $\mathbf{L_g L_f^i h(x)} \equiv \mathbf{0}$ for i=0, ...,γ-2 and $\mathbf{L_g L_f^{\gamma-1} h(x)}$ is bounded away from zero, then the control law is given by

$$\mathbf{u} = \frac{\mathbf{1}}{\mathbf{L_g L_f^{\gamma-1} h(x)}} (-\mathbf{L_f^{\gamma} h(x)} + \mathbf{v})$$

(5.12)

This yields

$$\mathbf{y^{\gamma} = v}$$

(5.13)

In the case of the nonlinear arm dynamics for the SRMS, differentiating the output until the input states appears yield:

$$\left.\begin{aligned} \dot{\mathbf{y}} &= \underbrace{\mathbf{f_1(x)}}_{\mathbf{L_f h(x)}} + \underbrace{\mathbf{0}}_{\mathbf{L_g h(x)}} \mathbf{u} \\ \ddot{\mathbf{y}} &= \underbrace{\mathbf{f_2(x)}}_{\mathbf{L_f^2 h(x)}} + \underbrace{\mathbf{g_2(x)}}_{\mathbf{L_g L_f h(x)}} \mathbf{u} \end{aligned}\right\}$$

(5.14)

Since for all $\mathbf{x}$, $\mathbf{L_g L_f h(x)} \neq \mathbf{0}$ the new input $\mathbf{v}$ can be defined by

$$\mathbf{v = f_2(x) + g_2(x) u}$$

(5.15)

Letting $\ddot{\mathbf{y}} = \mathbf{v}$, and solving for the feedforward term yields

$$\mathbf{u} = -\mathbf{g_2(x)^{-1} f_2(x)} + \mathbf{g_2(x)^{-1} v}$$

(5.16)

The linear control, $\mathbf{v}$, represents joint accelerations derived from the outer loop (i.e., the loop which corrects errors due to the servo/gearbox nonlinearities and process noise)

error dynamics. $\mathbf{f_2(x)}$ is the joint acceleration required to cancel the nonlinear arm dynamics. $\mathbf{g_2(x)^{-1}}$ converts joint acceleration to joint torque.

Substituting Eq. 5.16 into Eq. 5.5 the gives

$$\left.\begin{aligned}\dot{\mathbf{x}} &= \begin{bmatrix}\mathbf{f_1(x)}\\ \mathbf{f_2(x)}\end{bmatrix} + \begin{bmatrix}\mathbf{g_1(x)}\\ \mathbf{g_2(x)}\end{bmatrix}\left[-\mathbf{g_2(x)^{-1}f_2(x)} + \mathbf{g_2(x)^{-1}v}\right]\\ \mathbf{y} &= \mathbf{x_1} + \mathbf{v}\end{aligned}\right\} \tag{5.17}$$

from which a state space representation of the "feedback linearized" system can be derived. This state space representation (which is a series of integrators)is now linear from the new control **v** to the output **y**.

$$\left.\begin{aligned}\dot{\mathbf{x}} &= \begin{bmatrix}\mathbf{0} & \mathbf{I}\\ \mathbf{0} & \mathbf{0}\end{bmatrix}\mathbf{x} + \begin{bmatrix}\mathbf{0}\\ \mathbf{I}\end{bmatrix}\mathbf{v}\\ \mathbf{y} &= \begin{bmatrix}\mathbf{I} & \mathbf{0}\end{bmatrix}\mathbf{x}\end{aligned}\right\} \tag{5.18}$$

5.2 Implementation of the Control Law

Referring to Figure 5.1, the error dynamics are computed by differentiating the steering command and the joint encoder angle measurements which are being fed back. In the current system, a simple lead/lag compensator acts on the joint angle error in each joint to produce a joint rate command which is transformed into a digital motor rate command by a conversion factor. This conversion factor consists of the product of gear ratio (N) and digital tachometer gain (KD). The numerical values for N and KD are presented in Tables 4.2 and 4.4, respectively.

The joint servos produce the desired motor rate or joint torque subject to their internal lags. The feedforward joint acceleration term $\mathbf{f_2(x)}$ is computed by feeding back the joint angles γ and estimating joint rate using motor rate feedback. Alternatively, the commanded joint rate maybe used in this calculation, if servo time constants are small relative to the important arm dynamics.

The feedback compensator, K(s), must now be designed to provide good performance in the presence of disturbances and to provide stability in the presence of unmodeled dynamics. The unmodeled dynamics include boom flexibility, servo control saturations, and gearbox nonlinearities.

Spar Aerospace's Phase 1 Space Station Berthing study concluded that the SRMS position hold mode exhibited unstable joint oscillations with attached payloads greater than 65,000 lb.. mass. The Phase 2 Space Station Berthing Study suggested implementation of a first order lead-lag compensator to stabilize heavy payloads (over 65,000 lb..) [15]. This lead-lag controller is both payload and joint dependent. The transfer function of the compensator is presented in Eq. 5.19.

$$\mathbf{G(s) = K\frac{(1+T_1 s)}{(1+T_2 s)}} \tag{5.19}$$

This transfer function must be converted from continuous time to discrete time in order to be implemented in the SRMS general purpose computer (GPC) software. Using the Tustin approximation for the analog-to-digital conversion, with sampling time T,

$$\mathbf{s = \frac{2}{T}\frac{(1-z^{-1})}{(1+z^{-1})}} \tag{5.20}$$

$$G(z) = \frac{Y(z)}{X(z)} \frac{GF1 + GF2z^{-1}}{1 + GF3z^{-1}} \tag{5.21}$$

Table 5.1 defines the variables presented in equations 5.19 through 5.21.

Table 5.1. Lead-Lag Compensator Gains

Payload MB	K	T(s)	T_1(s)	T_2(s)	GF1 (1/s)	GF2 (1/s)	GF3
3A	0.1	0.08	60	6	0.99404	-0.99272	-0.98675
5B	0.1	0.08	80	8	0.99552	-0.99453	-0.99005
8 & 8'	0.1	0.08	90	9	0.99602	-0.99513	-0.99115

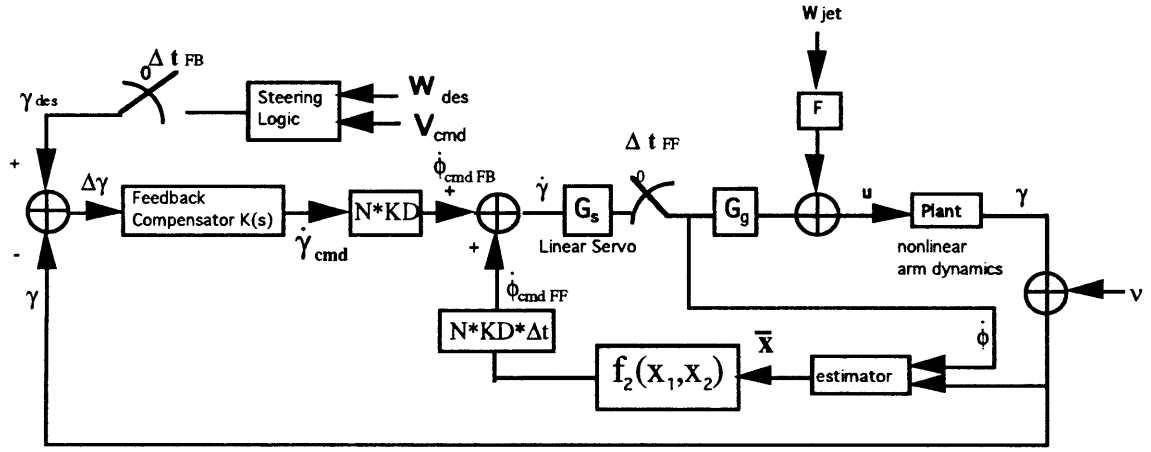

Δt_{FB} = Feed back Command Processing Rate (Outer Loop)
Δt_{FF} = Feed forward Command Processing Rate (Inner Loop)
$\mathbf{w_{jet}}$ = Thruster disturbance
$\mathbf{n}$ = measurement noise
$x_1 = \gamma$ = joint angle
$x_2 = \dot{\gamma}$ = joint rate

Figure 5.1. Linearized Plant Model

A classical control approach can be taken in the design of a controller for the "Linearized System." The goal is to obtain a system that is implementable in the shuttle computers, which have relatively small computing power. The feedback linearization control law presented in Eq. 5.16 was implemented in the "inner loop" for the nonlinear arm dynamics model to yield the "linearized system". Classical loop-shaping methods and robust control techniques can be used to obtain an appropriate design for the "outer loop" compensator. This thesis investigated the design of an LQR compensator and a pole placement compensator.

Chapter 6

Results

The goal of this endeavor is to study the performance of the SRMS system with different controllers and show the effects of feedback linearization. First, the current SRMS controller was studied with and without feedback linearization. Next, a LQR controller was designed for the system without feedback linearization to evaluate the linear controller performance and stability over the state space of a typical SRMS berthing maneuver. Finally, pole placement controller was designed in the outer loop for the system with feedback linearization.

Section 6.1 discusses the performance of the simulation model described earlier with the current position hold controller. A nonlinear model of the arm dynamics was simulated in SIMULINK. In this model, the servos and gearbox models were linearized because the nonlinear arm dynamics contain the significant nonlinearities of the system. The saturations and delays were eliminated from the servo model and the gearbox stiffness was modeled with a linear gain. A feedback linearization control law, derived from the nonlinear arm dynamics was used in the inner feedback loop. The outer feedback loop contained the current position hold controller, which is a lead-lag controller.

Section 6.2 discusses how feedback linearization can improve the performance of the system at high maneuver rate limits. The contribution of the nonlinear feedback term in the joint acceleration for different joint rates is compared with the contribution from the control to the joint acceleration. Next, section 6.3 describes how the steering algorithm is generated and section 6.4 discusses how it is incorporated into the current lead-lag controller system and simulates it using the MB4 SSF berthing trajectory. Section 6.5 discusses the development of the nonlinear gearbox in the SIMULINK model.

Boom flexibility was not included in the design model. Hence, a low bandwidth controller, such as the current lead-lag controller, was able to stabilize the design model at low rates over the designated trajectory. However, when boom and gearbox flexibility are considered in the design of the controller, a higher bandwidth controller must be implemented to suppress the vibrations and control the end effector. High bandwidth controllers using proportional-derivative (PD) feedback compensation or LQR compensators use velocity feedback to provide additional lead. Section 6.6 explores the possibility of designing a LQR controller for the system without feedback linearization. This controller would only be expected to stay stable over a certain operating region. Section 6.7 discusses a PD controller using the pole placement technique with the feedback linearization to find a controller that maintains stability over the entire region.

6.1 Current System Performance

A *SIMULINK* model of the current system was generated. The block diagram for this model is presented in Figure 6.1 A trajectory of joint angle histories was generated for the steering command block. Details about the steering algorithm will be presented in section 6.3.

$\Delta\gamma$ is the difference between the commanded joint angle and the actual joint angle γ. It is the input to the current lead-lag controller, described in section 5.2. A state space representation of the current lead-lag controller was used in the *SIMULINK* model. The commanded joint rate from the lead-lag controller is fed to the "g2vneil" function, which is a macro used to apply the feedback linearization "inner loop" control law and convert the commanded joint rates into commanded motor rates. These commanded motor rates, along with the gearbox torque, are inputs to the state space representation of the reduced order servos model (12^{th} order model). The output from the servos block is the actual motor rate. This motor rate, along with the $\Delta\gamma$, are the inputs to the gearbox state space representation. The gearbox block produces joint torque and gearbox torque. The joint torque is fed to the nonlinear arm dynamics block, while the gearbox torque is fedback to the servo block.

"nldyn_simp1" is the macro that uses the nonlinear equations of motion for the SRMS, which were presented in Eq. 4.3, to generate the joint angle. It is also possible to obtain the joint rate from the "nldyn_simp1" macro. However, joint rate measurements do not exist in the actual SRMS; instead, joint rate must be estimated and filtered based on the motor rate.

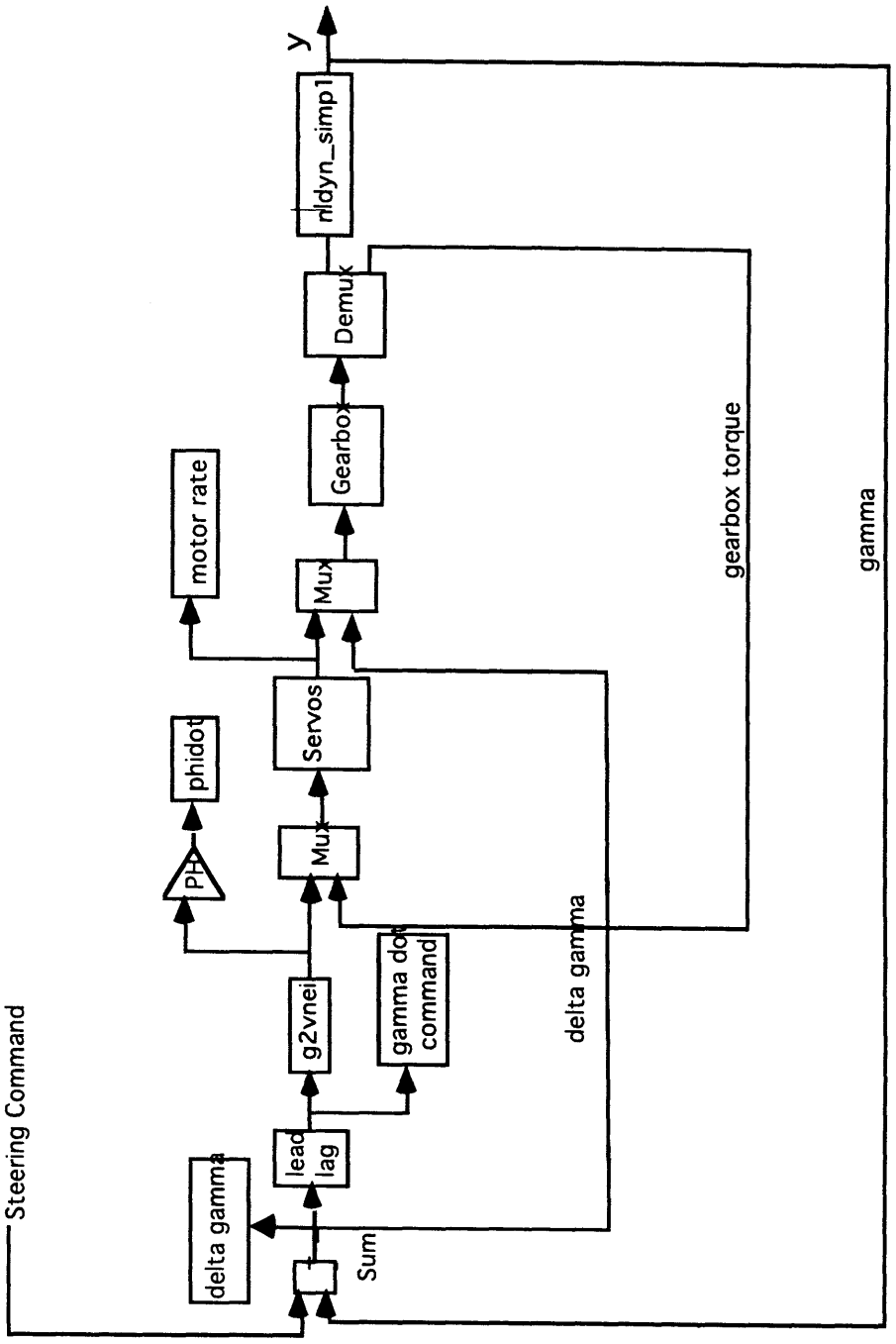

6.1 SIMULINK Model of System

Simulink with Runga Kutta, a fourth/fifth order integration method was used to simulate the system dynamics. A maximum step size of 0.1 sec was used for the integration. The euler method of integration, which was six times faster computationally, was also tried, but proved to be inaccurate.

The lead lag controller used in the current system limits the joint rates by virtue of its low bandwidth. Figures 6.2 and 6.3 present the joint angle and joint rate histories for a step input of 10 degrees in the shoulder yaw joint angle. The joint rates were set to be zero initially. The dotted line represents the input for each joint. The oscillatory nature is due to the lack of friction in the model; there is no damping modeled in the nonlinear dynamics.

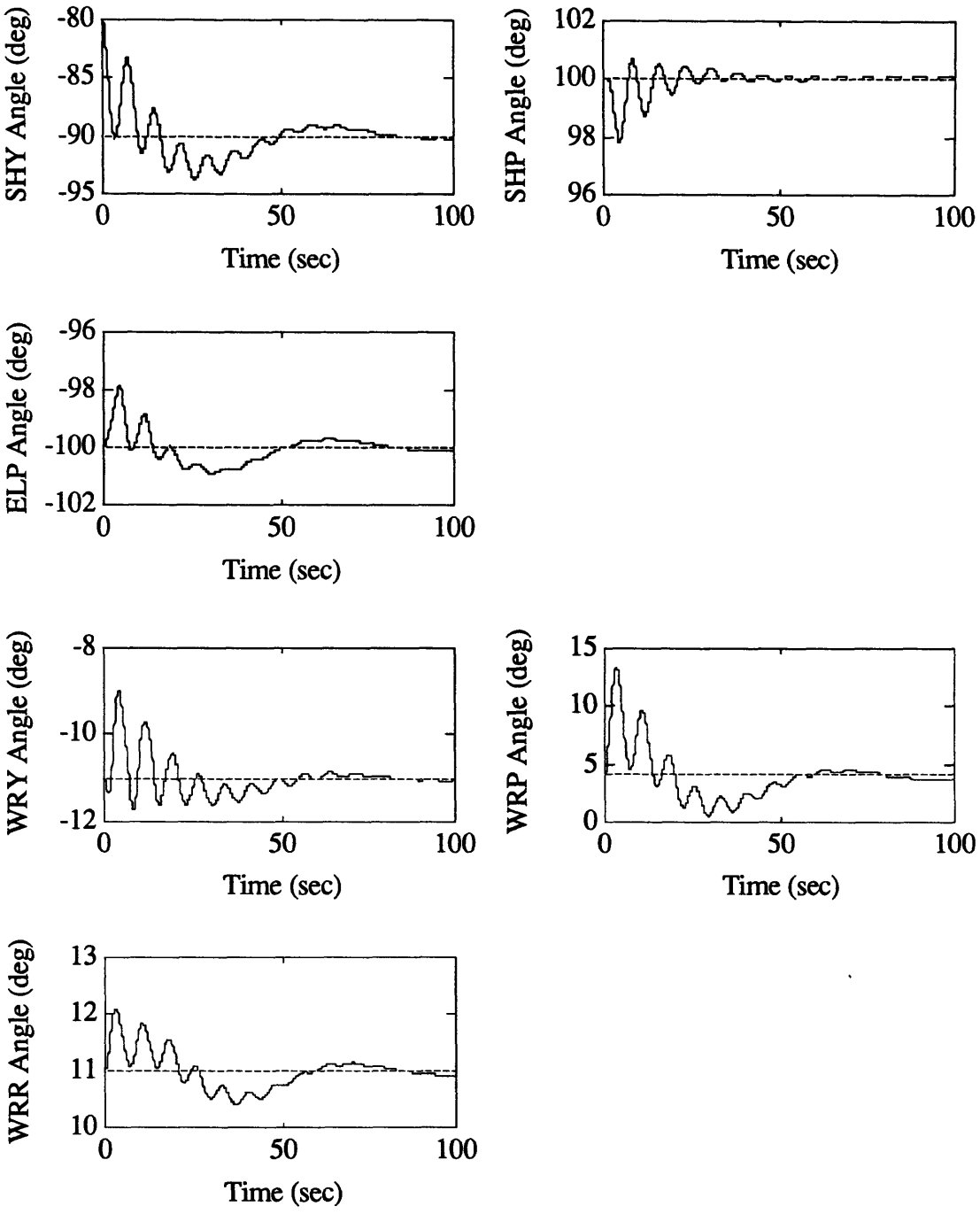

Figure 6.2. Joint Angle History for Constant Input Command

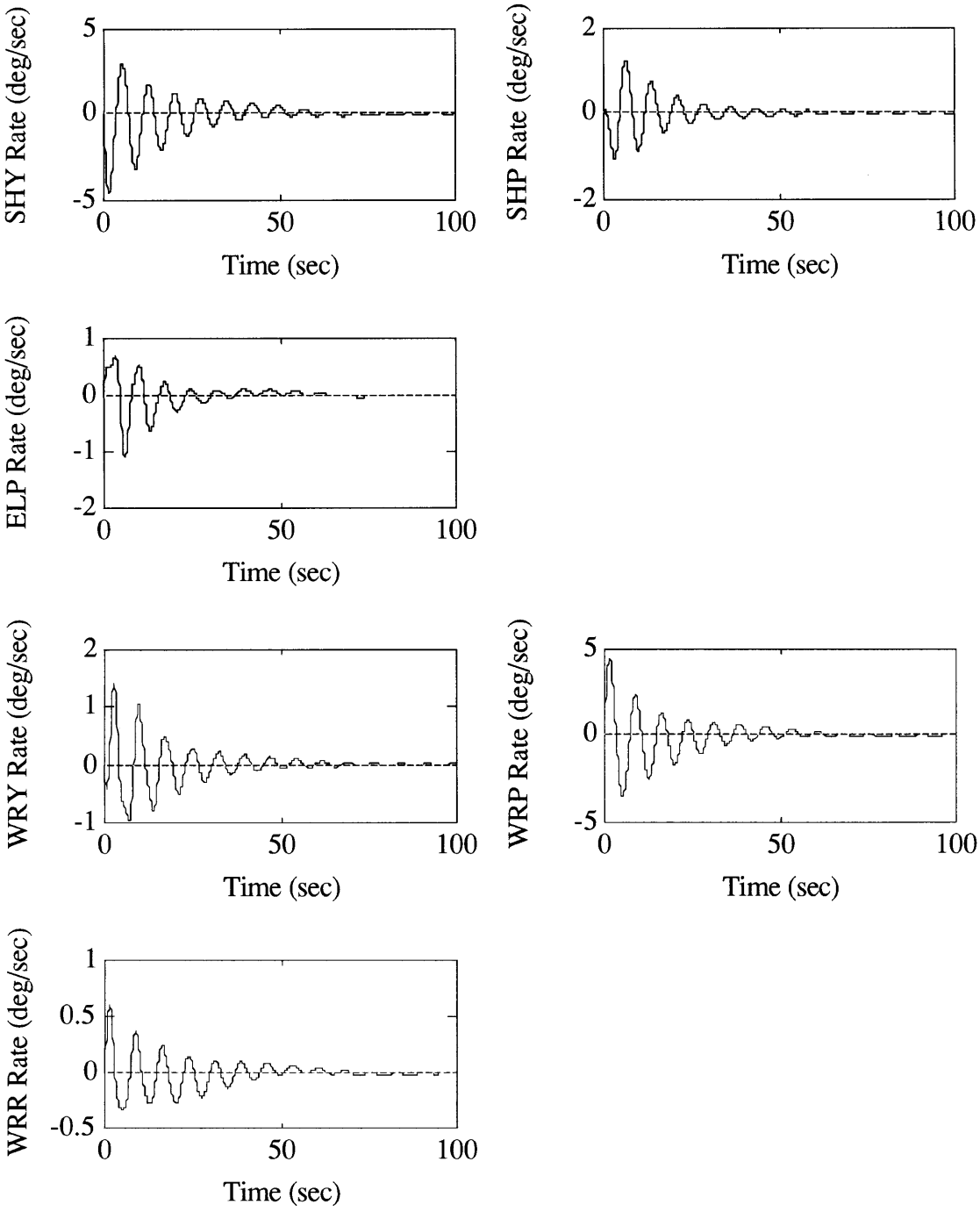

Figure 6.3. Joint Rate History for Constant Input Command

6.2 Feedback Linearization

Chapter 3 introduced the concept of feedback linearization and showed how the nonlinear feedback control law is derived. This section demonstrates how feedback linearization influences performance. The nonlinear feedback control law for the SRMS is made up of two parts, the joint acceleration due to the control and the joint acceleration due to the nonlinear feedback term. The relative contribution of each depends on joint rate, end effector position, payload mass and dimension properties. To facilitate the study, a cylindrically shaped payload was assumed held on the SRMS in its various positions. Figures 6.5 through 6.15 illustrate these relationships. Joint rates between 0.14 deg/s and 3 deg/sec were studied. Currently, the joint rate limits for Space Station size payloads are set at 0.14 deg/sec. At such slow rates, the feedback linearization "inner" control loop will have little influence on the system. However, at higher rates the feedback linearization "inner" control loop will have a significant impact on the system. The end effector positions that were studied are shown in Figure 6.4. Their locations are presented in Table 6.1.

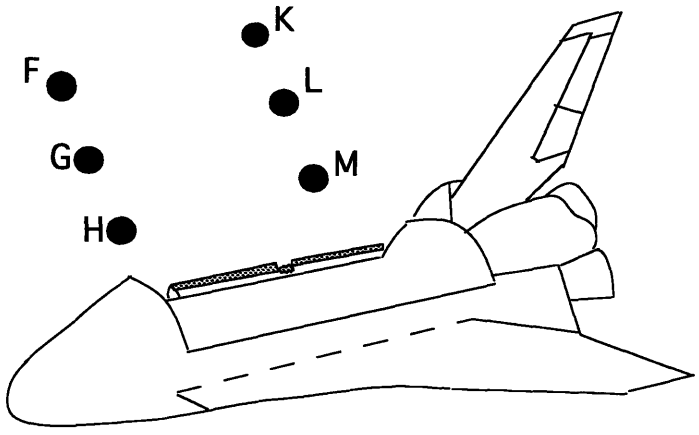

Figure 6.4. End Effector positions

Table 6.1. End Effector Position and Attitude

Position	X (in) Shoulder Yaw (deg)	Y (in) Shoulder Pitch (deg)	Z (in) Elbow Pitch (deg)	PITCH (deg) Wrist Pitch (deg)	YAW (deg) Wrist Yaw (deg)	ROLL (deg) Wrist Roll (deg)	Mass Size (MS)	Dim. changes (RS)
F1	379.5 -147.09	0.0 53.79	880.0 -7.88	0.0 78.97	270.0 52.32	0.0 46.74	1	1
F1	379.5 -147.09	0.0 53.79	880.0 -7.88	0.0 78.97	270.0 52.32	0.0 46.74	10	5
F1	379.5 -147.09	0.0 53.79	880.0 -7.88	0.0 78.97	270.0 52.32	0.0 46.74	10	1
F1	379.5 -147.09	0.0 53.79	880.0 -7.88	0.0 78.97	270.0 52.32	0.0 46.74	1	5
G1	379.5 -152.81	0.0 80.21	760.0 -72.23	0.0 -45.71	270.0 56.99	0.0 52.46	1	1
H5	379.5 -158.62	0.0 82.73	650.0 -96.35	0.0 -30.52	270.0 61.39	90.0 149.9	1	1
K1	979.5 -32.91	0.0 53.79	880.0 -7.88	0.0 -78.97	270.0 -52.32	0.0 -7.78	1	1
K1	979.5 -32.91	0.0 53.79	880.0 -7.88	0.0 -78.97	270.0 -52.32	0.0 -7.78	10	5
L1	979.0 -27.19	0.0 80.21	760.0 -72.23	0.0 -45.71	270.0 -56.99	0.0 -13.5	1	1
M5	979.0 -15.66	0.0 76.51	550.0 -109.56	0.0 -19.6	270.0 -65.2	90.0 59.54	1	1

Mass and dimension relations for the cylindrical payload were studied for end effector positions F1 and K1. For all configurations, as joint rate increased, the contribution from the nonlinear feedback joint acceleration increased dramatically, while the contribution of joint acceleration due from the control remained the same. The contribution of joint acceleration from the control term is only dependent on the error in joint angle. The steady state response to a 0.1 degree and 1.0 degree error are presented as '*' and '+', respectively. The transient response is one order of magnitude greater.

Figure 6.5 shows that, for position F1, with MS=1 (note MS=10 has 10 times the mass of MS=1) and RS=1, the joint acceleration due to the nonlinear feedback term becomes significant for joint rates greater than 0.5 deg/sec. The significance of the nonlinear feedback term varies by joint. Each of the six lines represent the response of one joint, and are labeled as such (SY=Shoulder Yaw, SP=Shoulder Pitch, EP=Elbow Pitch, WP=Wrist Pitch, WY=Wrist Yaw and WR=Wrist Roll). For Position F1 with MS=1 and RS=1, the elbow pitch, wrist pitch and shoulder pitch joint accelerations due to the feedback linearization terms are affected the most by increasing the rates. The shoulder yaw, wrist yaw, and wrist roll joints are relatively insensitive to the increasing rates for these arm geometries.

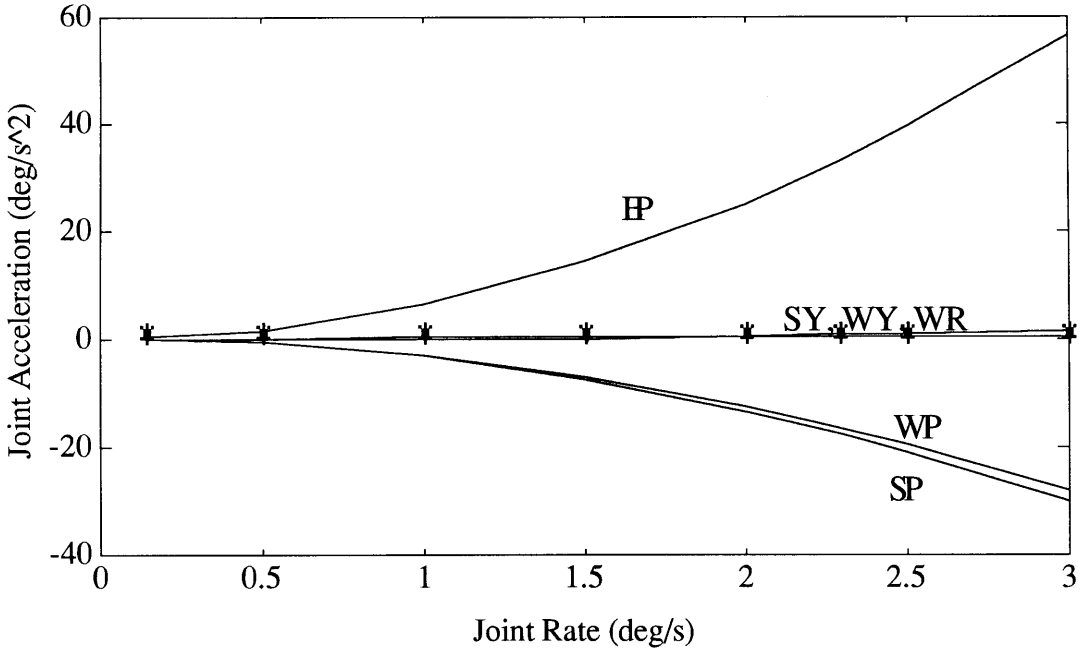

Figure 6.5. EE Position F1, MS=1, RS=1

For a ten times change in mass properties (MS) and five times change in cylinder dimension (RS), the joint acceleration nearly quadruples in each joint for position F1. In each joint, the magnitudes of the joint acceleration due to the feedback linearization term increase by about the same amount. Now, the shoulder yaw, wrist roll and wrist yaw joint accelerations due to the feedback linearization terms are affected slightly with increasing rates. The wrist pitch joint acceleration increased more than the shoulder pitch joint with increasing rates in this case.

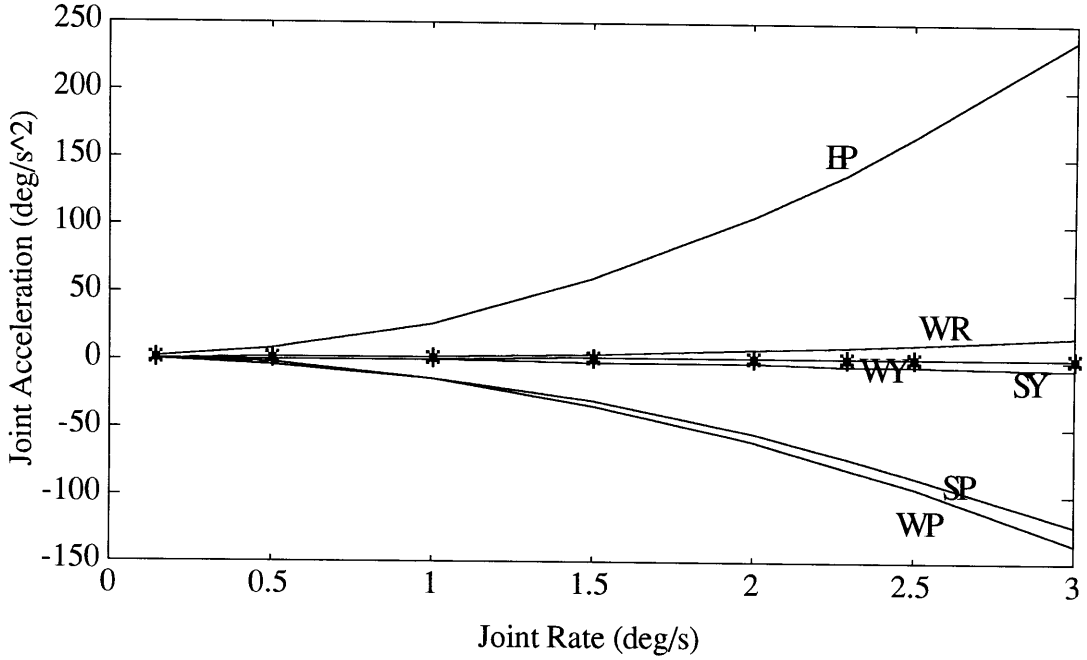

Figure 6.6. EE Position F1, MS=10, RS=5

Figures 6.7 and 6.8 will explain how the ten time change in mass properties and the five times change in dimension properties is broken down. According to Figure 6.7, changing only the mass properties (MS) by ten times and not changing the dimension properties (RS) does not significantly change the joint accelerations. The wrist roll, wrist yaw, and shoulder yaw joints are unaffected by the rate increase. As in Figure 6.5, the magnitude of the wrist pitch joint acceleration is less than that for the shoulder pitch joint at the different rates.

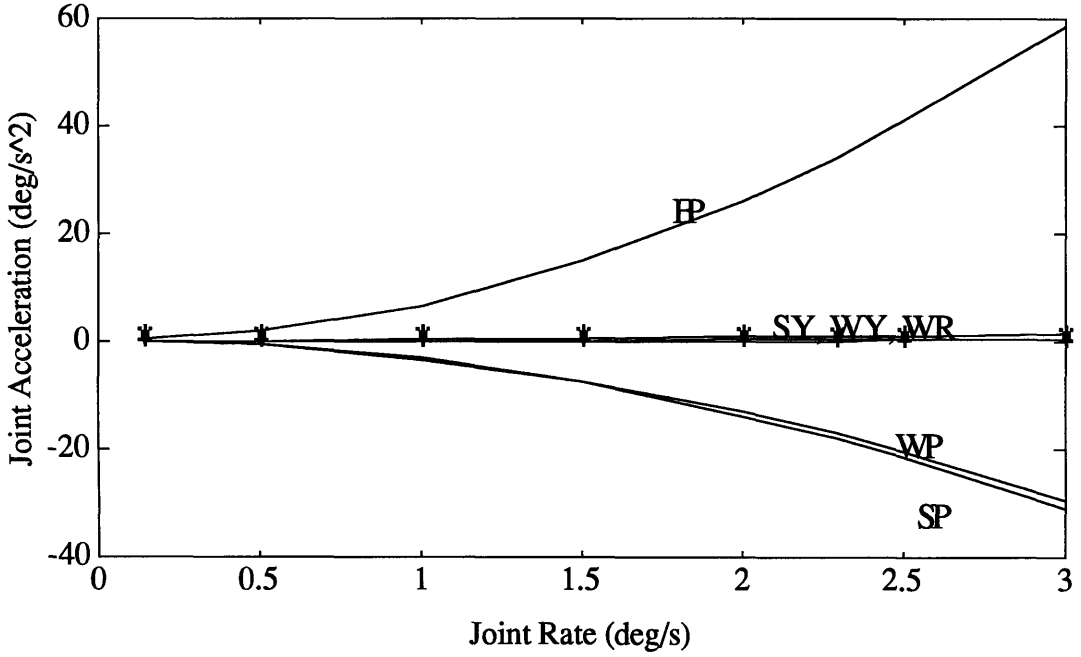

Figure 6.7. EE Position F1, MS=10, RS=1

Figure 6.8 illustrates that increasing the dimension properties for end effector position F1 by five times, without changing mass properties, has a severe impact on joint accelerations. The joint accelerations due to the feedback linearization terms in Figure 6.8 are about three times larger than the joint accelerations in Figure 6.5. Increasing the dimension properties simultaneously with mass properties increases the joint accelerations due to the feedback linearization terms even more. The joint accelerations shown in Figure 6.6 are slightly greater in magnitude than the joint accelerations shown in Figure 6.8. Increasing RS affects the wrist roll, wrist yaw, and shoulder yaw joints. As in Figure 6.6, their joint accelerations increase with increasing rate. Also the magnitude of the joint acceleration due to the feedback linearization terms in the wrist pitch joint is greater than that of the shoulder pitch joint.

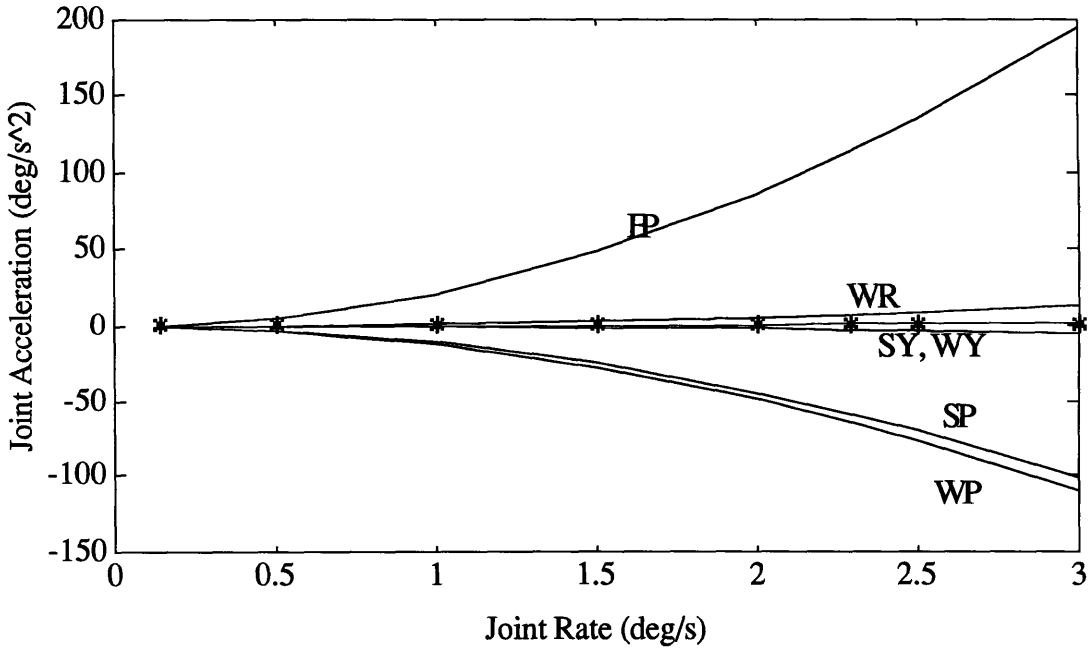

Figure 6.8. EE Position F1, MS=1, RS=5

Comparing Figures 6.5 and 6.9 shows that the joint accelerations due to the nonlinear feedback terms for position G1 are approximately fifteen times less than the joint accelerations for position F1. The nonlinear feedback terms do not dominate the control input until the joint rates are greater than 2.0 deg/sec. For position G, the wrist roll, wrist yaw, and shoulder yaw joint accelerations due to the feedback linearization terms increase slightly with increasing rate. Their magnitudes are about the same in position G as they are for position F. The magnitude of the joint accelerations in the elbow pitch, wrist pitch and shoulder pitch joints are significantly less for position G than for position F. As in position F with MS=1 and RS=1, the magnitude of the joint acceleration for the shoulder pitch joint is greater than that for the wrist pitch joint.

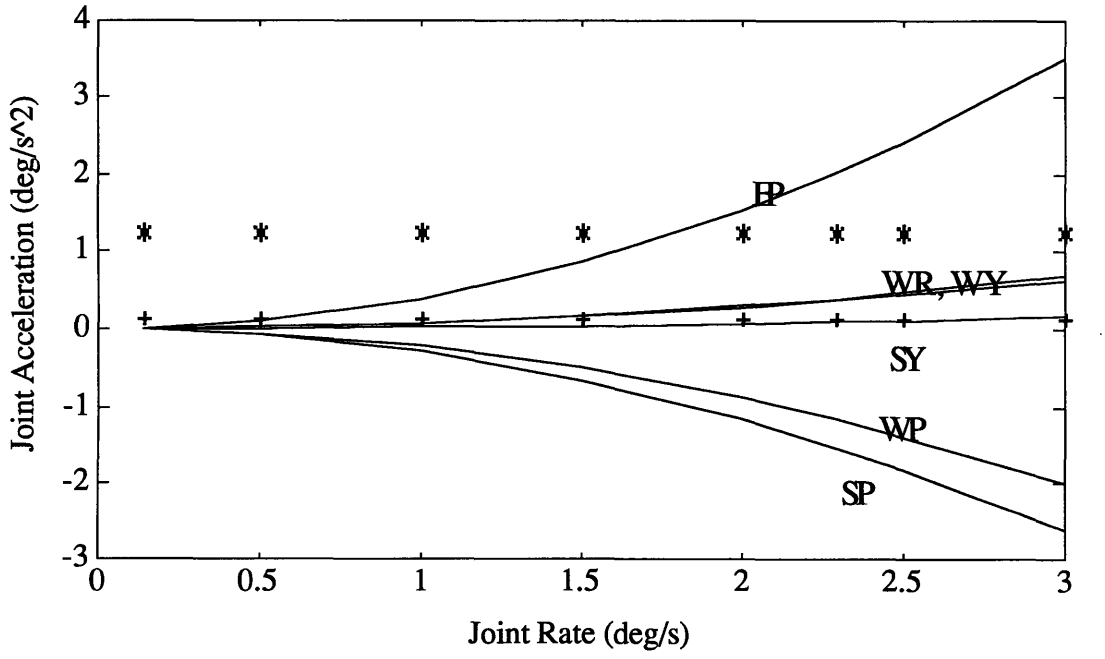

Figure 6.9. EE Position G1, MS=1, RS=1

Figure 6.10 illustrates that the joint accelerations due to the nonlinear feedback terms are similar for position H5 and G1, nearly fifteen times less than those for position F1. The joint accelerations due to the nonlinear feedback terms are slightly less at position H5 than position G1. The magnitudes of the joint accelerations for the elbow pitch, wrist pitch, and shoulder pitch joints are significantly less in position H than they are for position G. The magnitudes of the other joints are remain the same. Figure 6.4 shows that position F is the furthest from the shuttle in the Z direction, with respect to the end effector coordinate reference frame. Position H is closest to the shuttle, while position G is in-between F and H. All three positions have the same X and Y coordinates. This implies that the further away the end effector is from the shuttle, the more important the feedback linearization "inner loop" control law will be. Again, for positions G and H, it is not until the joint rates reach 2.0 deg/sec do the nonlinear feedback terms dominate the control input.

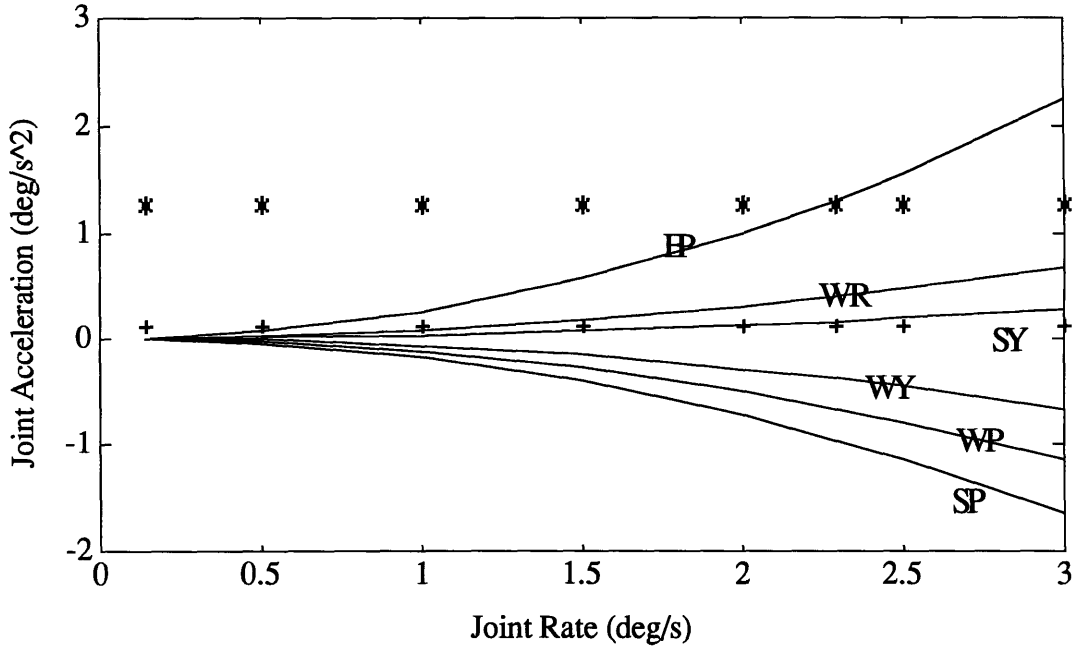

Figure 6.10. EE Position H5, MS=1, RS=1

Figure 6.4 and Table 6.1 show that position K has the same Z coordinate value as position F. Its X coordinate value is smaller than that of position F. For position K1, the joint accelerations due to the nonlinear feedback terms in the elbow pitch, wrist pitch, and shoulder pitch joints are almost half that for position F1. For joint rates greater than 0.7 deg/sec, the nonlinear feedback terms will be significant.

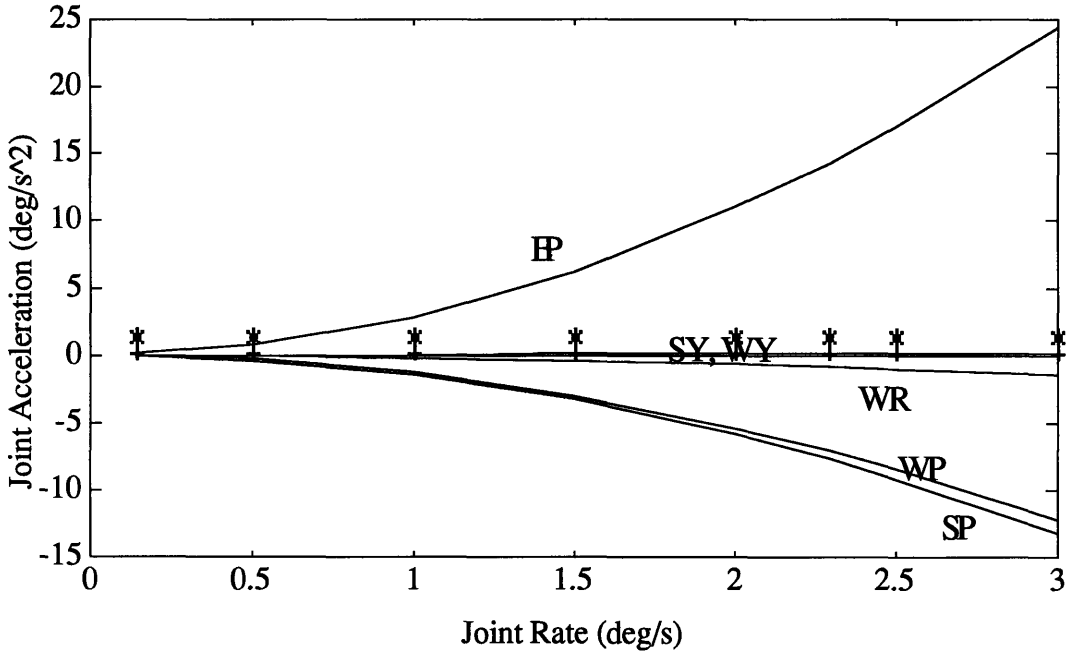

Figure 6.11. EE Position K1, MS=1, RS=1

For position K1, increasing the mass properties ten times and the dimension properties five times only increases the magnitudes of the joint acceleration due to the nonlinear feedback terms in all the joints by about 35 percent. Whereas, for position F, changing the mass and dimension properties by the same amounts changed the joint accelerations by over 400 percent. The joint accelerations in the elbow pitch, wrist pitch, and shoulder pitch joints also changed signs. Hence, the mass properties and dimension properties have different effects on different end effector positions.

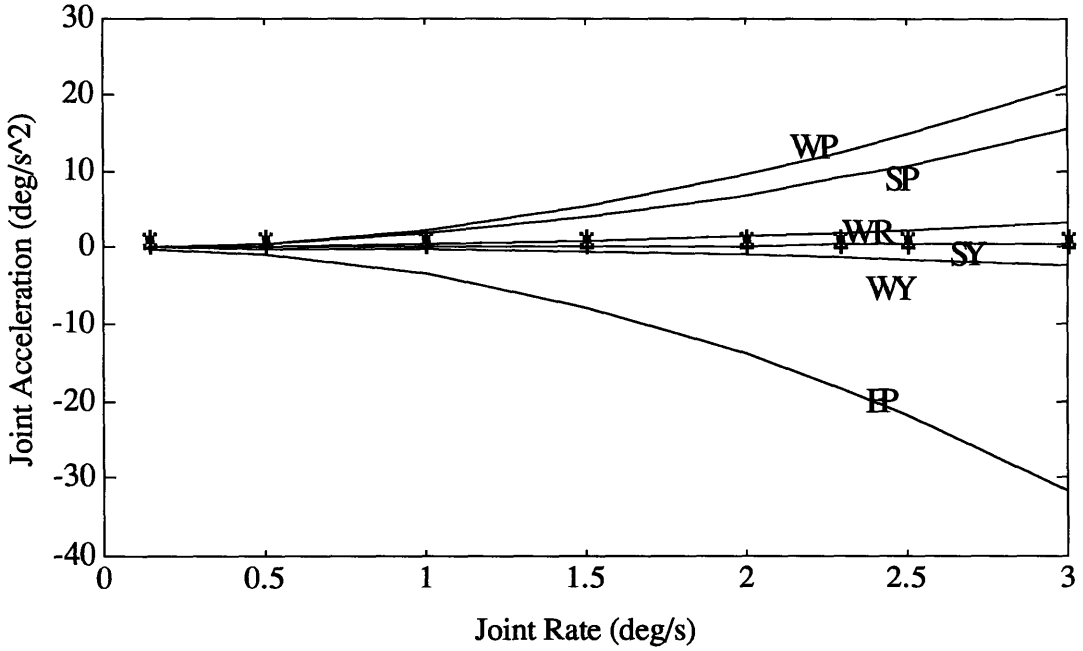

Figure 6.12. EE Position K1, MS=10, RS=5

The joint accelerations due to the nonlinear feedback terms for the elbow pitch, wrist pitch and shoulder pitch joints are not as significant at position L1 as they are for the position K which has the same X and Y coordinates. It is not until joint rates are greater than 2.5 deg/sec that the joint accelerations due to the nonlinear feedback terms become significant.

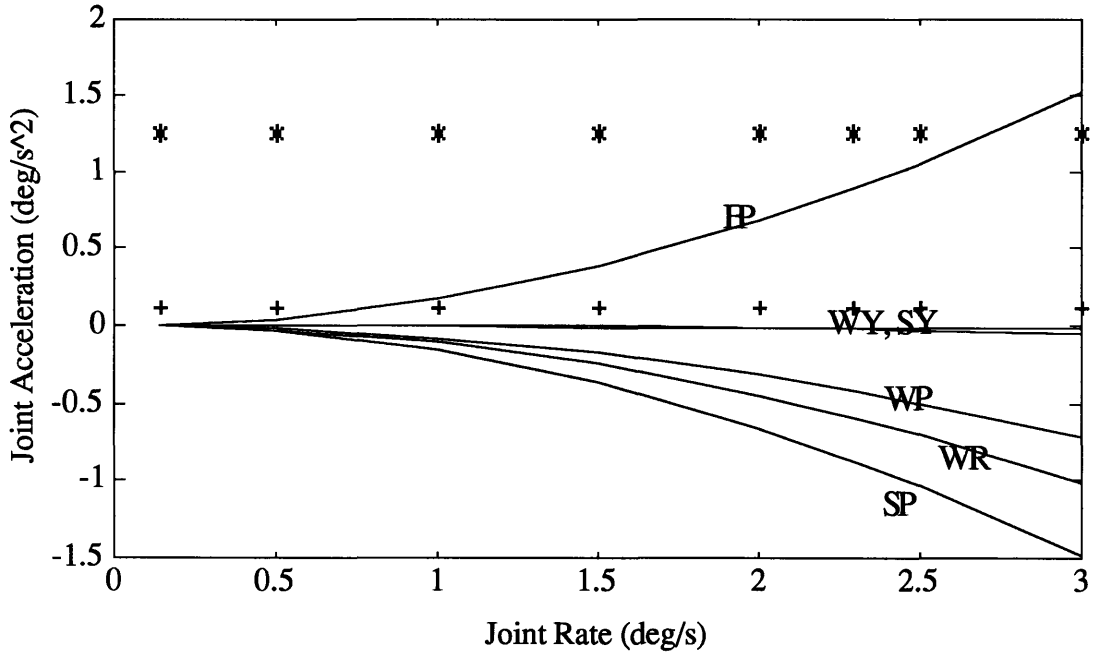

Figure 6.13. EE Position L1, MS=1, RS=1

EE position M5 yields even smaller joint accelerations for the nonlinear feedback terms in the elbow pitch, wrist pitch, and shoulder yaw joints than position L1. This is expected because position M is closer to the shuttle than position L. Both have the same X and Y coordinates. This result supports the conclusion that the closer the end effector is to the shuttle, the less significant are the joint accelerations due to the feedback linearization terms.

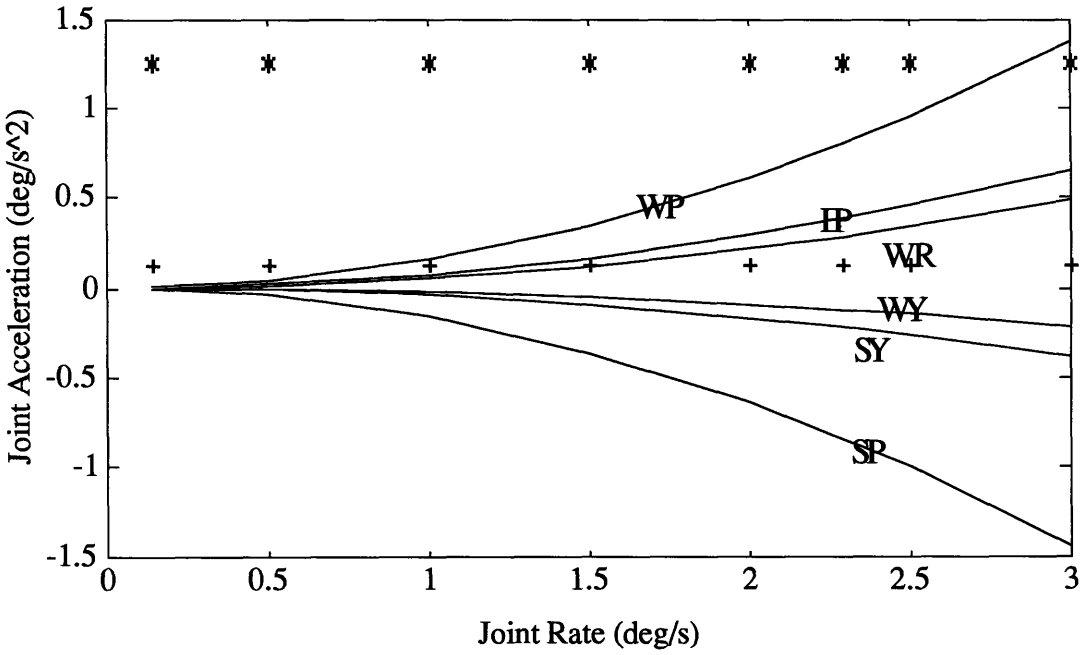

Figure 6.14. EE Position M5, MS=1, RS=1

From these plots, it is possible to summarize that the effect of the nonlinear feedback term is dependent not only on the joint rates, but also on the end effector position, mass properties, and dimensional properties. This implies that using feedback linearization will have a significant impact on the system performance for higher joint rates and maneuvers further from the shuttle. Currently, for space station size payloads, a joint rate of .14 deg/sec is chosen to be the rate limit. At this slow rate, feedback linearization

should have negligible effect on the performance of the system. Using feedback linearization, which takes into account the joint acceleration due to the nonlinear feedback term, should allow this joint rate to be increased. This, in turn, would reduce mission time required for SRMS maneuvers and ultimately allow astronauts to perform additional operations on-orbit.

6.3 Steering Algorithm

A realistic maneuver profile was created to be used with the design mode 1. Six points were chosen based on the current MB5 berthing trajectory for the Space Station Freedom. These points are described in Table 6.2. This trajectory was established to provide a direct, well lighted, and visible profile.

Table 6.2. MB5 Berthing Trajectory

POINT 1: SRMS at Capture Position						
View: MB5 - Capture						
RMS_JOINTS	-90.03 deg	97.99 deg	-60.02 deg	-57.45 deg	0.00 deg	19.50 deg
EE position	-674.4"	0.0"	-907.8"	269.8 deg	270.0 deg	269.8 deg
POINT 2: SRMS moves station further out and up over starboard wing						
View: MB5 - Station Positioned for final Attitude Adjustment						
RMS_JOINTS	-134.22 deg	69.77 deg	-46.72 deg	-70.05 deg	33.32 deg	50.20 deg
EE position	-429.6"	75.5"	-828.4"	269.3 deg	288.2 deg	269.4 deg
POINT 3: SRMS moves payload in Y over Starboard Wing						
View: MB5 - Station UBA Keel 5 Feet from the Orbiter Longeron						
RMS_JOINTS	-159.46 deg	87.00 deg	-58.00 deg	-94.28 deg	47.73 deg	77.82 deg
EE position	-429.4"	-91.3"	-811.2"	269.3 deg	288.2 deg	269.4 deg
POINT 4: SRMS moves payload in roll and Z to a 60 degree ELP						
View: MB5 - Station aligned in Position with some Roll						
RMS_JOINTS	-169.49 deg	89.07 deg	-59.93 deg	-105.48 deg	51.06 deg	92.36 deg
EE position	-429.4"	-135.8"	-795.4"	269.3 deg	288.2 deg	269.4 deg
POINT 5						
View: MB5 - Capture						
RMS_JOINTS	-149.21 deg	83.63 deg	-59.96 deg	-97.23 deg	25.07 deg	74.97 deg
EE position	--429.3"	-41.4"	-786.5"	269.7 deg	310.8 deg	269.8 deg

POINT 6: SRMS at Capture Position						
View: MB5 - Capture						
RMS_JOINTS	-156.15 deg	93.19 deg	-92.95 deg	-77.11 deg	26.78 deg	82.45 deg
EE position	-428.7"	-41.5"	-671.9"	269.7 deg	310.9 deg	269.8 deg

The steering algorithm for the design model was generated via a modified "Rigid Body Kinematic SRMS (KRMS)" code [16]. Rates for the different joints were computed using EE position and rate limit information. The rate limits used for translation (X,Y,Z) and rotation (pitch, yaw, roll) were 0.14 ft/s and 0.14 deg/s, respectively. It was possible to generate a joint angle trajectory using these six points and rate information. First, the maximum rates for maneuvers of each joint between the trajectory points were computed based on the given rate limits. Then, using the computed rate information and the joint angles for the trajectory points, it was possible to generate a joint angle history of the maneuver. The approach taken was based on Euler's theorem and use of appropriate quaternia.

Theorem 6.1 (Euler)*The most general displacement of a rigid body with one point fixed is equivalent to a single rotation about some axis through that point.* [17]

The rigid body motion described in Euler's theorem rotates about the eigen axis [17]. Rigid body motion can be separated into translational and rotational components. The translational components of motion can be specified by the motion of an arbitrary base point which is fixed in the body , while rotational motion can be specified by changes in orientation of the rigid body[17]. Translation and rotation rates are computed separately and superimposed. The translation rate vector is determined from the product of the

translation rate limit and the unit normal from the first end effector position to the second. The rotation rate vector is determined from the product of the rotation rate limit and the eigenaxis. In order to determine the eigenaxis, quaternia must be generated for the end effector positions.

Quaternions perform coordinate transformations on vectors. A quaternion is an ordered combination of scalar and (3D) vector elements which is capable of transforming 3D vectors according to prespecified rules. Quaternia are the mathematical representation of Euler's theorem. [18]

The notation for a quaternion of frame II with respect to frame I is

$$q_I^{II} \equiv \begin{bmatrix} s \\ \bar{v} \end{bmatrix} \equiv s + \bar{v} \tag{6.1}$$

where $\bar{v}$ is the vector which lies along the single equivalent axis of rotation, and s is a scalar which, along with $\bar{v}$, yields the angle of rotation about the eigenaxis, $\hat{v}$. $\hat{v}$ is a unit vector.

Quaternions are used to perform coordinate transformations on vectors. They obey the relationship

$$\bar{x}^{II} = q_I^{II} \bar{x}^I q_I^{II*} \tag{6.2}$$

where $\bar{x}^I$ is a quaternion whose scalar part is zero and is coordinatized in frame I, and $q_I^{II*} = (q_I^{II})^{-1}$. The form in which q_I^{II} performs coordinate transformations according to Eq. 6.2 is defined as

$$q_I^{II} \equiv \begin{bmatrix} \cos\left(\frac{\theta}{2}\right) \\ -\bar{u}\sin\left(\frac{\theta}{2}\right) \end{bmatrix} \tag{6.3}$$

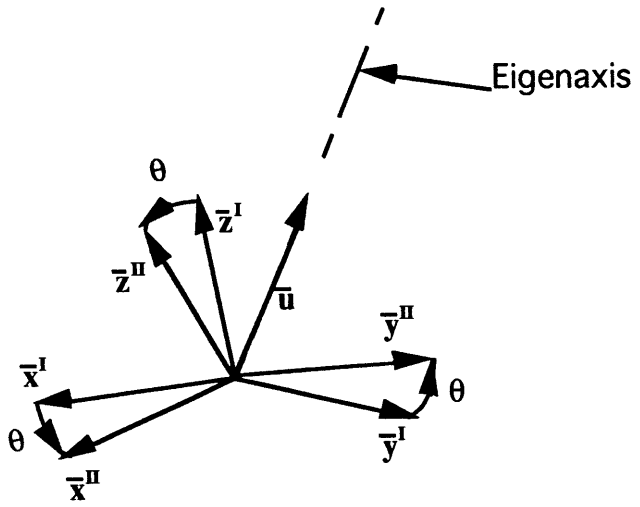

Figure 6.15. Coordinate Transformation with a Quaternion

The quaternia from ORAS to the first end effector position, q_{ORAS}^{EE1}, and from ORAS to the second end effector position, q_{ORAS}^{EE2}, are computed using *MATLAB* macros. Successive transformations can be grouped [18], this leads to

$$q_{EE1}^{EE2} = q_{ORAS}^{EE2} * q_{EE1}^{ORAS} \tag{6.4}$$

The eigenangle, θ, and eigenaxis, $\bar{u}$, can then be extracted from Eq 6.4.

$$\left.\begin{aligned} v &= \text{sign}(q_{EE1}^{EE2}) * q_{EE1}^{EE2}(2:4) \\ \theta &= 2 * \text{asin}(\|v\|) * \frac{180}{\pi} \\ \bar{u} &= -\frac{v}{\|v\|} \end{aligned}\right\}$$

(6.5)

The time for the maneuvers are determined by the rates and distance between end effector positions. The time for the translation and rotation part of the maneuvers are computed separately. The longer time is used as the time of maneuver. The time for the translation portion is computed by dividing the distance between the two points by the rate limit for the translation maneuver. The time for the rotation maneuver is determined by dividing the eigen angle by the rate limit for the rotation maneuver.

$$\mathbf{Time}_{\mathbf{translation}} = \frac{\|\text{Point 2} - \text{Point 1}\|}{\text{Rate Limit}_{\mathbf{translation}}}, \quad \mathbf{Time}_{\mathbf{rotation}} = \frac{\text{eigen angle}}{\text{Rate Limit}_{\mathbf{rotation}}}$$

(6.6)

The translational rate for the maneuver is computed by taking the product of the rate limit and the unit vector from Point 1 to Point 2. This rate is scaled if the time of the rotation part of the maneuver is greater than the time of the translational part. The rotational rate is determined by the product of the extracted eigen axis (Eq. 6.5) and the rate limit for rotation. Again, this is scaled if the time for the translational portion of the maneuver is longer than the time for the rotational portion.

Once the rates and time of maneuver are determined, the end effector positions and a joint angle history can be generated using the modified "Rigid Body Kinematic SRMS (KRMS)" code [16]. These end effector positions and joint angle trajectories, Figure 6.16 and 6.17, were then incorporated into the design model for evaluation. The "*" on the plots indicate the values of the joint trajectory specified in Table 6.2.

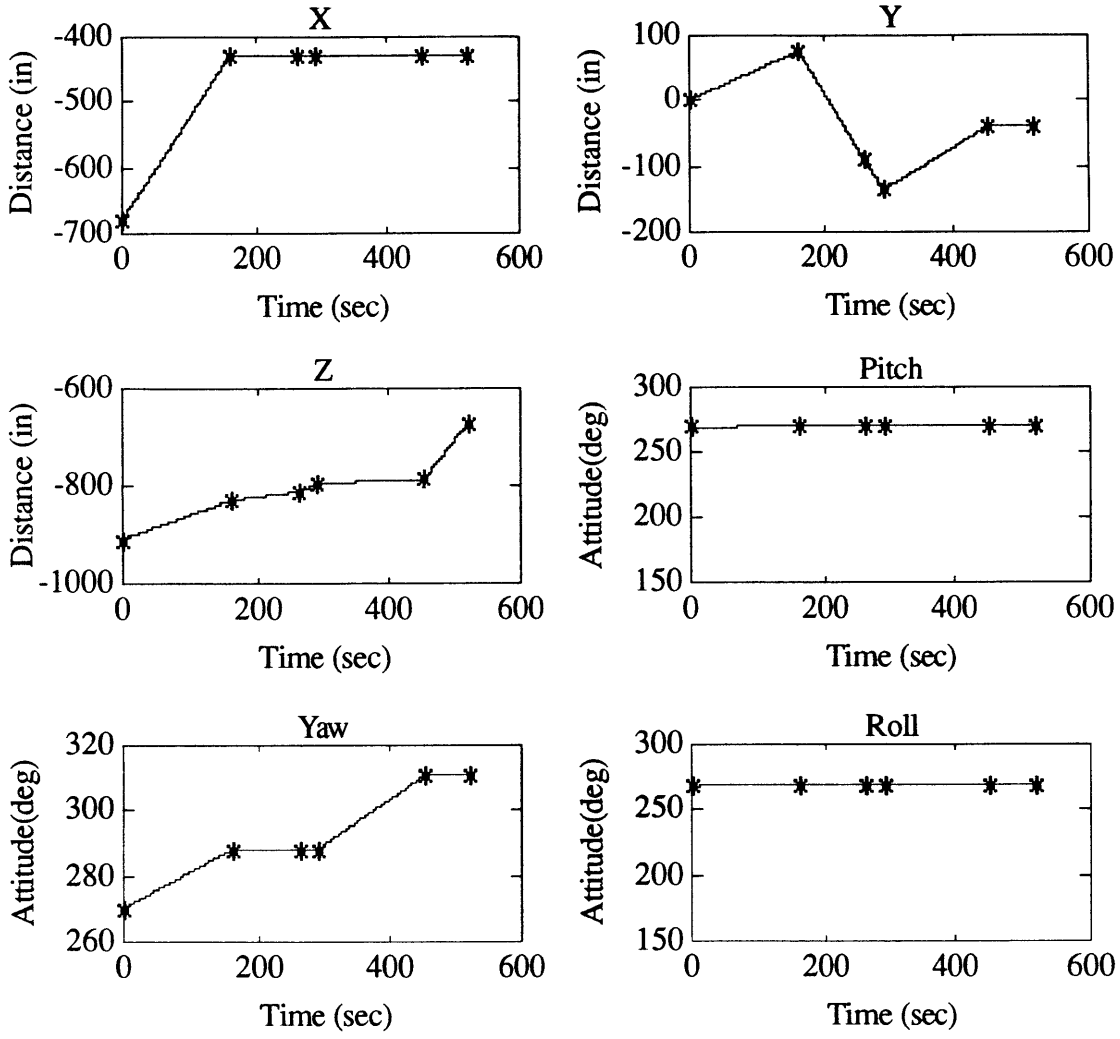

Figure 6.16 End Effector Positions

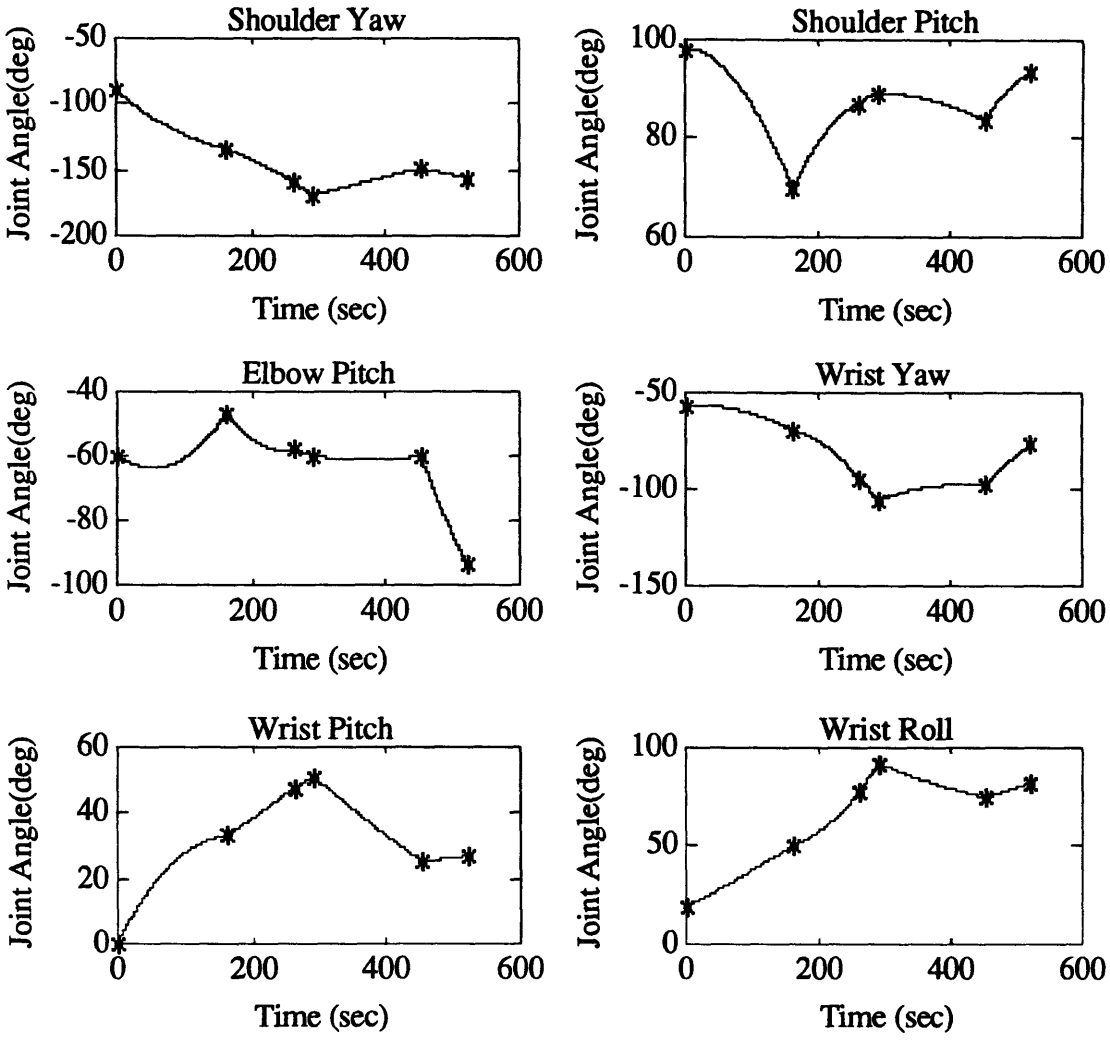

Figure 6.17. Joint Angle Trajectory

For point 1 of the maneuver, the joint angles do not yield a unique set of euler angles to describe the attitude of the end effector. With respect to ORAS, the set of euler angles generated by the steering algorithm, [180° 270° 180°] is equivalent to the desired set of euler angles [269.8° 270° 269.8°]. The "RateInv" code was modified to choose the [269.8° 270° 269.8°] set of euler angles. Figure 6.17 illustrates how the two sets of euler angles are equivalent. The order of rotation is Pitch Yaw Roll for the euler sequences. Frame A presents the direction of the coordinate frame. Frames B, C, and D present the [180° 270° 180°] sequence. Frame B represents a 180 rotation about the pitch axis from

Frame A; Frame C represents a 270° about the Yaw axis from the system in Frame B; and Frame D represents a 180° rotation about the Roll axis from Frame C. Frames E, F, and G present the corresponding euler sequence for [270° 270° 270°]. Notice that Frames D and G yield the same configuration. Hence, the euler sequences [180° 270° 180°] are equivalent to the euler sequence [270° 270° 270°].

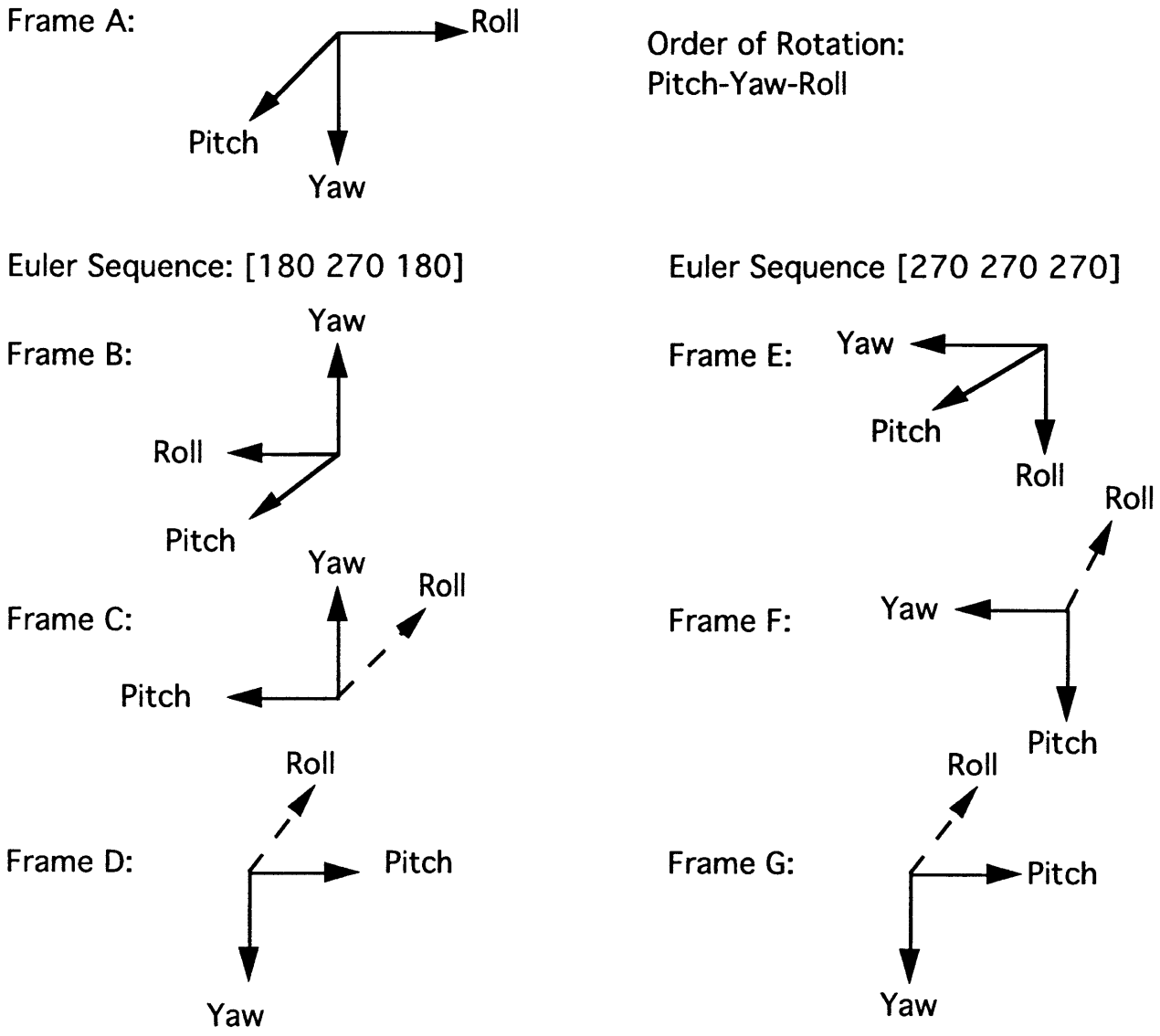

Figure 6.18. Euler Angles for Point 1

6.4 Implementation of Steering Algorithm

The joint angle trajectory of Section 6.3 was used to test the design model, including the current lead-lag controller, with and without feedback linearization. Because the joint rates were so slow (0.14 in/s & 0.14 deg/s) the results with and without feedback linearization were nearly identical. Recall, the results from section 6.3 showed that for all such slow rates, the joint acceleration due to the feedback linearization terms are insignificant as compared with the joint acceleration due to the control term. The results from studying the system at such slow rates using feedback linearization indicate that it is possible to implement feedback linearization in the system. For maneuvers at higher rates, the joint acceleration due to the feedback linearization terms will become significant as long as the $\Delta\gamma$ (difference between the commanded joint angle and the actual joint angle) remain relatively small. Figure 6.19 presents the resulting joint angles along with the prescribed trajectory. It is impossible to differentiate between the actual joint angle history and the commanded trajectory in Figure 6.19 because they are nearly identical.

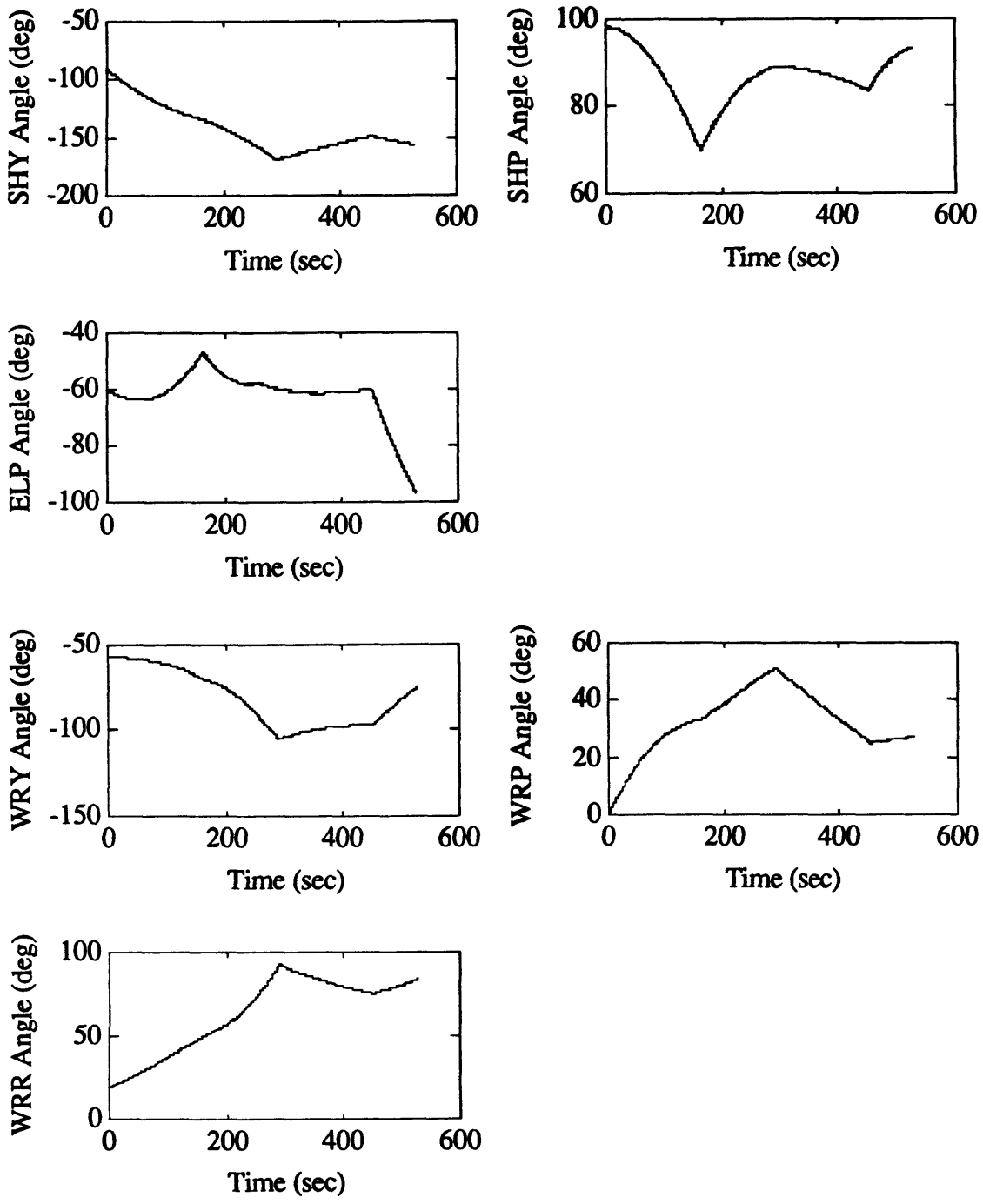

Figure 6.19. Joint Angle History with and without Feedback Linearization for Rate Limit of 0.14 in/sec and 0.14 deg/sec

Figure 6.20 presents the joint rates commanded during the maneuver from Point 1 to Point 6. As expected, the joint rates change direction and magnitude when the SRMS moves from one point to another. Also the magnitude of the joint rates are relatively small.

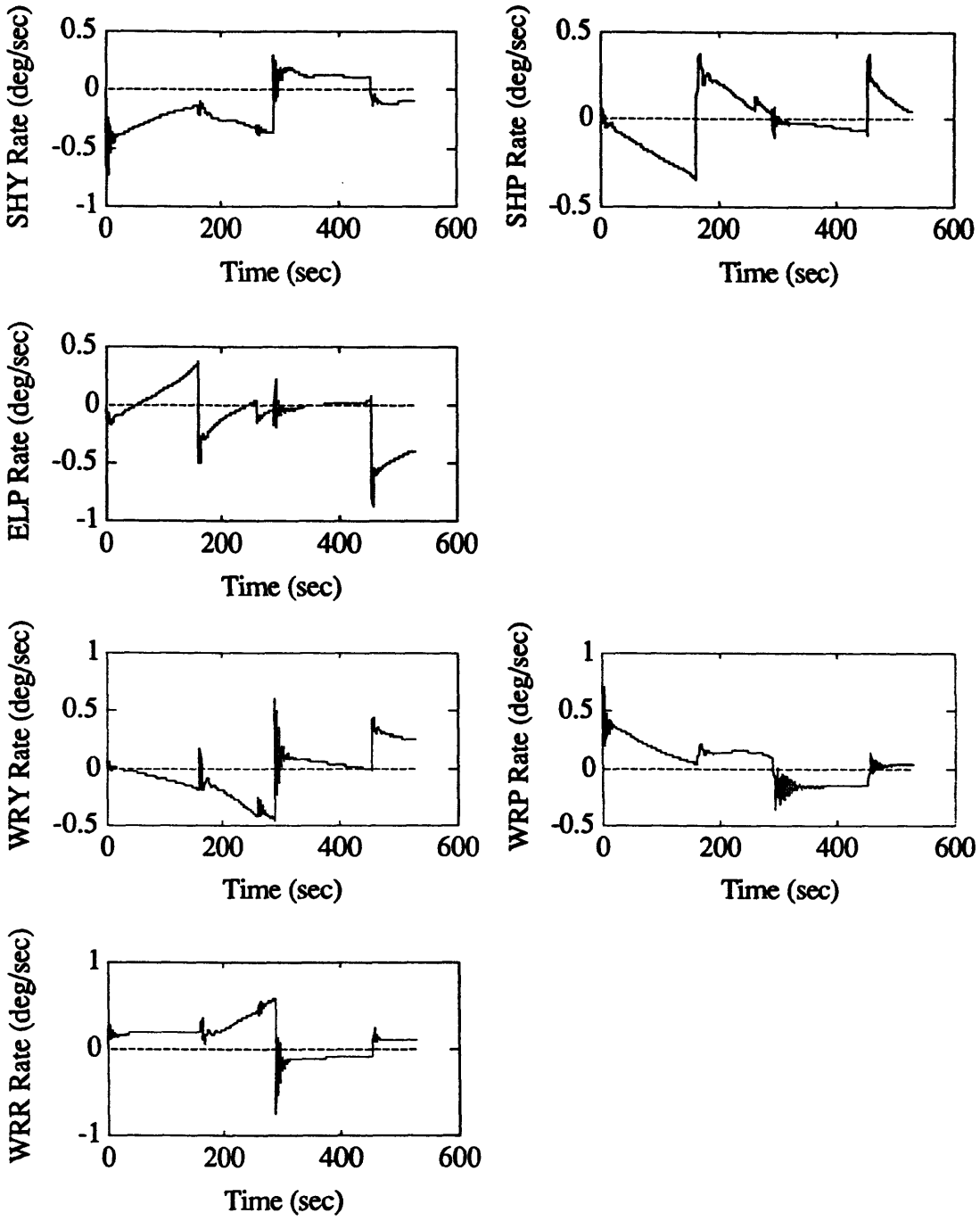

Figure 6.20. Joint Rate History with and without Feedback Linearization for 0.14 in/s and 0.14 deg/sec Rate Limits

Figure 6.21 presents the resulting $\Delta\gamma$ histories. The magnitudes of $\Delta\gamma$ are greatest when the trajectory changes from one point to another. Overall, the magnitudes of the $\Delta\gamma$ are small, hence the commanded trajectories are followed closely.

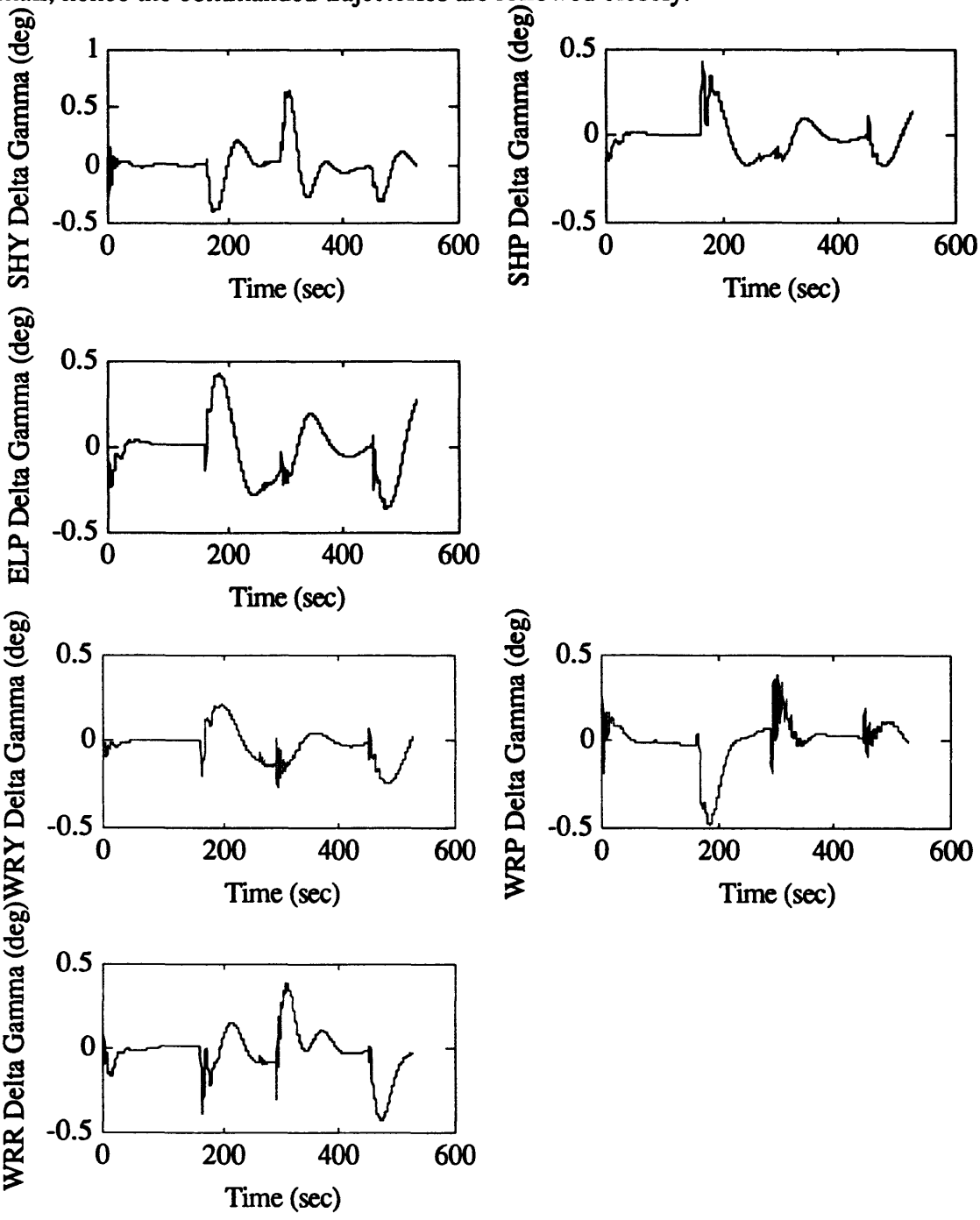

Figure 6.21. $\Delta\gamma$ History for 0.14 in/s and 0/14 deg/s Rate Limits

6.5 Nonlinear Gearbox Model

Section 4.1 discussed the linear and nonlinear models of the gearbox. A *SIMULINK* model of the nonlinear gearbox was generated and can be incorporated in the system model. The linear and nonlinear gearbox models were subjected to the same motor rate inputs from the servo model (obtained from a constant command input to the servo model). The resulting joint toques and gear torques were in the same direction, but of slightly different magnitudes. Figures 6.22 and 6.23 present the resulting linear and nonlinear gearbox joint torques, respectively, while Figures 6.24 and 6.25 present the resulting linear and nonlinear gearbox gear toques, respectively. Also, the frequency content of the signals with and without the nonlinear model also differ. Incorporating the nonlinear gearbox model will be more computationally intensive; however, it will yield more accurate results.

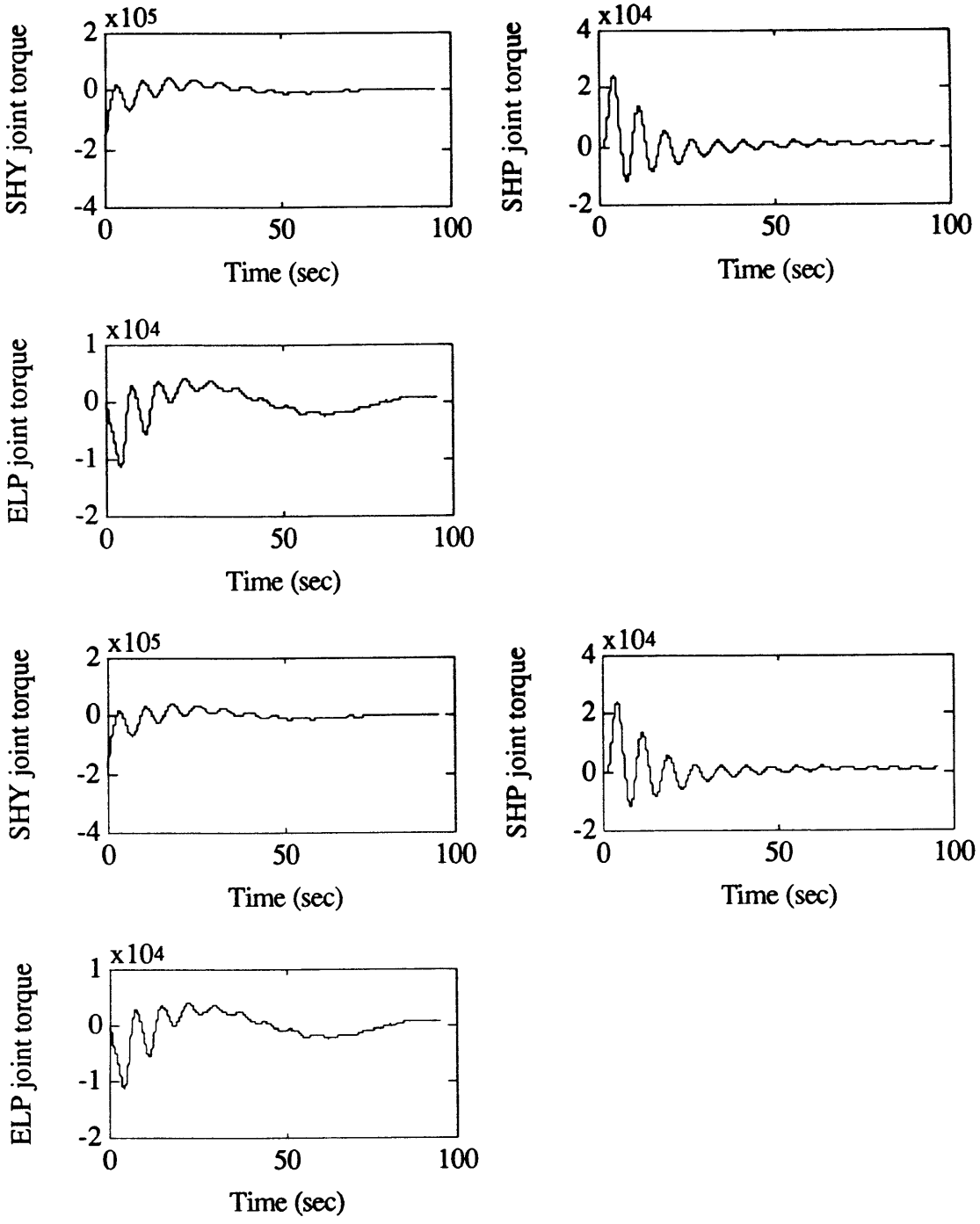

Figure 6.22. Linear Gearbox Joint Torques

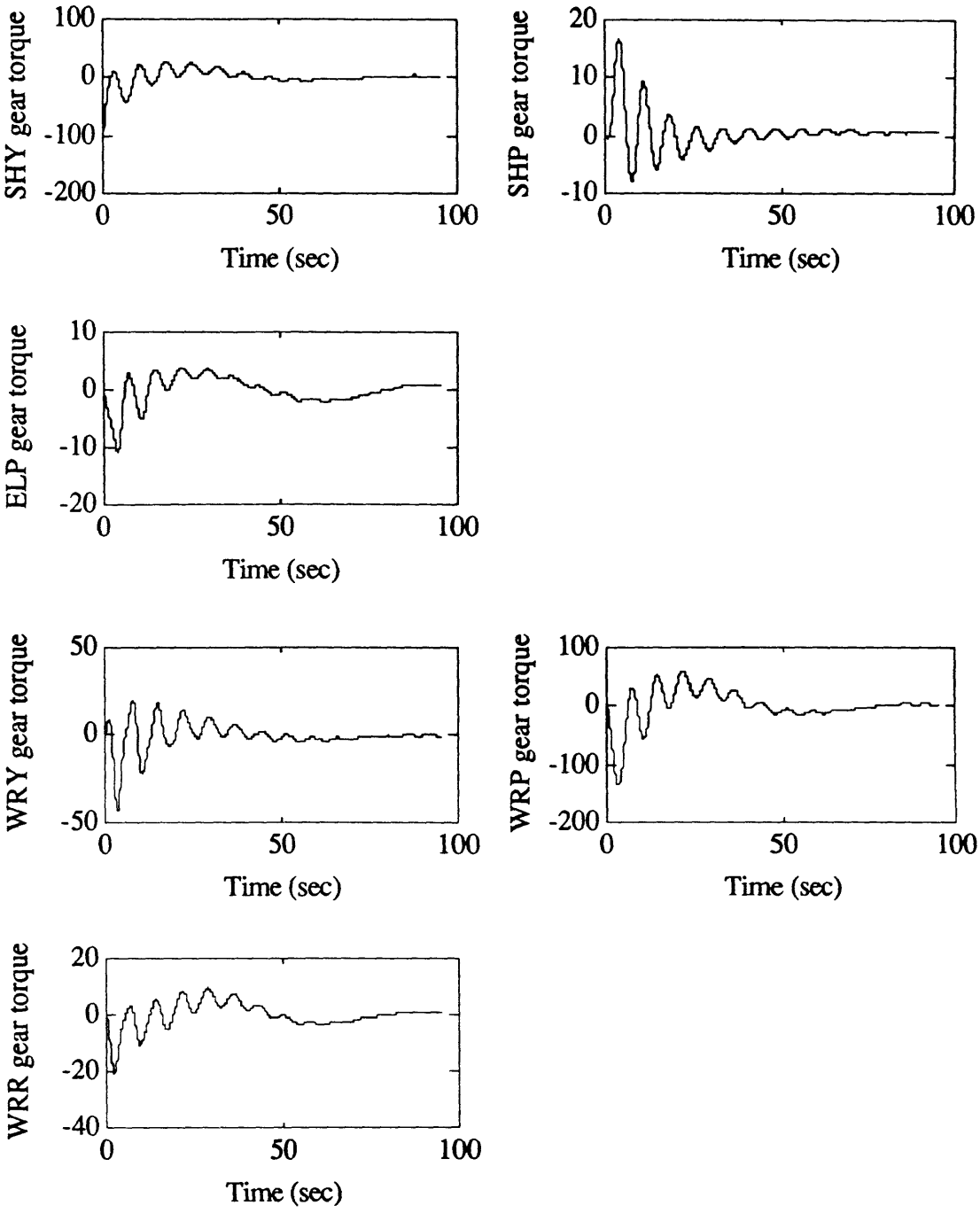

Figure 6.23. Linear Gearbox Gear Torques

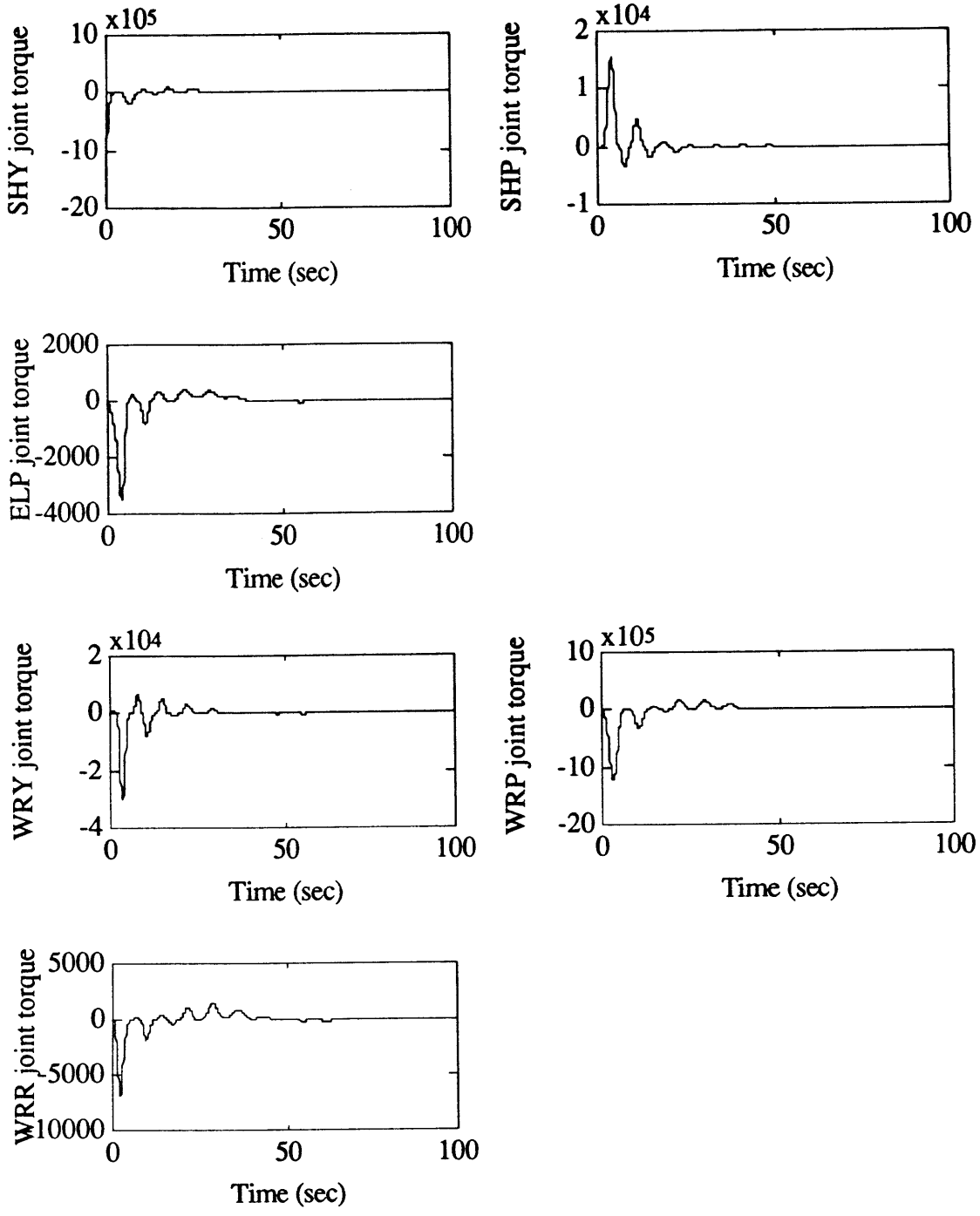

Figure 6.24. Nonlinear Gearbox Joint Torque

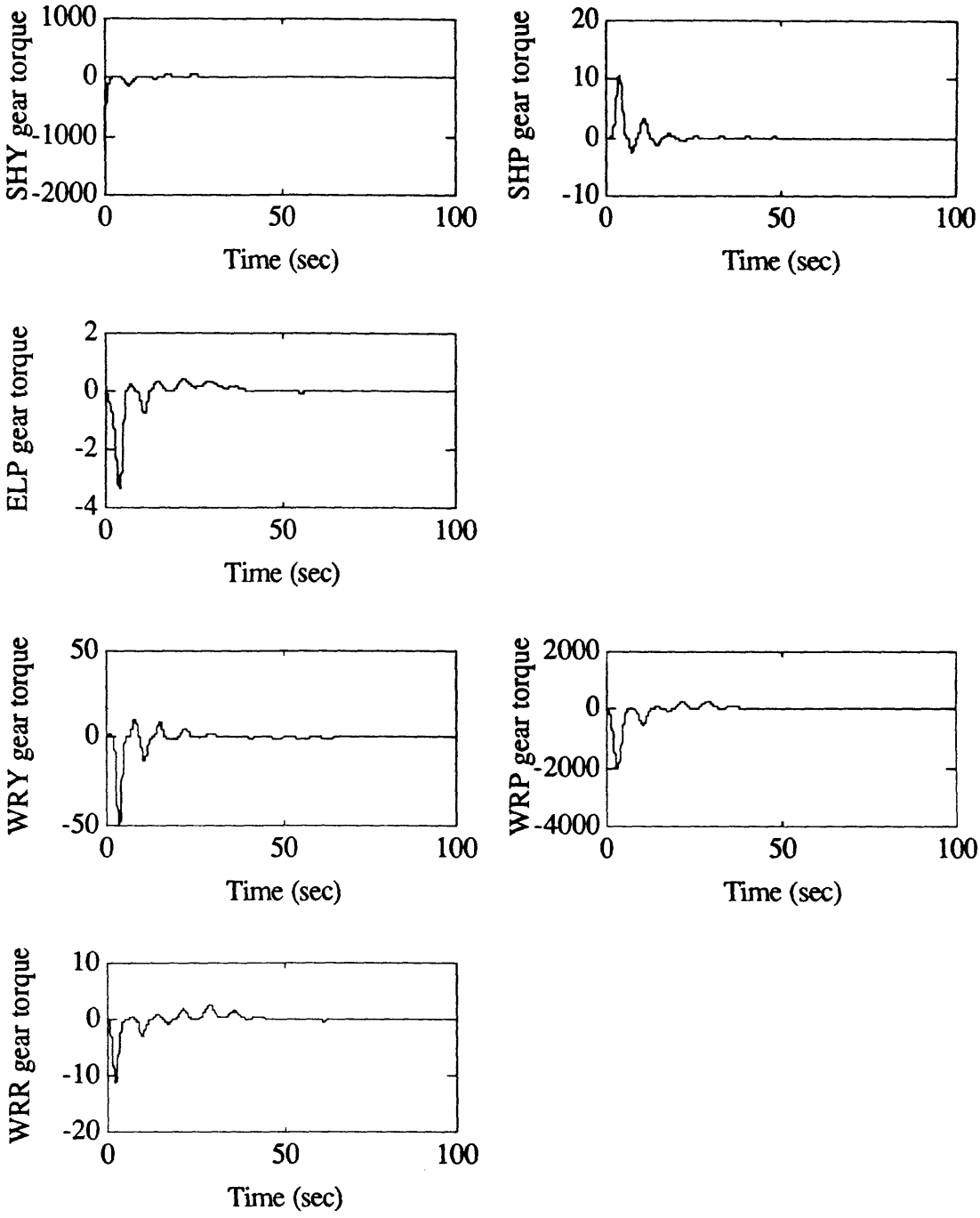

Figure 6.25. Nonlinear Gearbox Gear Torque

6.6 LQR Controller

In section 6.4 it was shown that it was possible to use the current linear lead-lag controller in the outer feedback loop plant to stabilize the system. This section will investigate the possibilities of replacing this lead-lag controller with a linear optimal controller, namely a Linear Quadratic Regulator (LQR) for the system without feedback linearization. A LQR controller will be designed for the *SIMULINK* 30^{th} order model that includes the reduced order servos.

Optimal Control theory is becoming increasingly important in designing modern control systems because its objective is to minimize the cost function. Optimal control theory helps to determine which control signals will cause a process to satisfy physical constraints while minimizing performance criteria [19]. R.E. Kalman provided the solution to the classical LQR problem in the 1960s. Since then, properties of the LQR problem have been well developed [20]. Kwakernaak and Sivan [21] explain the details of LQR theory. The solution to the LQR problem is known to be a constant gain matrix, hence, the LQR does not increase the order of the closed-loop system.

Using an LQR compensator, it is possible to stabilize SISO and MIMO nominal models. It also provides insight as to how the system will behave with model based compensators. However, it does have limitations, including requiring full state feedback, which is impractical in many applications.

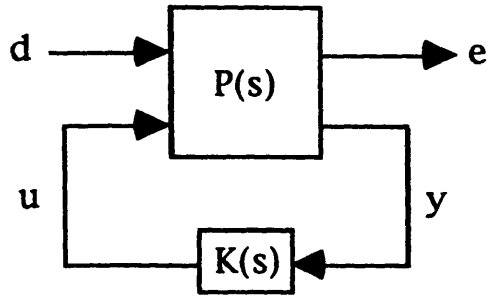

Figure 6.26. System with LQR Compensator

LQR requires uncorrupted full state feedback; hence, the disturbance vector only includes the process noise, and not the sensor noise. The general state space representation of the system in Figure 6.26 is

$$\begin{bmatrix} \dot{\mathbf{x}}_p \\ \mathbf{e} \\ \mathbf{y} \end{bmatrix} = \begin{bmatrix} \mathbf{A} & \mathbf{B}_1 & \mathbf{B}_2 \\ \mathbf{C}_1 & \mathbf{D}_{11} & \mathbf{D}_{12} \\ \mathbf{C}_2 & \mathbf{D}_{21} & \mathbf{D}_{22} \end{bmatrix} \begin{bmatrix} \mathbf{x}_p \\ \mathbf{d} \\ \mathbf{u} \end{bmatrix} \tag{6.7}$$

where $\mathbf{x}_p$ is the state vector, $\mathbf{e}$ is the error vector that includes the states and the controls $\mathbf{e} = \begin{bmatrix} \mathbf{x}_p \\ \mathbf{u} \end{bmatrix}$, $\mathbf{d}$ is the disturbance vector, $\mathbf{y}$ is the output vector that is fed to the compensator and $\mathbf{u}$ is the control input from the compensator to the plant. Because LQR requires full state feedback, the $\mathbf{C}_2$ matrix is always the identity matrix, $\mathbf{I}$.

The LQR method derives a feedback control law that minimizes the following quadratic cost function. The cost function, presented in Eq. 6.8 is subject to the constraints of the differential equations of the state variables.

$$\mathbf{J} = \int_0^\infty \left[\mathbf{x}_p^T \mathbf{Q} \mathbf{x}_p + \mathbf{u}^T \mathbf{R} \mathbf{u} \right] dt \tag{6.8}$$

where **Q** is a positive semi-definite symmetrical matrix that weights the states. $\mathbf{Q} = \mathbf{N}^T\mathbf{N}$, and [**A**,**N**] must be detectable. **R** is the positive definite symmetrical matrix that weights the controls. The optimal feedback control law that is produced by the LQR method is

$$\begin{aligned} \mathbf{u} &= -\mathbf{K}\mathbf{x}_p \\ \mathbf{K} &= \mathbf{R}^{-1}\mathbf{B}_p^T\mathbf{P} \end{aligned} \tag{6.9}$$

where **P** is the positive semi-definite solution of the "control" algebraic Riccati equation. In general there are many solutions of the "control" algebraic Riccati equation, however, only one is positive semi-definite. If [**A**,**B**] is controllable and if [**A**,**N**] is observable, then **P** is positive definite.

$$\mathbf{0} = -\mathbf{P}\mathbf{A} - \mathbf{A}^T\mathbf{P} - \mathbf{Q} + \mathbf{P}\mathbf{B}\mathbf{R}^{-1}\mathbf{B}^T\mathbf{P} \tag{6.10}$$

The closed-loop dynamics of the system become

$$\begin{aligned} \dot{\mathbf{x}}_p &= \mathbf{A}\mathbf{x}_p + \mathbf{B}_2\mathbf{u} + \mathbf{B}_1\mathbf{d} \\ \mathbf{u} &= -\mathbf{K}\mathbf{x}_p \\ \dot{\mathbf{x}}_p &= [\mathbf{A} - \mathbf{B}_2\mathbf{K}]\mathbf{x}_p + \mathbf{B}_1\mathbf{d} \end{aligned} \tag{6.11}$$

And, the poles of the closed loop system are guaranteed to be stable, i.e. in the left half plane.

$$\mathrm{Re}\lambda_i[\mathbf{A} - \mathbf{B}_2\mathbf{K}] < 0, \quad \forall i \tag{6.12}$$

Stability of the nominal closed-loop system is assured regardless of the numerical values of **A**,**B**,**Q**, and **R**. The exact locations of the closed-loop poles will, however, depend on the numerical values of the given **A** and **B**, and chosen **Q** and **R** matrices.

The weighting matrices Q and R were chosen based on Bryson's rule. The states that are important, and weighted heavily are the joint angle and joint rate states. All controls were weighted equally. It was desired that the magnitude of the change in joint angle be less than one degree, or less than 0.017 rad. It was assumed that this is equivalent to a 0.1 deg/sec change and rate and 0.1 deg/sec change in the control. Using Bryson's rule [22], the corresponding Q, and R matrices were chosen to be

$$Q = \begin{bmatrix} \varepsilon & 0 & 0 & 0 & 0 & 0 & 0 & 0 & 0 \\ 0 & \ddots & 0 & 0 & 0 & 0 & 0 & 0 & 0 \\ 0 & 0 & \varepsilon & 0 & 0 & 0 & 0 & 0 & 0 \\ 0 & 0 & 0 & \frac{1}{0.017^2} & 0 & 0 & 0 & 0 & 0 \\ 0 & 0 & 0 & 0 & \ddots & 0 & 0 & 0 & 0 \\ 0 & 0 & 0 & 0 & 0 & \frac{1}{0.017^2} & 0 & 0 & 0 \\ 0 & 0 & 0 & 0 & 0 & 0 & \frac{1}{0.0017^2} & 0 & 0 \\ 0 & 0 & 0 & 0 & 0 & 0 & 0 & \ddots & 0 \\ 0 & 0 & 0 & 0 & 0 & 0 & 0 & 0 & \frac{1}{0.0017^2} \end{bmatrix}$$

$$R = \begin{bmatrix} 100000 & 0 & 0 & 0 & 0 & 0 \\ 0 & 100000 & 0 & 0 & 0 & 0 \\ 0 & 0 & 100000 & 0 & 0 & 0 \\ 0 & 0 & 0 & 100000 & 0 & 0 \\ 0 & 0 & 0 & 0 & 100000 & 0 \\ 0 & 0 & 0 & 0 & 0 & 100000 \end{bmatrix}$$

The state space for the system was obtained from a *SIMULINK* model[1]. The system model contained a linear representation of the servos, gearbox, and nonlinear arm dynamics model. Figure 6.27 presents a block diagram of the *SIMULINK* model that

[1]Note, when converting the *SIMULINK* block diagram representation of the system into a state space representation, the states maybe rearranged by *SIMULINK*.

was used to generate the LQR controller. The nonlinear arm dynamics model was linearized about Point 1 in the trajectory. The joint acceleration was approximated as the product of the composite inertia matrix at Point 1 and the control input. The other terms from Eq. 4.3 are higher order terms that are not significant in the approximation. *MATLAB* tools were used to solve the "control" algebraic Riccati equation and derive the required gain matrix.

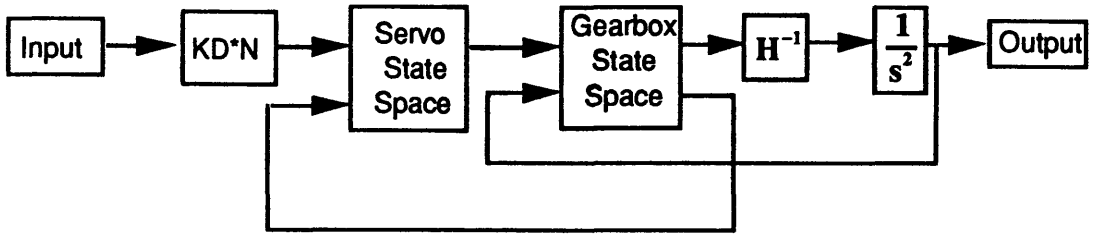

Figure 6.27 *SIMULINK* Model Used to Generate LQR Gain Matrix

The LQR compensator was integrated with the *SIMULINK* model of the system. The states associated with $\Delta\gamma$ and $\Delta\dot{\gamma}$ were weighted most through Q. A block diagram of the system is presented in Figure 6.28. The steering command input is the same as the one used for the current lead-lag controller model.

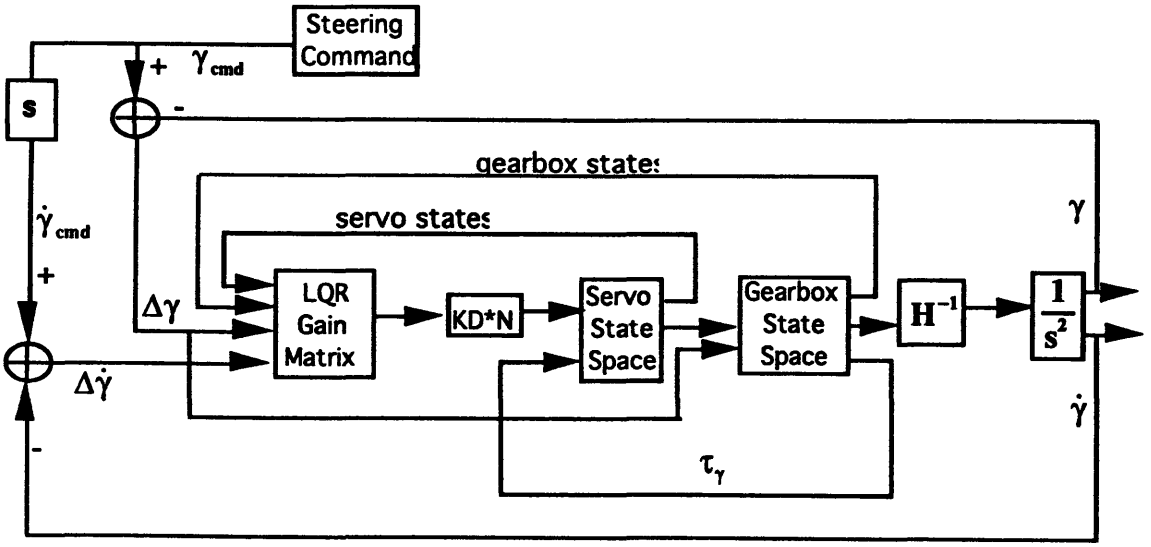

Figure 6.32 *SIMULINK* Model of LQR Controller Integrated with System

The LQR controller was designed based on linearizing the nonlinear arm dynamics about Point 1 of the trajectory. As the SRMS moves away from this point, LQR does not guarantee system stability. This effect is seen in Figures 6.29 through 6.31. As the SRMS approaches Point 2 of the trajectory after 150 seconds of motion, the controller can no longer stabilizes the system.

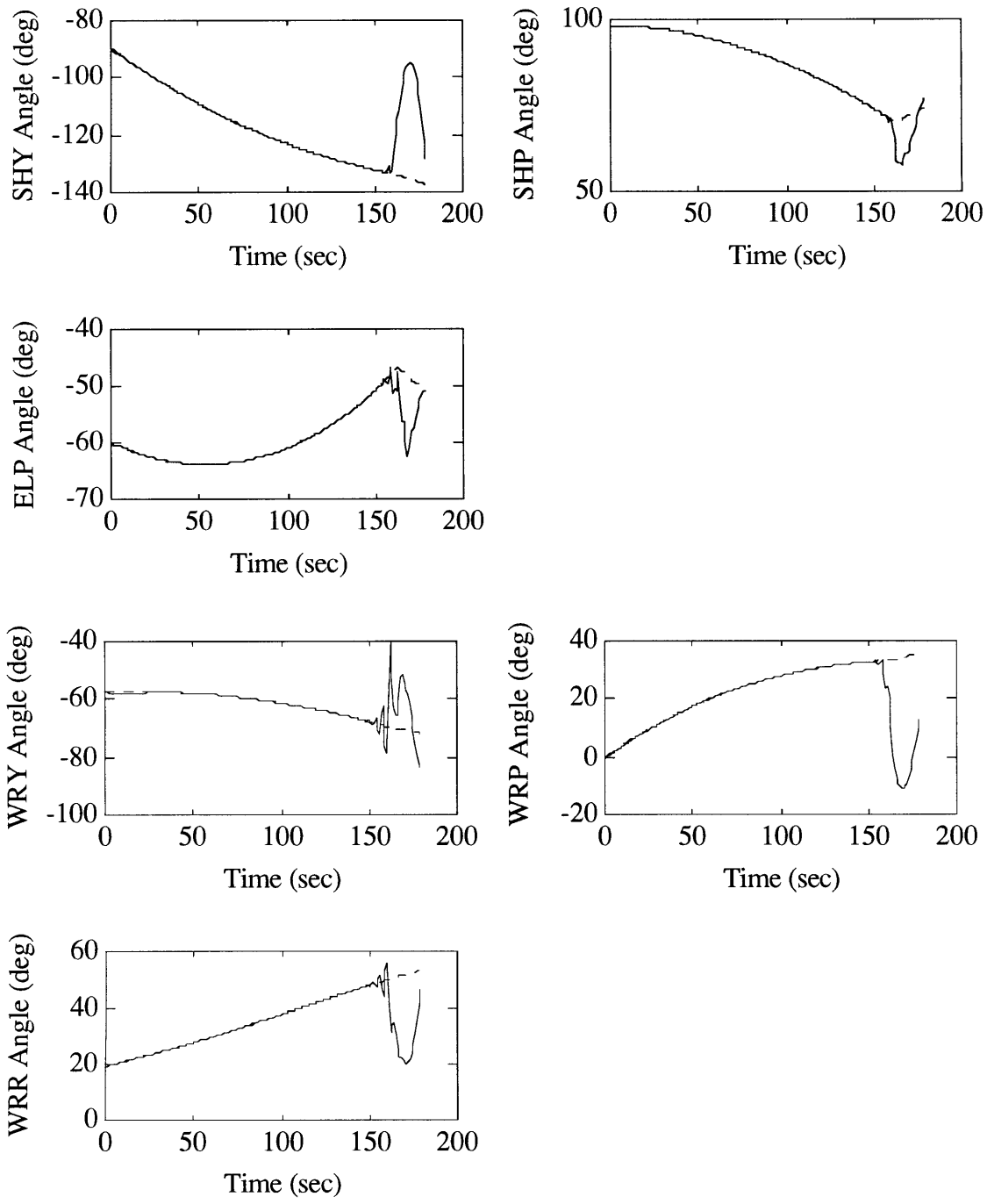

Figure 6.29. Joint Angle History for LQR Compensator without Feedback Linearization and Rate Limits of 0.14 deg/sec and 0.14 in/sec

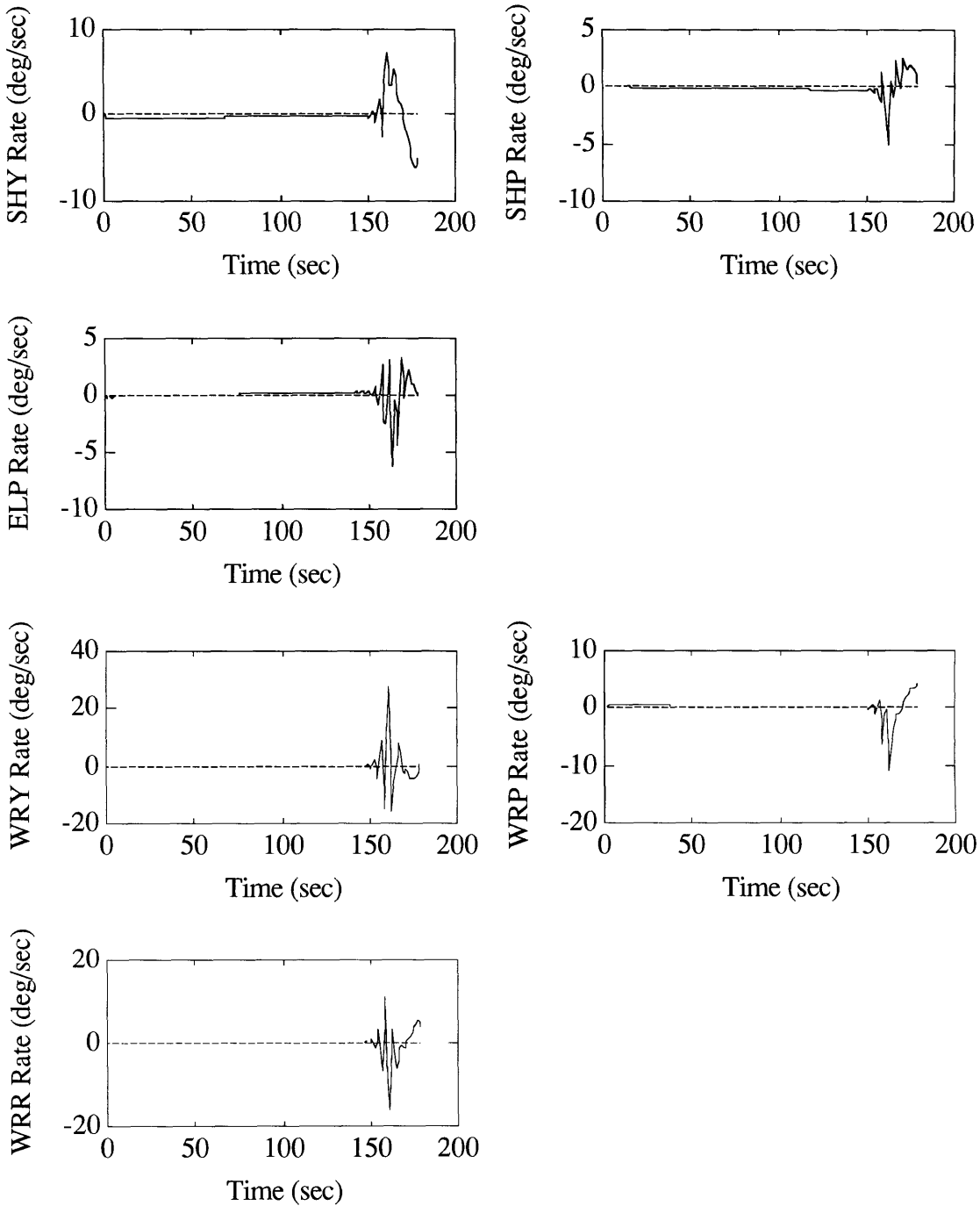

Figure 6.30 Joint Rate History for LQR Compensator without Feedback Linearization

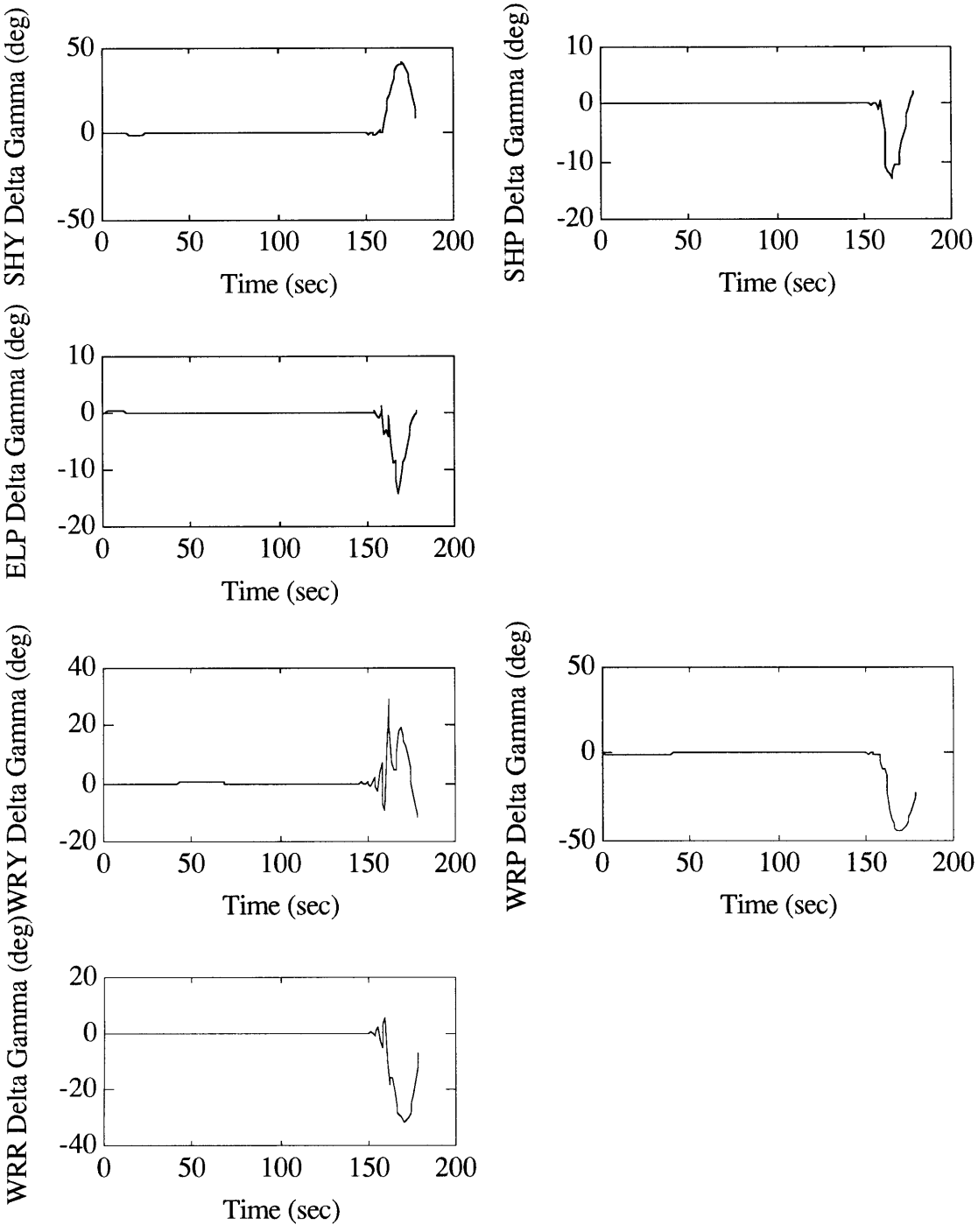

Figure 6.31. $\Delta\gamma$ History for LQR Compensator without Feedback Linearization

6.7 Pole Placement Controller

Using input-output feedback linearization it is possible to represent the nonlinear arm dynamics as a set of twelve integrators (two differentiations are required to get to the input and there are six joints). A pole placement controller can be designed in the outer feedback loop to stabilize the decoupled system, which also contains the servos and gearbox models. This pole placement controller is made up of twelve SISO lead-lag controllers. Using such a controller is different from the current lead-lag controller, which was applied only to the $\Delta\gamma$ states for feedback. The new pole placement controller will be applied to the $\Delta\gamma$ states as well as the $\Delta\dot{\gamma}$ states for feedback. The pole placement method was used to design a controller for the system with and without feedback linearization.

First, a pole placement controller was designed for the system at Point 1 without feedback linearization. The current lead-lag controller with a gain of 0.1 was used in the $\Delta\gamma$ states, while the current lead-lag controller with a gain of 0.01 was used in the $\Delta\dot{\gamma}$ states. The system without feedback linearization is stable for Point 1, however, when the SRMS moves to the subsequent points, some of the closed loop poles move to the right half plane (see highlighted cells), resulting in instabilities. Figure 6.32 and 6.33 present a plot of the pole locations for Point 1 through 6, while Table 6.3 present the corresponding pole locations.

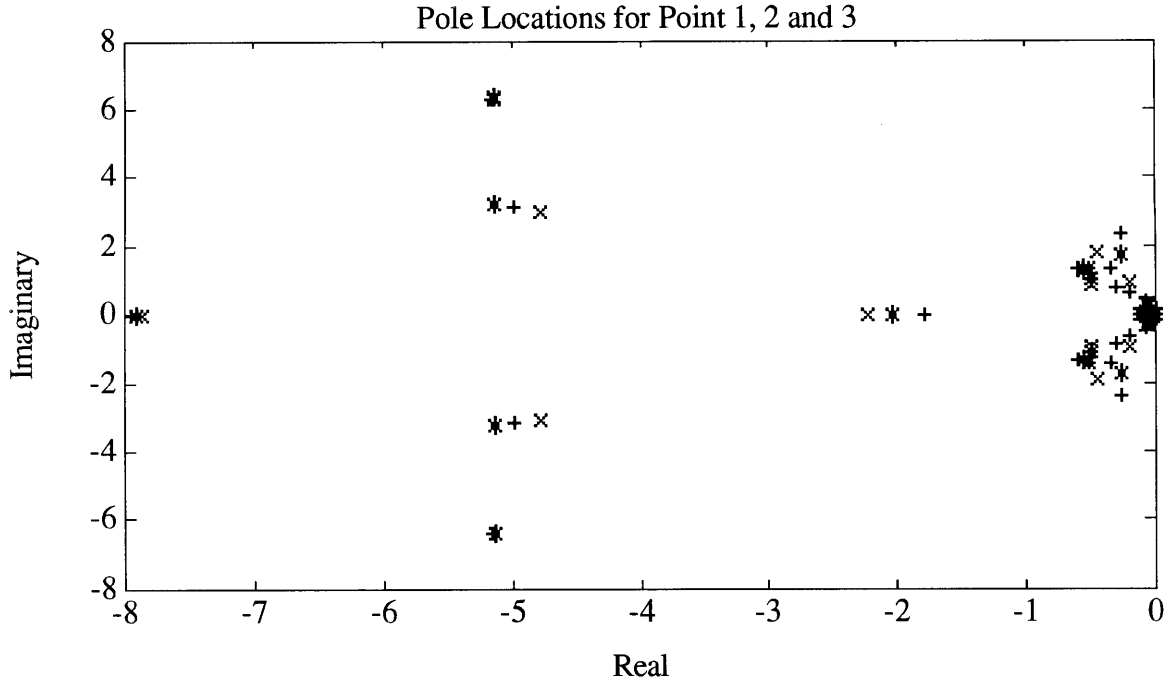

Figure 6.32. Pole Locations for Point 1,2 and 3

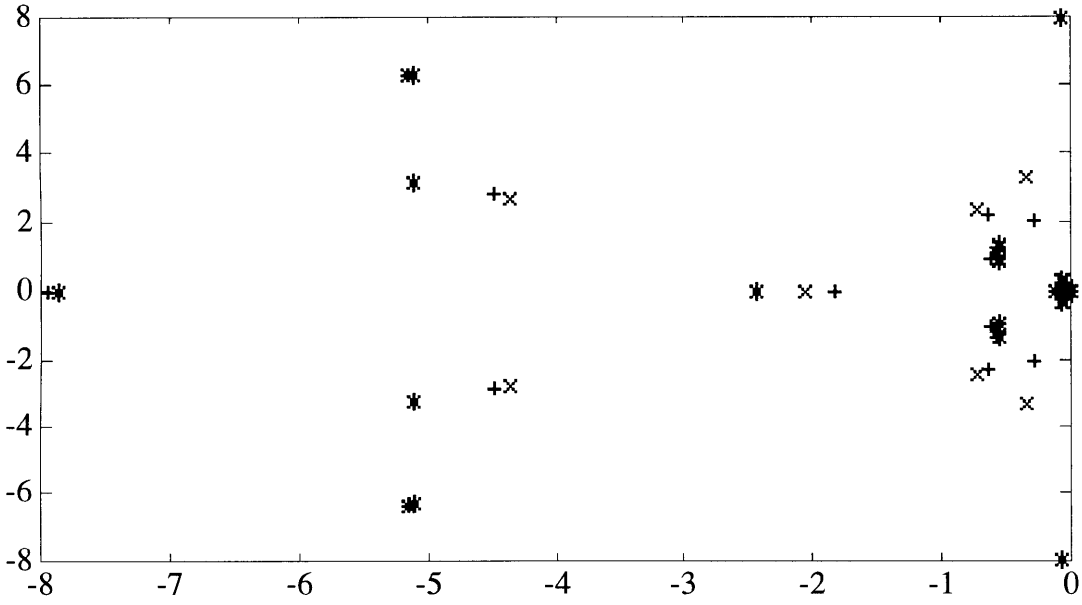

Figure 6.33. Pole Locations for Point 4, 5, and 6

Table 6.3. Pole Locations for Point 1,2, 3, 4, 5 and 6

Point 1	Point 2	Point 3	Point 4	Point 5	Point 6
-0.007	-0.0062	-0.0064	-0.0064	-0.007	-0.0061
-0.0071	-0.0072	-0.0077	-0.0076	-0.0071	-0.0073
-0.0096	-0.01	-0.0096	-0.0098	-0.0096	-0.0101
-0.0123	-0.0126	-0.0133	-0.0131	-0.0122	-0.0118
-0.0012-0.0191i	**0.0010-0.0134i**	**0.0014-0.0138i**	**0.0011-0.0141i**	-0.0125	-0.0122
-0.0012+0.0191i	**0.0010+0.0134i**	**0.0014+0.0138i**	**0.0011+0.0141i**	-0.0125	-0.0125
-0.0047-0.0202i	-0.0030-0.0212i	-0.0208	-0.0183	-0.0135	-0.0125
-0.0047+0.0202i	-0.0030+0.0212i	-0.0128-0.0261i	-0.0022-0.0236i	-0.0008-0.0185i	0.0014-0.0126i
-0.0248	-0.0258	-0.0128+0.0261i	-0.0022+0.0236i	-0.0008+0.0185i	0.0014+0.0126i
-0.0463	-0.027	-0.0455	-0.0256	-0.0024-0.0199i	-0.0037-0.0220i
-0.0523	-0.0549	-0.0535	-0.0547	-0.0024+0.0199i	-0.0037+0.0220i
-0.0391-0.1054i	-0.1169	-0.0988	-0.1176	-0.0257	-0.0263
-0.0391+0.1054i	-0.1227	-0.123	-0.1227	-0.0273	-0.0302
-0.1142	-0.1250-0.0000i	-0.125	-0.125	-0.0546	-0.0529
-0.1195	-0.1250+0.0000i	-0.125	-0.1250-0.0000i	-0.1179	-0.1162
-0.125	-0.125	-0.1250-0.0000i	-0.1250-0.0000i	-0.1204	-0.1232
-0.125	-0.125	-0.1250+0.0000i	-0.1250+0.0000i	-0.125	-0.125
-0.125	-0.125	-0.125	-0.1250+0.0000i	-0.125	-0.1250-0.0000i
-0.125	-0.125	-0.125	-0.125	-0.125	-0.1250+0.0000i
-0.125	-0.0453-0.1464i	-0.0434-0.1393i	-0.0469-0.1730i	-0.125	-0.125
-0.125	-0.0453+0.1464i	-0.0434+0.1393i	-0.0469+0.1730i	-0.1250-0.0000i	-0.125
-0.0675-0.2949i	-0.2154-0.6517i	-0.0579-0.2338i	-0.0612-0.2993i	-0.1250+0.0000i	-0.125
-0.0675+0.2949i	-0.2154+0.6517i	-0.0579+0.2338i	**0.0612+0.2993i**	-0.0450-0.1434i	-0.0494-0.1418i
-0.2087-0.9571i	-0.3240-0.8166i	-0.0752-0.3093i	-0.5625-0.9440i	-0.0450+0.1434i	-0.0494+0.1418i
-0.2087+0.9571i	-0.3240+0.8166i	-0.0752+0.3093i	-0.5625+0.9440i	-0.0541-0.2423i	-0.0429-0.1662i
-0.5042-0.9168i	-0.3450-1.3855i	-0.5052-1.0501i	-0.5703-1.0898i	-0.0541+0.2423i	-0.0429+0.1662i
-0.5042+0.9168i	-0.3450+1.3855i	-0.5052+1.0501i	-0.5703+1.0898i	-0.5835-0.9770i	-0.0817-0.3350i
-0.5740-1.3141i	-0.5286-1.3742i	-0.5732-1.3143i	-0.5740-1.3132i	-0.5835+0.9770i	-0.0817+0.3350i
-0.5740+1.3141i	-0.5286+1.3742i	-0.5732+1.3143i	-0.5740+1.3132i	-0.6246-0.9723i	-0.5673-0.8943i
-0.5230-1.3745i	-0.6096-1.3506i	-0.5646-1.3257i	-2.0709	-0.6246+0.9723i	-0.5673+0.8943i

Next, a pole placement controller was designed with feedback linearization. A block diagram of the *SIMULINK* model with this pole placement controller is presented in Figure 6.34. The current lead lag controller with a gain of 0.1 was applied to the $\Delta\gamma$ states in the new design. Six SISO lead-lag controllers with gains of 100, zeros at -1 and a pole at -10 were chosen to be used with the $\Delta\dot{\gamma}$ states. This pole placement controller placed the poles of the linearized system at: -0.0068+0.0089i, -.0068-0.0089i, -109.0833 and -0.9167.

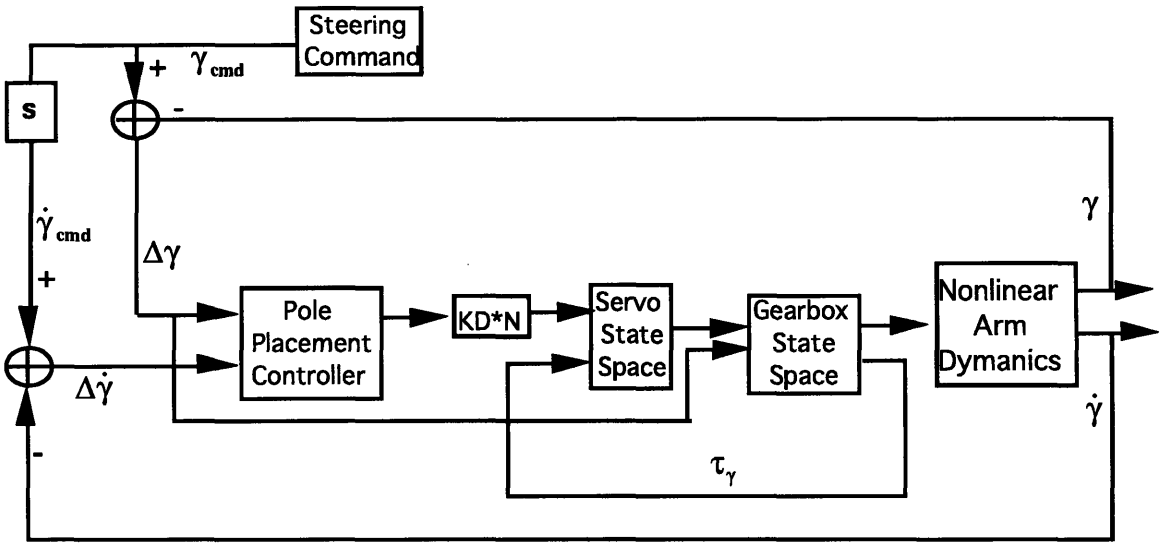

Figure 6.34. *SIMULINK* Model of Pole Placement Controller

The same trajectory for the lead-lag compensator was used with the pole placement compensator. Figures 6.35 through 6.37 present the joint angle, joint rate and $\Delta\gamma$ histories for the trajectory. Again, because the rate limit for the trajectory was set to be 0.14 deg/sec, the joint angle history with the pole placement controller that uses feedback linearization should be similar to the current lead-lag controller. If the rates were increased so that the feedback linearization terms became significant and the difference in the commanded joint angle and the actual joint angle was kept small, then it is expected that the pole placement controller, using the feedback linearization, will perform better than the current lead-lag controller.

With the pole placement controller, the trajectory is followed closely. The commanded joint angle trajectory is plotted with the actual joint angle history in Figure 6.34; they are nearly identical.

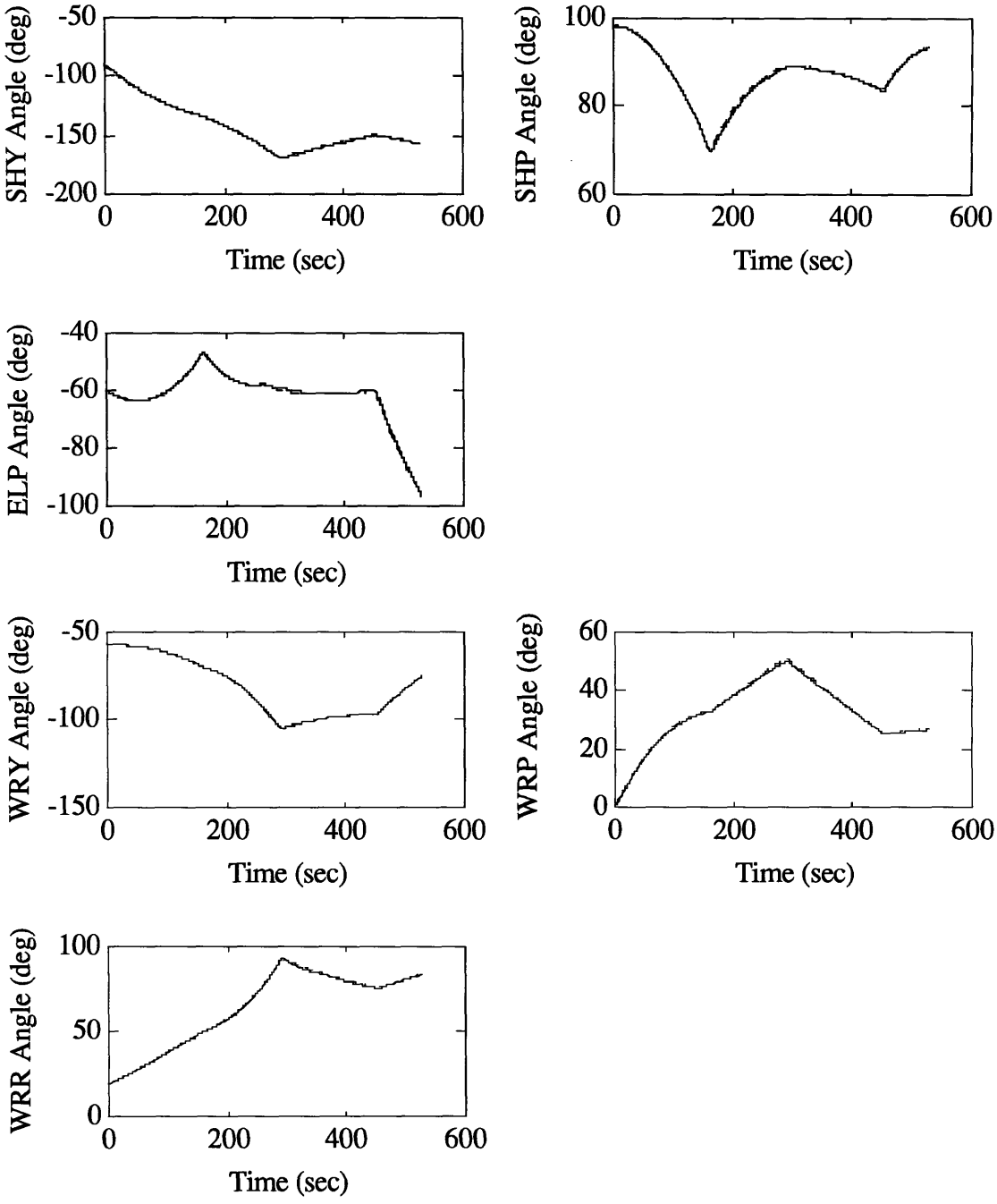

Figure 6.35. Joint Angle History for Pole Placement compensator

The joint rates for each of the joints are shown in Figure 6.36. The rate profiles for the shoulder yaw, shoulder pitch and elbow pitch joints are nearly identical to those that for the current lead-lag controller with and without feedback linearization. However, for the

three wrist joints, the maximum rates for the pole placement controller are 40 percent less than that for the current lead-lag controller.

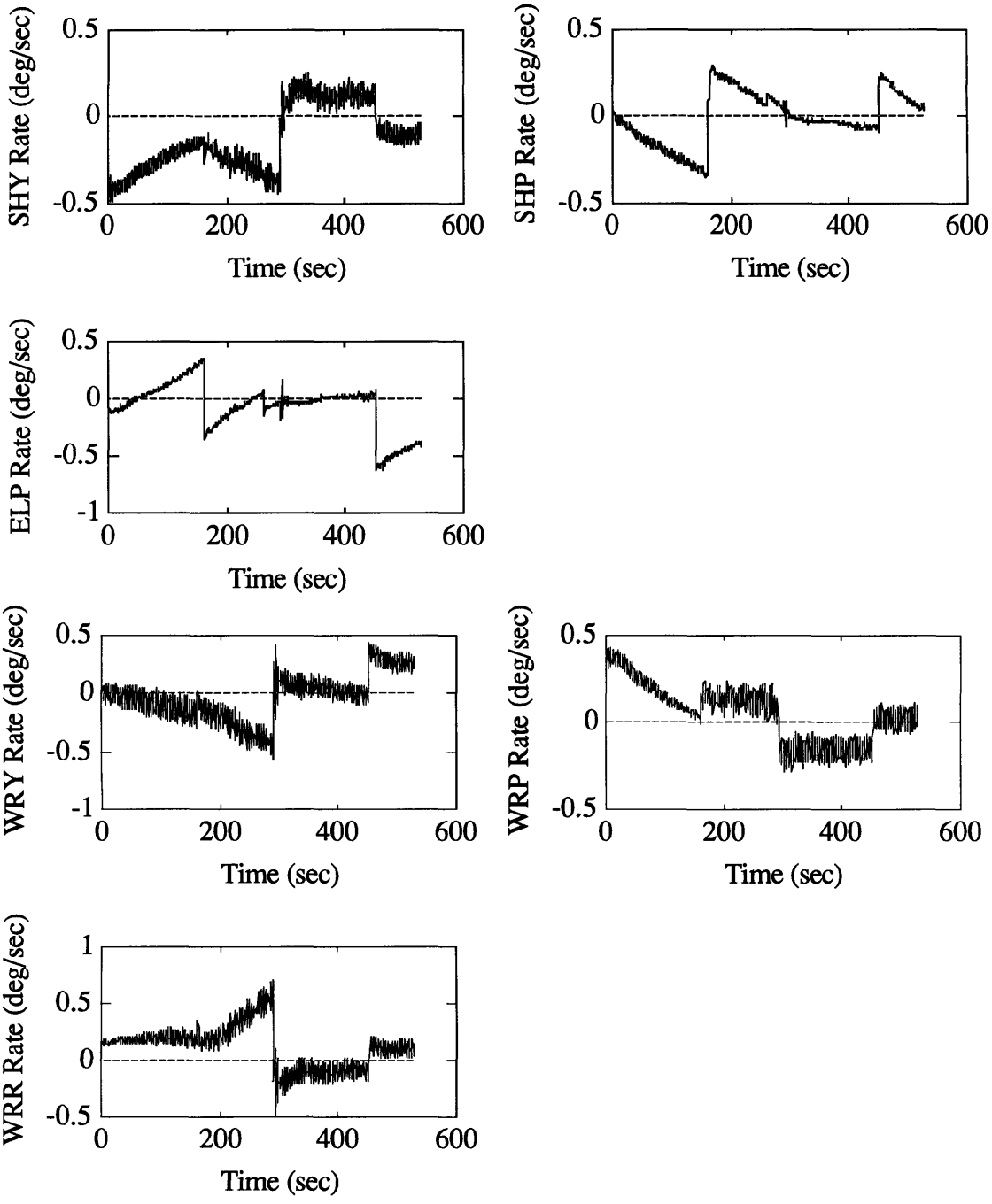

Figure 6.36 Joint Rate History for Pole Placement Controller

Figure 6.37 presents the $\Delta\gamma$, the difference between the commanded joint angle trajectory and the actual joint angle history for the six different joints. The $\Delta\gamma$ plots for the elbow pitch and wrist yaw joints are similar in magnitude as the $\Delta\gamma$ for the current lead-lag

controller, shown in Figure 6.21. The four other joints have larger magnitudes in $\Delta\gamma$ for the pole placement controller than for the current lead-lag controller.

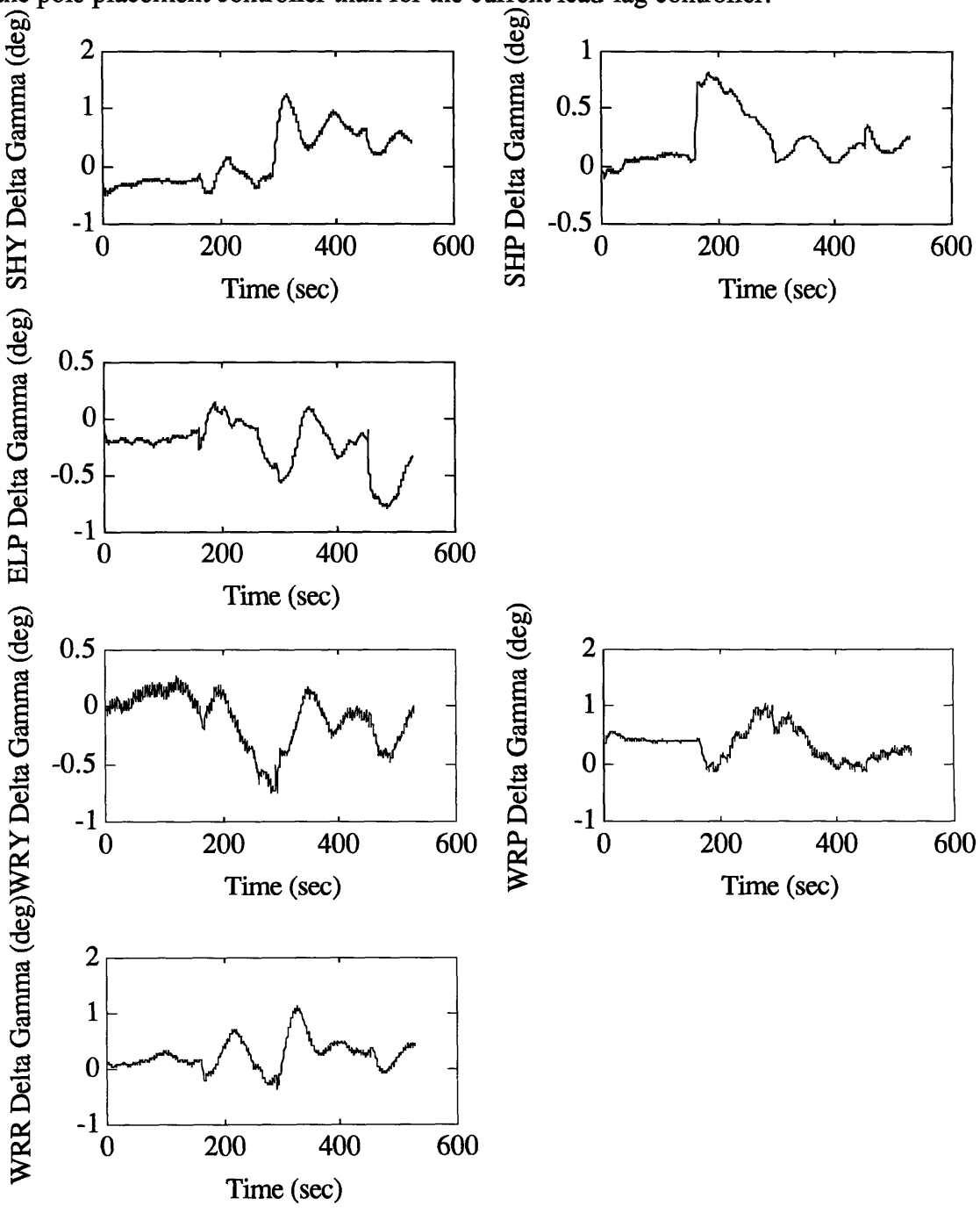

Figure 6.37 $\Delta\gamma$ History for Pole Placement Controller

Chapter 7

Conclusions and Future Work

SIMULINK models were generated for the SRMS system with the current lead-lag controller, a pole placement controller, and an LQR controller. The servos and gearbox models were linearized in the design model. Model reduction techniques were applied to the 42^{nd} order model with servos to obtain a 12^{th} order model. This allows for faster computation time and an implementable system. The nonlinear arm dynamics were modeled using the equations of motion for the SRMS.

This thesis has demonstrated some of the advantages in using simple feedback linearization techniques. The current lead-lag controller is used with rate limits of 0.14 deg/sec. At this slow rate, the joint acceleration due to feedback linearization terms is insignificant; however, at higher rates the joint acceleration due to the feedback linearization terms begin to dominate the control. Hence, if the rate limits were increased, using the feedback linearization control law in the "inner" loop would improve performance. It was also determined that the joint accelerations due to feedback linearization terms are dependent on the location of the end effector and the dimension properties of the payload. If the end effector is maneuvering a payload further out from the shuttle, the joint accelerations due to the feedback linearization terms will be greater than if the end effector were maneuvering a payload closer to the shuttle.

A nonlinear gearbox model was developed to replace the linearized gearbox in the SRMS model. The linear and nonlinear gearbox models were subjected to the same motor rate inputs from the servos. The resulting joint toques and gear torques were in the same direction, but of slightly different magnitudes. Also, the frequency content of the signals with and without the nonlinear gearbox model differed due to the nonlinear stiffness representation.

Exploring the possibilities of incorporating a higher bandwidth controller than the current lead-lag controller, an LQR controller was designed for the system without feedback linearization. Using this type of controller would enable the system to be stabilized when boom and gear flexibility are included in the system model. The present lead-lag controller would not provide good active damping of boom and gearbox flexibility because of the low bandwidth design and the lack of joint rate feedback. LQR compensation can not be counted on to stabilize the nonlinear system as demonstrated in Chapter 6. Future work might include developing a model based compensator for the including feedback linearization for a trajectory following problem with active damping of SRMS flexibility.

Finally, using feedback linearization, the nonlinear system appears to be a set of twelve integrators. It was possible to design a pole placement controller in the "outer" loop for this decoupled system. This system yielded smaller joint rate histories for the wrist joints than the current lead-lag controller system. The pole placement controller should can handle the vibration suppression problem better than the current lead-lag controller because the velocity states are fed back and it is possible to add more lead to the compensator and increase the bandwidth.

A possible extension of this thesis could include incorporating the techniques that Prakash [2] investigated for the position hold mode to the trajectory following problem. Prakash studied optimal control techniques to achieve fine control of the end effector in the presence of flexible-body dynamics and modeling uncertainty for the position hold mode. Boom flexibility issues can be addressed if end effector position measurements can be obtained, since flexibility is not observable in the current joint encoder measurements. Input/output feedback linearization would be required to maintain stability over the operating envelope of the SRMS.

Future work might also include implementation of the candidate controller on the high-fidelity, multi-flex-body, Draper RMS Simulator (DRS) to test its performance in berthing the SSF Stage 4 in the Orbiter bay via an automatic sequence. The speed of the maneuver and accuracy of the control could be compared to the existing SRMS controller.

References

[1] Sasiadek, J.Z., " Space Robotics and Manipulators: Lessons Learned From the Past and Future Missions and Systems", *12th IFAC Symposium on Automatic Control in Aerospace* , Ottobrun, Germany, September 7-11, 1992.

[2] Prakash, O., " Multivariable Control of the Space Shuttle Remote Manipulator System Using $\mathbf{H}_2$ and $\mathbf{H}_\infty$ Optimization", Masters Thesis, MIT, Cambridge, MA, May 1991. CSDL-T-1083.

[3] Scott, M.A. and Demeo, M.E., "Active Vibration Damping of the Shuttle Remote Manipulator System," *Proceedings of the AIAA Guidance and Control Conference*, New Orleans, Louisiana, August, 1991.

[4] Ravindran, R. and Doetsch, K.H., " Design Aspects of the Shuttle Remote Manipulator Control," *Proceedings of the Guidance and Control Conference*, AIAA Paper No. 82-1581, 1982.

[5] Spar Aerospace Limited, "Spar STS-3 RMS Press Kit," March 1982.

[6] Doyle, J.C., Synthesis of Robust Controllers and Filters," **IEEE CDC**, San Antonio, TX 1983

[7] Vidyasagar, M. Nonlinear Systems Analysis, 2nd Ed. Prentice Hall, NJ. 1993.

[8] Glenn, T., "Composite MIMO Nonlinear Control System Design Using $\mathbf{H}_2$ / $\mathbf{H}_\infty$ Optimization, Nonlinear Feedback and Parameter Adaptation" Masters Thesis, MIT, Cambridge, MA, December 1992.

[9] Slotine, J.J., and Li, W., Applied Nonlinear Control, Prentice Hall, Englewood Cliffs, NJ, 1991.

[10] Bedrossian, N., "Nonlinear Control Using Linearizing Transformations", PhD Thesis, MIT, Cambridge, MA, September 1991.

[11] *Payload Deployment and Retrieval System Simulation Database*, Version 1.0, NASA Document JSC-25134, July 1, 1991.

[12] "Stability Analysis and Gain Setting for POHS Controller", Presented by SPAR Aerospace to the Payload Data Retrieval System Math Model Working Group, Johnson Space Center, Houston, TX, Nov. 7, 1991.

[13] Moore, B.C., "Principal Component Analysis in Linear Systems: Controllability, Observability, and Model Reduction," IEEE Trans. on Auto. Control, Vol, AC-26, pp. 17-32, 1981.

[14] Enns, D.F., "Model Reduction with Balanced Realizations: an Error Bound and a Frequency Weighted Generalization," 1984 IEEE Conference on Decision and Control, Las Vegas, Nevada.

[15] Pham, T., " RMS Position Hold Function Modification CR", Lockheed, March 12, 1992.

[16] Bedrossian, N. and Crouse, M., "Rigid Body Kinematic SRMS Model," Charles Stark Draper Laboratory Memo: ESC-92-318, 1992.

[17] Greenwood, D., Principles of Dynamics. Prentice Hall, Inc. Englewood Cliffs, NJ 1988.

[18] Carroll, J., " The Notation and Use of Quaternions for Shuttle Ascent Steering", Charles Stark Draper Laboratory Memo: SSV10C-75-47, 1975.

[19] Kirk, D. Optimal Control Theory, An Introduction. Prentice-Hall Inc., Englewood Cliffs, NJ.1970.

[20] Athans, M., " Course Notes in Multivariable Control Systems, I & II", MIT 1991.

[21] Kwakernaak, H., and Sivan, R., Linear Optimal Control Systems, Wiley-Interscience, 1972.

[22] Bryson, A. Applied Optimal Control. Hemisphere Publishing Company, Washington D.C., 1975.

[23] *Simulink User's Guide*, The Mathworks, Inc., March 1992.

[24] Sastry, S.S. "Introduction to Linearization by State Feedback."

[25] Kawamura, S., Miyazaki, F., and Arimoto, S., "Is A Local Linear PD Feedback Control Law Effective"IEEE 1988